

Technische Universität
München
Fakultät für Physik



Abschlussarbeit im Masterstudiengang Physik

Title : Halo-independent interpretation of dark
matter searches with CRESST

von Gonzalo Herrera

Erstgutachter (Themensteller): Prof. A. Ibarra
Abgabetermin: 02.07.2020

Abstract

Dark Matter is one of the biggest unsolved puzzles of fundamental physics. In recent years, direct detection experiments have increasingly constrained the parameter space of weakly interacting massive particles (WIMPs), a very well theoretically motivated dark matter candidate. Nevertheless, the unknown nature of dark matter makes necessary to reanalyze the results of these experiments, accounting properly for the yet misunderstood dark matter phase space distribution. This thesis attempts to systematize and quantify, in a statistically solid manner, the impact of astrophysical uncertainties (particularly, of the dark matter velocity distribution) in local dark matter searches, emphasizing the developed methodology for the CRESST experiment.

Zusammenfassung

Dunkle Materie ist eines der größten Rätsel der fundamentalen Physik. In den letzten Jahren haben die Experimente zur direkten Suche den Parameterraum von schwach wechselwirkende massereiche Teilchen (WIMPs), einem sehr gut motivierten theoretischen Kandidaten für dunkle Materie, zunehmend eingeschränkt. Die unbekannte Natur der dunklen Materie macht es jedoch notwendig, die Ergebnisse dieser Experimente neu zu analysieren und dabei die noch unverstandene Phasenraumverteilung der dunklen Materie angemessen zu berücksichtigen. In dieser Arbeit wird versucht, die Auswirkungen astrophysikalischer Unsicherheiten (insbesondere der Geschwindigkeitsverteilung der dunklen Materie) bei der lokalen Suche nach dunkler Materie zu systematisieren und auf statistisch solide Weise zu quantifizieren, wobei die entwickelte Methodik für das CRESST-Experiment hervorgehoben wird.

Acknowledgments

I want to thank my supervisor Alejandro Ibarra for his confidence in me and this project, broadening my physics horizon by constantly suggesting new possibilities and approaches. I am very grateful to Federica Petricca and the CRESST collaboration for giving me the opportunity of being part of their group and learn the difficult reality and technicalities of dark matter direct detection experiments. Furthermore, I want to acknowledge the continuous help during this project of Andreas Rappelt. This work wouldn't have been possible without him. Last but not the least, I want to thank my family for their support and giving me the possibility to study physics.

This work was finished during the COVID-19 outbreak, and I also would like to thank all the people who kept the institutions running and fought against the virus in the front line.

Contents

1	Dark Matter : Introduction	1
1.1	Evidence for Dark Matter	2
1.1.1	Rotation curves of galaxies	2
1.1.2	Colliding galaxy clusters	3
1.1.3	Cosmic Microwave Background	4
1.1.4	Big Bang Nucleosynthesis	5
1.2	Cosmology : Λ CDM	6
1.2.1	Dark Matter production: WIMPs	7
1.2.2	Structure formation	9
1.2.3	Dark Matter substructure	11
2	Dark Matter in the Milky Way	13
2.1	The Dark Matter density	13
2.2	The Dark Matter velocity distribution	14
2.2.1	The Standard Halo Model (SHM)	14
2.2.2	N-Body simulations	16
2.2.3	Tracers observations	18
2.2.4	Maximum entropy velocity distribution	20
3	Dark Matter searches	24
3.1	Collider searches	24
3.2	Indirect searches	25
3.2.1	Capture mechanism : Detecting dark matter with neutrino experiments	26
3.3	Direct searches	28
3.3.1	The CRESST Experiment	30
4	Direct detection formalism	32
4.1	Kinematics of DM-nucleus scattering	32
4.2	Effective field theories to describe DM-nucleus interactions	34
4.2.1	Spin-independent interactions	35
4.2.2	Spin-dependent interactions	38
5	Parametrization of dark matter astrophysical uncertainties	40
5.1	Methodology: Optimization of the dark matter velocity distribution	40
5.2	Parametrizing deviations from the SHM: Information theory divergences	44
5.3	Analyzing the impact of astrophysical uncertainties in CRESST III	49
5.4	A proof of concept : Ruling out specific DM models	55
5.4.1	Testing <i>Z-mediated</i> DM in a halo-independent manner	55
5.4.2	Testing <i>Sneutrino</i> DM in a halo-independent manner	57
5.5	Combined halo-independent analysis of CRESST II and SK	60
6	A bayesian approach to the dark matter velocity distribution problem	63
6.1	The quantified maximum entropy method	63
6.2	Extracting information of the DM velocity distribution from CRESST III	65

7	Alternative scenarios: Extragalactic dark matter and Inelastic dark matter	70
7.1	Extragalactic dark matter at CRESST	70
7.2	Inelastic dark matter at CRESST	72
8	Conclusions	77
A	Appendix A	78
A.1	Convex Optimization	78
A.2	The Karush-Kuhn-Tucker optimality conditions	79
A.3	Linear programming	80
A.4	Second Order Cone Problems (SOCP)	81
A.5	Exponential Cone Problems	82
A.6	Interior-point methods	83
A.7	Disciplined Convex Programming (DCP)	85
B	Appendix B	87
B.1	Introduction to Information theory	87
B.2	Proofs of theorems 1 and 2	88
C	Appendix C	89
C.1	Statistics of DM discovery and upper limits	89
C.1.1	Poisson statistics	89
C.1.2	Yellin Methods	90
C.2	DDCalc-2.2.0 software : Implementing CRESST III	91

1 Dark Matter : Introduction

Although the discussion about the existence of invisible matter in the form of dark stars, dark planets, dark nebulae or dark clouds was already active in the XIX century, [1], it was not until the beginning of the XX century that the first theoretical estimates of the amount of dark matter in the Milky Way were performed. Kelvin, only by using Newtonian mechanics and the kinetic theory of gases, proposed a method to relate the size of the galaxy and the velocity dispersion of stars, concluding from observations that many of them could be extinct and dark, [2]. E.Öpik, J.H. Kapteyn, J.C. Jeans, and J.H. Oort tried to measure the local matter density in the solar neighborhood but did not find compatible results, [3]. It was in two papers of 1933 and 1937, [4][5], when the first compelling observational evidence of dark matter was found by Zwicky. He applied the virial theorem to the Coma Cluster and estimated a mass-to-light ratio of ~ 500 , which could only be explained due to the existence of an additional source of non-luminous matter. After some years in which caveats to Zwicky's publication were discussed, [6] and alternative explanations to the high mass-to-light ratio were provided, [7], the measurement of rotation curves of stars in galaxies of Vera Rubin and collaborators, [8], consolidated the dark matter paradigm.

The dark matter evidence coming from Vera Rubin and Kent Ford observations of galaxy rotation curves is the starting point of this thesis. In section 1, we discuss further evidence coming from colliding galaxy clusters, [9], the cosmic microwave background (CMB), [10], and Big Bang nucleosynthesis, [32], which revealed the existence of dark matter to describe consistently our current universe within the cosmological model of Λ CDM. More precisely, latest results of the Planck satellite mission, [11], show that visible matter only accounts for 5% of the total energy density of the universe, while dark matter represents $\sim 27\%$, the remaining being dark energy Λ . Based in this evidence, we introduce Weakly Interacting Massive Particles (WIMPs), [12] and motivate them as a dark matter candidate, describing its production in the early universe. We furthermore briefly discuss the formation of structures in the universe within Λ CDM and in particular the dark matter halo and substructure formation, [13][14]. In section 2, we discuss the state of the art about the dark matter halo in the Milky Way, particularly the local density of dark matter in the solar neighbourhood and the dark matter velocity distribution, quantities of crucial importance in different dark matter searches, [15]. We point out that the current Standard Halo Model (SHM) used by experiments might not be a good description of our dark matter halo. Finally, we propose a novel method to compute the dark matter velocity distribution based in the *principle of maximum entropy*, [16]. In section 3, we show some of the different experimental searches for dark matter taking place, dedicating special attention to the description of the dark matter capture mechanism in indirect searches, which search for the products of annihilations of dark matter particles into standard model particles, and the state of the art of direct detection experiments, which search for direct interactions of dark matter with detectors placed on Earth. We present in more detail the CRESST experiment, [17][18], as we will be working with their results in the latter part of this thesis. In section 4, we review the direct detection formalism necessary to make dark matter predictions, discussing the importance of the kinematics in the capability of direct detection experiments to access certain dark matter phase space configurations.

In section 5, we develop a method to quantify the impact of astrophysical uncertainties in a direct detection experiment, based on tools from information theory, [19]. By using this technique, we derive upper limits on the dark matter scattering cross-section using CRESST, [20], including uncertainties from the velocity distribution. Furthermore, we discuss the possibility of these methods to rescue or definitely rule out specific dark matter models in a halo-independent manner. Finally, we perform a combined halo-independent analysis of CRESST and Super-Kamiokande results, [21]. In section 6, we develop a bayesian technique based in the *quantified maximum entropy* method, [22], which allows to interpolate between the SHM and the maximally entropic velocity distributions consistently with the results of a certain direct detection experiment.

The thesis concludes in section 7 with a short discussion about alternative scenarios that could arise from the extragalactic dark matter component and the inelastic interaction of dark matter particles with nuclei, [23][24]. We use the 4 high-recoil unidentified events of CRESST II, [17], to show that a proper knowledge of the dark matter phase space distribution and kinematics is crucial in order to make high precision measurements.

1.1 Evidence for Dark Matter

There is evidence for the existence of dark matter on different scales. We present here some of the most convincing observations.

1.1.1 Rotation curves of galaxies

Rotation curves of galaxies represent the circular velocity $v_{rot}(r)$ of stars as a function of their distance to the galactic center. For illustration purpose, we can naively assume a spherically symmetric density distribution $\rho(\vec{r}) = \rho(r)$ for the galaxy. From Newtonian mechanics, the shape of the rotation curve can be derived equating the gravitational force produced by the mass enclosed in the sphere of radius r and the centripetal force of an object at this position

$$\frac{GM(r)m}{r^2} = \frac{mv_{rot}^2}{r} \quad (1)$$

and

$$v_{rot} = \sqrt{\frac{GM(r)}{r}}, \quad (2)$$

where

$$M(r) = \int_0^r 4\pi\rho(r')r'^2 dr'. \quad (3)$$

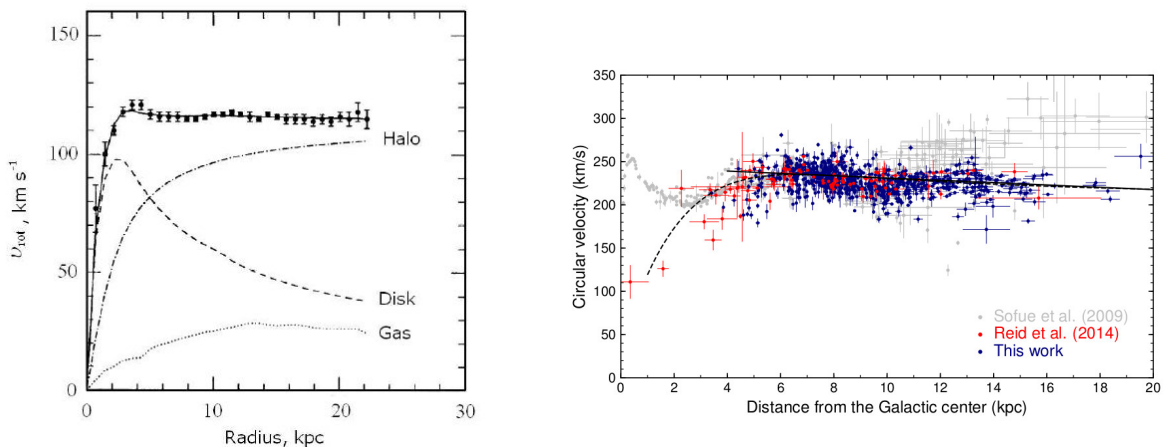


Figure 1: On the left, the rotation curve of galaxy NGC 6503, taken from [25], including the main contributions summing up the total measure: the gas, stellar disk and dark matter halo. On the right, recent measurements of the Milky Way rotation curve from classical cepheids, taken from [26].

At the center of the galaxy the density is roughly constant and $v_{rot} \propto r$. This can only approximate the observed rotation curve at the very core of the galaxy, see Figure 1. For stars orbiting the outer part of the galaxy, $M(r)$ is equal to the total mass of the galaxy, thus constant, and $v_{rot} \propto r^{-1/2}$. In the case of spiral galaxies, this approximation is well justified, since they typically present a bulge at the core which contains most of the luminous matter. The prediction for v_{rot} in the outer region of galaxies is incompatible with observations, that show an approximately flat profile in the outskirts of, see Figure 1. This discrepancy can be explained by considering an additional, non luminous, source of gravitational potentials present on the galaxy beyond the baryonic disk.

1.1.2 Colliding galaxy clusters

Since the observation in 2006 of the galaxy cluster 1E0657-558, the Bullet Cluster, [9], collisions of galaxy clusters have been argued as a proof of the existence of dark matter. These works typically construct a map of the gravitational potential using weak gravitational lensing, which measures the distortions of images of background galaxies caused by the gravitational deflection of light by the cluster's mass. While this shows that most of the matter remains in the individual clusters after the collision, the thermal X-ray emission map shows that most of the baryonic matter is concentrated in the collision region.

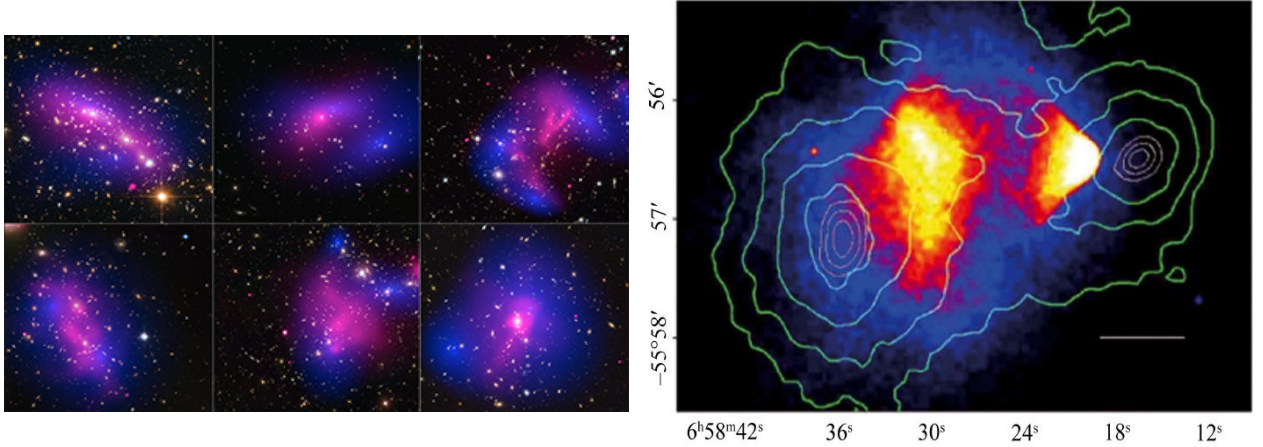


Figure 2: On the left, 6 examples of colliding galaxy clusters, taken from [27], where the dark matter (blue) and stars are clearly separated from baryonic matter (pink). On the right, the Bullet Cluster, [9]. The green contours show the weak-lensing reconstructions, and the color gradient is the thermal X-ray emission map. The centers of the gravitational potential are shifted with respect to the strongest X-ray emission regions of the plasma

This effect has been observed not only in the Bullet Cluster but on several further colliding galaxies, see Figure 2. Since there is 5 times more mass in the form of gas than stars, the discrepancy between the weak lensing map and the thermal X-ray emission can only be explained by the presence of dark matter. In this interpretation stars and dark matter move nearly collisionless away from the center of the collision, while baryonic matter from both cluster interacts electromagnetically and remains in the center. The observation of collisions of galaxy clusters challenge the so-called MOND (Modified Newton Dynamics) theories, which propose that the gravitational evidence for dark matter is due to a modification of the law of gravity at large scales, [28].

1.1.3 Cosmic Microwave Background

The Cosmic Microwave Background (CMB) radiation is one of the most compelling arguments in favour of dark matter. In the early stages of the universe, at the time of recombination (redshift $z \approx 1100$), radiation decoupled from matter and since then, photons travelled freely. The almost perfect black-body CMB spectrum shows the temperature (2.728 K), or the inverse wavelength, of the microwaves that we receive on Earth from this early times, see Figure 3. When looking closely at this spectrum, one finds fluctuations in the μK scale, [11].

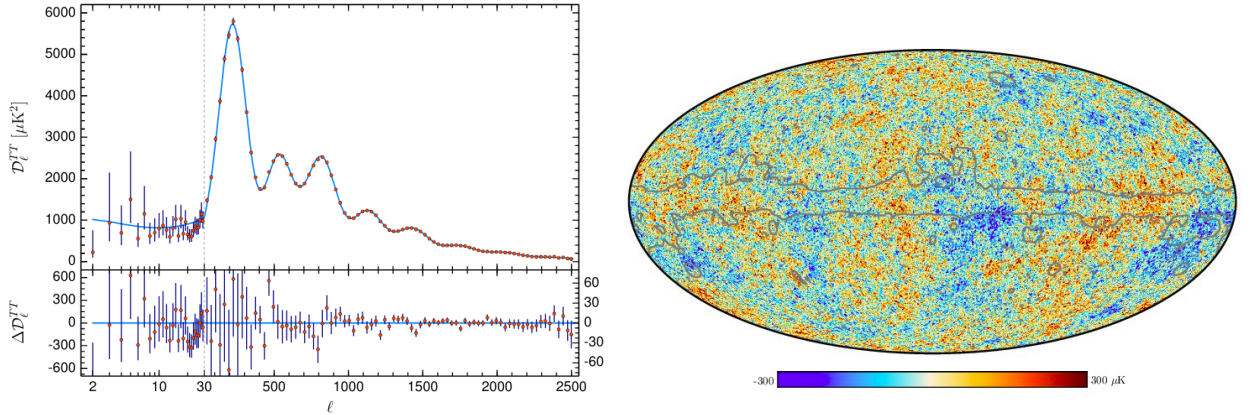


Figure 3: On the left, the most recent Planck satellite measurement of the CMB angular power spectrum in terms of the multipole moment l , [11]. The first peak is correlated with the amount of baryonic matter. The measured position and height of the second and third peaks are consistent with a dark matter abundance of roughly 5 times higher than baryonic matter, [55]. On the right, the most recent Planck satellite sky map of the CMB temperature anisotropies

The temperature anisotropies of the CMB are explained as baryon acoustic oscillations, [29]. Previous to the recombination era, when the free electrons still strongly scattered the photons of the cosmic plasma, this rang with sound waves excited by the initial perturbations of the inflaton field, [30]. The photon radiation pressure keeps the ionized gas from clustering, and this pressure leads to relativistic sound waves that propagate until the plasma becomes neutral at recombination. The mechanism then freezes and CMB photons carry information about the baryonic density profile in their temperature profile. Photons coming from dense baryonic regions loose energy by escaping the gravitational potential and are redshifted. On the other hand, photons coming from diluted regions are blueshifted with respect to the average CMB photon temperature. This is called the Sachs-Wolfe effect, [31]. Since the coupling of dark matter and baryons to photons is different, the power spectra of temperature and polarization fluctuations depend crucially on the ratio between both components.

1.1.4 Big Bang Nucleosynthesis

At redshift $z \approx 4 \times 10^8$, Big Bang nucleosynthesis takes place and light elements are formed. It starts with the production of deuterium and ends up with the production of helium



though low probability reactions up to ${}^7\text{Li}$ also occurred. While the fraction of baryons that make up the helium abundance is mainly sensitive to the n/p ratio at the time of nucleosynthesis, [32], which from Boltzmann statistics is $\sim 1/7$ and leads to $\sim 25\%$ of the mass of baryons forming helium ${}^4\text{He}$, the deuterium, helium ${}^3\text{He}$ and ${}^7\text{Li}$ abundances depend on the baryon density at the time of nucleosynthesis, see Figure 4.

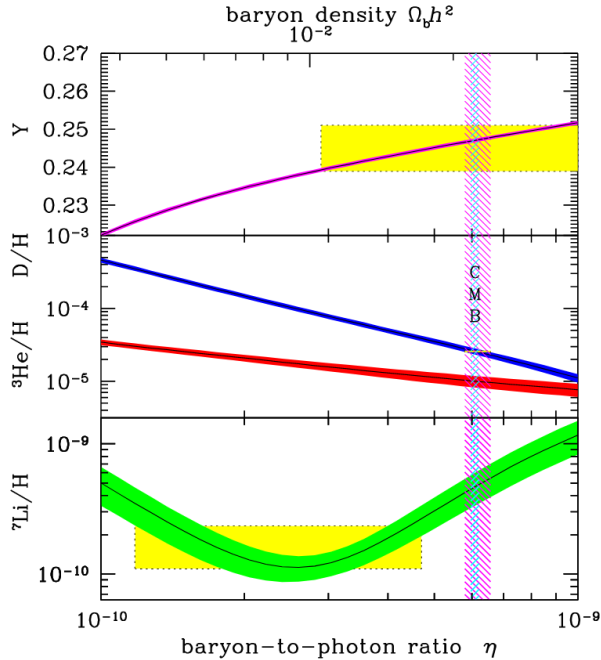


Figure 4: Primordial abundances of light elements as a function of the baryon density relative to photons and the CMB observations. The bands show the 95%CL range. Boxes indicate the observed light element abundances. The narrow vertical band indicates the CMB measure of the cosmic baryon density, while the wider band indicates the BBN $D + {}^4\text{He}$ concordance range (both at 95% CL), [33]

Deuterium, due to its stability (binding energy of 2.2 MeV), is a good thermometer of the baryon density at nucleosynthesis, since it is only destroyed hereafter, like in the evolution of stars, but never enduringly produced. Therefore, the amount of deuterium, but also of other light elements in the universe can be used to set an upper limit in the baryon density, [33]. Therefore BBN, which provides a measure of the baryon density, indicates the existence of dark matter when combined with the measure of the matter density coming from the CMB.

1.2 Cosmology : Λ CDM

The Λ CDM model of cosmology represents a century of confluence work of theoretical and observational efforts. The universe contains four major components: dark energy Λ , cold dark matter CDM, baryonic matter B and radiation R , where the density proportions can be extracted from the CMB anisotropies and are given by, [11],

$$\Omega_{\Lambda}h^2 = 0.3107 \pm 0.0082 \quad (6)$$

$$\Omega_{\text{DM}}h^2 = 0.1200 \pm 0.0012 \quad (7)$$

$$\Omega_B h^2 = 0.02234 \pm 0.0001, \quad (8)$$

where $0.4 \leq h \leq 1.0$, and the density of radiation Ω_R is negligible today $\mathcal{O}(0.0001)$. Although the yet unknown nature of dark energy Λ and dark matter may indicate some small scale inconsistencies, [34], it is the current parameterization that better explains simultaneously

the existence of the cosmic microwave background (CMB), the observed accelerating expansion of the universe, the observed abundances of hydrogen (including deuterium), helium, and lithium, and the formation of large scale structures in our Universe.

In this section, we will review the basics of the cold dark matter paradigm (CDM): the CDM particle production in the early universe and the CDM structure formation, emphasizing the formation of dark matter halos and its subsequent substructure.

1.2.1 Dark Matter production: WIMPs

In the modern cosmological picture, right after the inflationary period, [30], the Universe is filled with a relativistic plasma of particles. For the understanding of the thermal history of the Universe and the CDM paradigm, the comparison between the rate of particle interactions Γ and the rate of expansion of the universe H (Hubble rate) is crucial. In this discussion, the temperature of the primordial plasma T is proportional to the scale factor a of the Friedmann-Lemaitre-Robertson-Walker (FLRW) metric $T \propto a^{-1}$, and the rate of change in the temperature is just the Hubble expansion parameter $\dot{T}/T = -H$, [35].

So long as the interactions necessary for particle distributions to adjust to the temperature changes are rapid compared to the expansion rate, the Universe will evolve through a succession of nearly thermal states (local thermal equilibrium) with temperature decreasing as a^{-1} . It is considered in the literature, [35], that reactions are happening rapidly enough to maintain local thermal equilibrium when $\Gamma \geq H$. As the Universe cools, the rate of interactions could decrease faster than the expansion rate. At $\Gamma \approx H$, the different particles (dark matter among them) decouple from the thermal bath. Different particle species may have different interaction rates and so may decouple at different times. Boltzmann constant is set equal to unity, $k_B = 1$, so that the temperature has units of energy. The rate of particle interactions is given by the expression:

$$\Gamma \equiv n\sigma v, \tag{9}$$

where n is the number density of particles, σ is their interaction cross section and v is the average velocity of the particles. For a process $1 + 2 \leftrightarrow 3 + 4$, the interaction rates of species 1 and 2 would be written as $\Gamma_1 = n_2\sigma v$ and $\Gamma_2 = n_1\sigma v$ respectively with v being the average relative velocity of species 1 and 2 and n_i their respective densities. The approximation $n_1 \sim n_2 \equiv n$ will be taken for high energies. In conclusion, this interaction rate describes the probability of particles 1 and 2 to scatter. The distribution functions of the different particles in the thermal bath can be described by Fermi-Dirac and Bose-Einstein statistics. If the Universe had remained in equilibrium, it would be mostly photons and neutrinos. Any massive particle species would be suppressed due to the exponential factor in the distribution function, $e^{-m/T}$. For baryons this is not quite correct since baryon number is a symmetry of the Standard Model. Deviations from equilibrium lead to the freeze out of massive particles, where they acquire a relic abundance still present today.

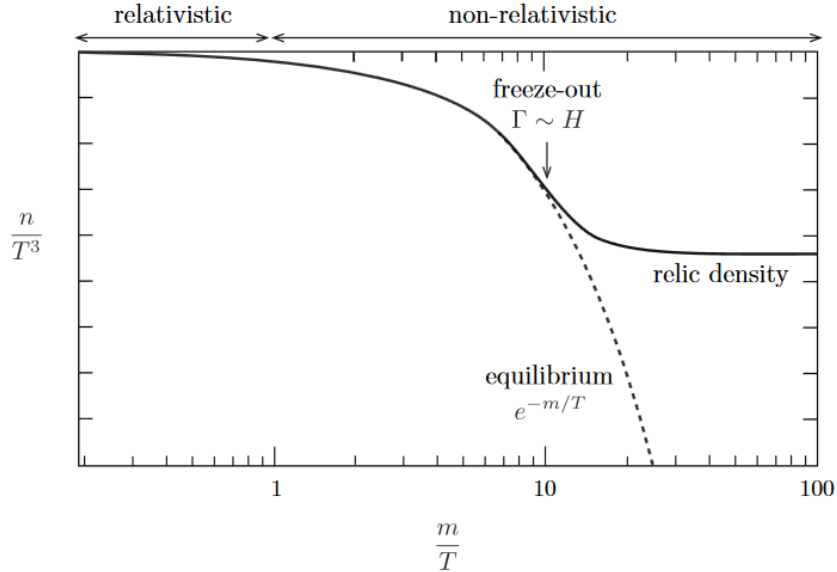


Figure 5: Freeze out process. At high temperatures $T \gg m$, the particle abundance tracks its equilibrium value. At low temperatures $T \ll m$, the particles freeze out maintaining a relic density much larger than the Boltzmann-suppressed equilibrium abundance, [36]

In order to understand the evolution beyond equilibrium, the Boltzmann equation is required. In the absence of interactions, the number density of a particle species i evolves as

$$\frac{dn_i}{dt} + 3\frac{\dot{a}}{a}n_i = 0, \quad (10)$$

due to the fact that the number of particles in a fixed physical volume is conserved, so that the density dilutes with the expanding volume, $n_i \propto a^{-3}$. Adding a collision term to include the effects of interactions yields

$$\frac{dn_i}{dt} + 3Hn_i = C_i[n_j]. \quad (11)$$

This is the Boltzmann equation. The form of the collision term depends on the interactions under consideration. If we only contemplate single particle decays and two particle scatterings/annihilations, the processes are condensed in $1 + 2 \leftrightarrow 3 + 4$. To track the number density n_1 of species 1, it is considered that the rate of change in the abundance of species 1 is given by the difference between the rates for producing and eliminating the species. The collision term then takes the form

$$\frac{dn_1}{dt} + 3Hn_1 = -\langle\sigma v\rangle_{12}n_1n_2 + \langle\sigma v\rangle_{34}n_3n_4, \quad (12)$$

where $\langle\sigma v\rangle$ is the thermally averaged cross section. The thermally averaged cross section is similar to that of a cross section, but one has to consider that the “initial conditions” do not correspond to a well defined energy, but rather it is necessary to integrate to the possible energies (or velocities) that the particles in the thermal bath may have. Thus, the thermally averaged cross section depends on the relative velocity between particles, and the

brackets denote an average over v . By taking into account that the collision term vanishes in chemical equilibrium, equation 12 can be expressed as

$$\frac{1}{a^3} \frac{d(n_1 a^3)}{dt} = - \langle \sigma v \rangle [n_1 n_2 - \left(\frac{n_1 n_2}{n_3 n_4}\right)_{eq} n_3 n_4]. \quad (13)$$

This formula allows to compute the relic density of WIMPS (Weakly Interacting Massive Particles) as dark matter agents. It is convenient to distinguish different dark matter particles according to their freeze out temperature $x = m_\chi/T$: Hot Dark Matter (HDM) with $x_f \ll 3$, Cold Dark Matter (CDM) with $x_f \gg 3$ and the intermediate case of Warm Dark Matter (WDM) with $x_f \sim 3$. This distinction is relevant because the value of x_f is determinant in the latter Universe structure formation, [37]. WIMP's assumption as cold dark matter is, a priori, well justified by two reasons. The first one is that, since the main assumption in the thermodynamics depiction of the primordial bath is that it is formed by a gas of weakly interacting particles, it is reasonable to consider dark matter also as weakly interacting, though massive, since freeze out happens earlier for massive particles before than photons decouple, [36]. The second and more important reason is that a cross section characteristic of the weak interaction $\sigma_\chi \sim 10^{-40}$ gives the right dark matter abundance today. This is called the WIMP miracle. Another motivation to consider WIMPs as CDM, not theoretical but purely experimental, is that the weak scale is testable and accesible to several experiments nowadays.

1.2.2 Structure formation

In Λ CDM, the structures of the universe are formed from small early density fluctuations, where the nature of dark matter plays a crucial role. The CMB temperature map anisotropies indicate evidence for fluctuations $\delta(x, t)$ in the primordial matter density

$$\rho(x, t) = \bar{\rho}(t)[1 + \delta(x, t)], \quad (14)$$

where $\bar{\rho}$ is the average matter density over all space. These small density perturbations form, via gravity, the large scale structures observed in the late universe. The growth of structure are determined by the background pressure and gravity. The overall fluctuating density field can be considered as a superposition of waves with different wavelengths, phases, and amplitudes. Then, it is possible to take a Fourier transform $\delta_k \sim \sum e^{-ikr}$ and measure the power spectrum on different scales, expressed either as wavelengths l , frequencies or wave numbers $k = 1/l$, [37], see Figure 6.

At early times, in the radiation dominated era, density perturbations are small $\delta \ll 1$ and general relativity linear perturbation theory can be applied. Indeed, the fields are still weak, and it is possible to obtain the evolution of the density perturbations by using special relativity fluid mechanics and Newtonian gravity (Poisson equation) with a relativistic source term, [13],

$$\nabla^2 \Phi = 4\pi G(\rho + 3p/c^2), \quad (15)$$

which leads to the following evolution of the density field

$$\ddot{\delta} + 2\frac{\dot{a}}{a}\dot{\delta} = 32\frac{\pi}{3}\rho_0\delta. \quad (16)$$

From equation 16, one sees that during radiation domination the growth is slow $\delta \sim \ln(a)$, being $a(t)$ the scale factor in the FLRW metric. After matter-radiation decoupling, matter dominates the background density and the radiation pressure drops to zero, leading to a linear growth in density perturbations $\delta \sim a$. This discussion is only valid for perturbations outside the horizon, [37][35]. Nevertheless, in a combined picture of collisionless matter in a radiation background there is a mode of perturbations inside the horizon where the collisionless (non-relativistic) matter component of density ρ_m is perturbed relative to the relativistic radiation component of density ρ_r . This leads to a perturbations growth mode of $\delta \sim 2/3 + a/a_{eq}$, where a_{eq} is the scale factor at matter-radiation equality. For $a < a_{eq}$ the (cold) matter perturbation is “frozen”, $\delta \sim \text{constant}$, while for $a > a_{eq}$ the matter perturbation grows linearly with $\delta \sim a/a_{eq}$. The overall behaviour (Mészáros effect) is therefore similar to the effects of pressure on a coupled fluid: for scales greater than the horizon, perturbations in matter and radiation can grow together, but this growth ceases once the perturbations enter the horizon, [38].

The perturbations enter the horizon in both the radiation-dominated and the matter-dominated epochs. The difference in the growth rate in these epochs set two important scales in the power spectrum of density perturbations. These are the size of the horizon at matter radiation equality, below which the power spectrum of density fluctuations flattens, and the size of the horizon when dark matter freezes out, see Figure 6. Small scales become non-linear first, $\delta \geq 1$ and form gravitationally bound objects that decouple from the overall expansion. This leads to a picture of hierarchical structure formation with small scale structures (like stars and galaxies) forming first and then merging into larger structures (clusters and superclusters of galaxies).

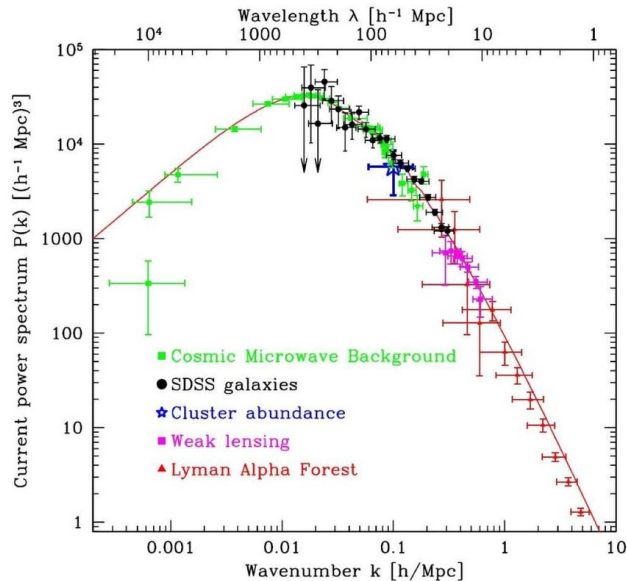


Figure 6: Matter power spectrum $P(k)$ versus wave number extrapolated to $z = 0$, from various measurements of cosmological structure. The solid line shows the Λ CDM best fit, [39]

The most common approach in the literature to describe structure formation in the non-linear regime are N-body simulations, [40], since there is no analytic solution for the evolution of the density field in the strongly coupled case. Later in this thesis, section 2.2.2, these methods will be analyzed in some detail. The formation of non-linear dark matter halos is understood due to its hierarchical nature. In Λ CDM, dark matter halos form in essentially the same way regardless of mass and the formation epoch. The slope of the power spectrum changes as a function of length scale, see Figure 6, but the final dependence of $P(k)$ in k is still monotonic for cold dark matter, [41]. On the other hand, the formation of the first baryonic objects involves a number of physical processes, and so is much more complicated to depict. Also, if dark matter were not cold but warm $x_f \sim 3$ or hot $x_f \ll 3$, the power spectrum would significantly differ from the CDM case, presenting a cut-off at large k that would prevent the formation of small dark matter halos at high redshift, in contradiction with observations of the Lyman- α forest, [42].

1.2.3 Dark Matter substructure

Due to the hierarchical structure formation, the main halos of galaxies are expected to host a number of substructures. Non-virialized structures have been both predicted in N-body simulations, [43], and observed in stellar surveys data, [44]. The precise determination of the dark matter substructure, in particular in the Milky Way, might be of crucial importance for dark matter searches, [45], since they include the phase space distribution of dark matter particles in their observables. Some examples of dark matter substructure are:

- **Subhalos:** These are halos bounded to larger halos. A large fraction of light subhalos does not accrete sufficient matter to form stars and remain dark. In the CDM picture, these can have masses in the range $\sim 10^{-4}M_\odot - 10^{10}M_\odot$ and lead to local regions of overdensities that can affect the predictions of direct and indirect dark matter searches. Its properties are determined by the subhalo mass function, depending on the dark matter density profile and concentration parameter of the subhalos, [45].
- **Streams:** In the same way that the gravitational pull of the moon creates tides on Earth, the gravitational pull of the Milky Way creates tides too. It is well known that globular clusters lose stars to form tidal streams, such as the Sagittarius, Orphan and Monoceros streams, orbiting around the Milky Way, [46], see Figure 7. A recent study found a new stream in the outskirts of the Milky Way, the stream S1, [47]. This suggests the possibility of analogous structures formed of dark matter wrapped around the Milky Way. If this were the case, then the dark matter particle velocities in a given stream would be coherent, with

$$f_{stream}(\vec{v}) = \delta^3(\vec{v} - \vec{v}_{stream}) \quad (17)$$

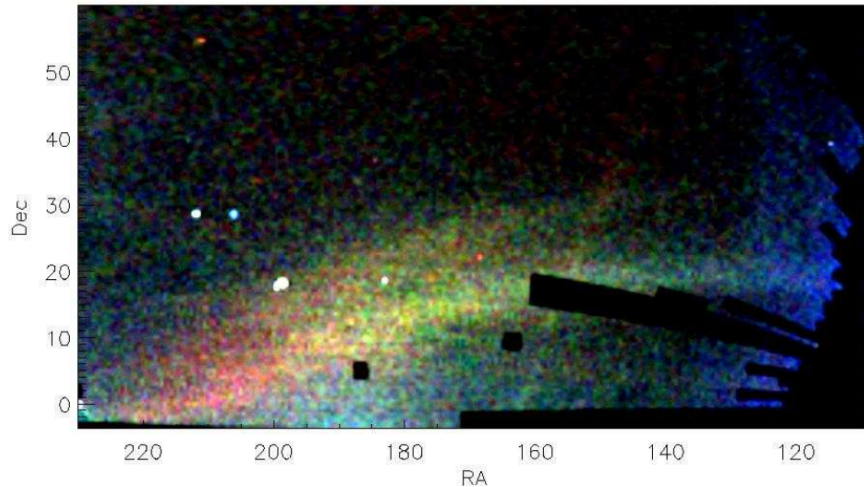


Figure 7: The field of streams imaged by SDSS, [46]. On the x axis, the right ascension (RA), and on the y axis, the declination, both in degrees. In yellow and red colours, the two tails of the Sagittarius stream, note the bifurcation around $RA \sim 180^\circ$. The Orphan stream is the thin vertical line at $RA \sim 160^\circ$ and the Monoceros stream is clearly visible in blue on the right of the image.

- **Debris flow:** This dark matter substructure consists of the sum of different debris materials from a subhalo infalling in the Milky way orbit, [14]. Its particle constituents would have the same speed but different directions, and simulations suggest that debris flow would constitute a significant fraction of the high-speed particles in the Milky Way, as we will see in section 2.2.2
- **Dark disc:** A dark disc may form if subhalos merging with the Milky Way are disrupted by its baryonic disc, resulting in a concentration of dark matter on the plane that rotates in the same direction as the Sun, [14]. Its existence would provide an excess of slow-moving particles in the solar neighborhood. Although the existence of a dark disc was suggested by simulations, [48], recent works disfavour it and constrain its possibilities, [49].

To summarize, there are different types of non-virialized dark matter substructure with different phase space distributions that could be present in the Milky Way and cause an impact on dark matter searches.

2 Dark Matter in the Milky Way

In this section, we review in more detail our current knowledge of the dark matter local density and velocity distribution in the Milky Way, particularly in the solar neighbourhood.

2.1 The Dark Matter density

There are two independent methods to obtain the radial dark matter density profile in the Milky Way $\rho_{DM}(r)$. One option is to fit the predictions of dark matter-only N-body simulations. In this way the Navarro-Frenk-White (NFW) profile, [50], and the Einasto profile, [51] are obtained. Alternatively, the Burkert profile is extracted from the rotation curve of the galaxy, [52]. These methods lead to incompatible results, since N-body simulations show a cuspy profile at the center of the galaxy and the Milky Way rotation curve indicates a flat profile at the center. This discrepancy is known as the core-cusp problem, and alternatives such as hydrodynamical simulations including the effects of baryonic physics, 2.2.2, or self-interacting dark matter models seem to provide solutions to this problem, see [53] for a detailed review. We are particularly interested in the local dark matter density ρ_{loc} in the solar neighborhood, since this is the quantity that affects the prediction of local dark matter searches, specifically neutrino experiments, 3.2.1, and direct detection experiments, 3.3, that will be studied later in this manuscript. Two complementary analyses are carried to measure this value, see Figure 8. Local measurements look at the motion of tracers not farther than 10 kpc away from the sun. These are metal-poor stars that are believed to trace the dark matter component in the galaxy, since both dark matter and metal-poor halo stars are accreted to the Milky Way via mergers of galaxies. The dominant uncertainties here come from the kinematics of the tracers and the surface density of baryons, and current studies go from no dark matter at all towards values so large as $0.85 \text{ GeV}/\text{cm}^3$, [54][55]. The second analysis consists in global measurements, which model the mass distribution of the galaxy from the rotation curve and infer the dark matter density at the solar distance from the galactic center. The uncertainties here arise from the precise determination of the Milky Way mass components and the simplifying assumptions made for the dark matter density profile. These studies however obtain more restricted values in the range $0.2\text{-}0.4 \text{ GeV}/\text{cm}^2$, [56][57].

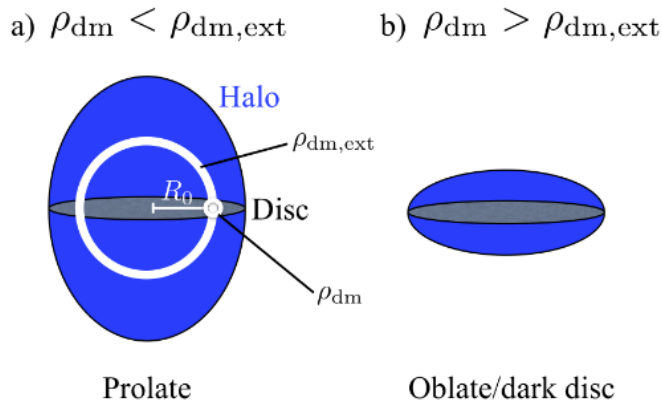


Figure 8: Schematic representation of local vs global measures, taken from [57]. The Milky Way disc is marked in grey and the dark matter halo in blue. If the local measure is smaller than the global measure $\rho_{dm} < \rho_{dm,ext}$, this indicates a prolate dark matter halo. On the other hand, if $\rho_{dm} > \rho_{dm,ext}$, this would imply an oblate halo, or the existence of dark matter substructure near the Milky Way, such a dark disc, [48].

The canonical value in the community is $0.3 \text{ GeV}/\text{cm}^3$, but recent works suggest $\mathcal{O}(1)$ uncertainties, such as [58]. Nevertheless, as we will discuss in section 5.1, the total dark matter rates in experiments depend linearly on the local density of dark matter particles, and therefore this uncertainty, though of course relevant for making precise predictions, can be addressed by rescaling the signal normalization.

2.2 The Dark Matter velocity distribution

A proper understanding of the velocity distribution of dark matter particles is crucial to determine both its particle nature and cosmological history. Furthermore, as we will discuss in section 5.1, its impact on the dark matter scattering rates at experiments is difficult to track, being a source of uncertainty. In this section, we review our current knowledge about the dark matter velocity distribution.

2.2.1 The Standard Halo Model (SHM)

The benchmark dark matter velocity distribution used not only in WIMPs, but also axion searches, [59], is a truncated Maxwell-Boltzmann (MB) velocity distribution at the galactic escape velocity. The Standard Halo Model (SHM) consists in a dark matter density profile given by the isothermal sphere and a truncated Maxwell-Boltzmann velocity distribution. The Maxwell-Boltzmann velocity distribution can be obtained in several independent ways, [60][43][55][16]. We would like to comment that there is confusion in the literature regarding the derivation of the Maxwell-Boltzmann velocity distribution in the SHM used at dark matter searches. Some studies model the dark matter density by an isothermal sphere, motivated by the observation of flat rotation curves, where the velocity dispersion is obtained by integrating up to the virial radius the mass of the galaxy, and later use the Eddington inversion method to infer the Maxwell-Boltzmann velocity distribution, [55]. Other studies

just consider a generic Maxwell-Boltzmann distribution with three parameters: the normalization constant, the Milky Way escape velocity, and the peak speed v_0 . The peak speed is consistent with the circular speed of rotation curves in the case of the isothermal model, or it can be taken to be $v_0 = \sqrt{\frac{2}{3}}\sigma_v$, where the velocity dispersion $\sigma_v = \sqrt{\langle v^2 \rangle}$ can be obtained from solving the spherically symmetric Jeans equation, [43]. Some parametrizations maintain a sharp truncate at v_{esc} while others smooth it *ad-hoc* with an additional exponential term, [61]. Furthermore, the isothermal sphere can be obtained by solving the collisionless Boltzmann equation, taking a maxwellian profile as an ansatz, or independently from solving the hydrostatic balance equation for the isothermal equation of state $P \propto \rho$, to obtain the gravitational potential Φ , that allows to compute the isothermal profile by solving the Poisson equation, [62]. In the following, we will describe only one of the approaches used in the literature: obtaining the isothermal sphere from the assumption of the maxwellian ansatz, later determining the velocity distribution via Eddington's method.

The isothermal sphere model can be obtained by taking a Maxwell-Boltzmann distribution $f = C \exp(\mathcal{E}/\sigma_v^2)$, with σ_v^2 being the velocity dispersion of the particles in the system, and energy per unit mass $\mathcal{E} = v^2/2 + \Phi(\vec{r})$, as an ansatz of the particles phase space distribution $f(\vec{r}, \vec{v}, t)$ to help solve the collisionless boltzmann equation

$$\frac{\partial f}{\partial t} + (\vec{v} \cdot \nabla)f - (\nabla\Phi \cdot \nabla_v)f = 0, \quad (18)$$

where Φ is the gravitational potential that the collisionless particles are subject to. Equation 18 would therefore describe the evolution in phase space of an incompressible fluid of dark matter particles subject to a gravitational potential $\Phi(r)$. As a historical note, equation 18 is misleadingly sometimes called Vlasov equation, though Vlasov took it initially from Boltzmann to track the evolution of a plasma of electrically charged particles, [63]. Integrating out equation 18 in velocity space, the mass density yields

$$\rho(\vec{r}) = \int d^3\vec{v} f(\vec{r}, \vec{v}) = \rho_c \exp(-\Phi(\vec{r})/\sigma_v^2). \quad (19)$$

Assuming spherical symmetry and the the scale invariant ansatz $\rho = Ar^\alpha$, one can solve the Poisson equation

$$\Delta\Phi = \frac{1}{r^2} \frac{d}{dr} \left\{ r^2 \frac{d\Phi}{dr} \right\} = 4\pi G\rho(r), \quad (20)$$

and the density profile of the isothermal sphere yields

$$\rho(r) = \frac{\sigma_v^2}{2\pi G} \frac{1}{r^2}. \quad (21)$$

Now, we can use Eddington's inversion method, [64]. In the maximally symmetric case of an isotropic and spherically symmetric halo of self-gravitating dark matter particles with energies per unit mass $\mathcal{E} > 0$, the angular momentum is not relevant and the phase-space distribution function can be described as a function of the energy only $f(\vec{r}, \vec{v}) = f(\mathcal{E})$. By performing an Abel inversion of 19, one can derive the unique steady-state solution of the collisionless Boltzmann equation 18 for a given density-potential

$$f(\mathcal{E}) = \frac{1}{\sqrt{8\pi^2}} \left[\frac{1}{\sqrt{\mathcal{E}}} \left(\frac{d\rho}{d\Psi} \right)_{\Psi=0} + \int_0^{\mathcal{E}} \frac{d\Psi}{\sqrt{\mathcal{E} - \Psi}} \frac{d^2\rho}{d\Psi^2} \right], \quad (22)$$

which is the Eddington formula. It is important to notice that ρ refers to the dark matter density, while $\Psi = \Phi_0 - \Phi(r)$ is the total relative potential of the system. The first term $\propto 1/\sqrt{E}$ leads to a divergence in the velocity distribution at $v \rightarrow v_{esc}$ and therefore must be dropped, though more sophisticated methods to regularize it have been proposed, [65][66]. Using the Eddington inversion method, the dark matter velocity distribution can be obtained as $f_{\vec{r}}(\vec{v}) = f(\vec{r}, \vec{v})/\rho(\vec{r})$, which leads to the result

$$f_{\text{SHM}}(\vec{v}) = \frac{1}{(2\pi\sigma_v^2)^{3/2}N_{esc}} \exp\left(-\frac{v^2}{2\sigma_v^2}\right) \text{ for } v \leq v_{esc}, \quad (23)$$

where the velocity dispersion σ_v^2 of the dark matter particles of the Milky Way dark matter halo can be obtained integrating the mass density in equation 21 over the Milky Way volume (up to the virial radius), and equating to the mass of the dark matter halo in the galaxy, which is experimentally known. Its value is $\sigma_v \approx 156$ km/s, [67]. The escape velocity is taken to be $v_{max} = 544$ km/s, according to [68]. The normalization factor N_{esc} is,

$$N_{esc} = \text{erf}\left(\frac{v_{esc}}{\sqrt{2}\sigma_v}\right) - \sqrt{\frac{2}{\pi}} \frac{v_{esc}}{\sigma_v} \exp\left(-\frac{v_{esc}^2}{2\sigma_v^2}\right) \quad (24)$$

depending on the escape velocity v_{esc} and velocity dispersion σ_v . Notice that the truncation at the Milky Way escape velocity has been done *a posteriori*, which leads to a sharp cut-off in the tail of the distribution. But this is not the only nor the most important caveat of the SHM. First, the mass density in equation 21 diverges for $r \rightarrow 0$, which leads to a diverging mass in the Milky Way. The SHM behaves bad in the central regions of galactic structures, where the circular speed is known to provide a very poor estimate of the velocity dispersion, due to the influence of the baryonic disc. Furthermore, the NFW and Einasto profiles are not proportional to r^{-2} but to r^{-3} for large radii. Moreover, the Maxwell-Boltzmann is not a generic solution to the Boltzmann equation 18 for more realistic galactic gravitational potentials including the effects of baryonic physics.

Despite all this discussion, the SHM is expected to provide a good first order approximation at the scales of the solar neighbourhood. It is however necessary to look closely at the results from N-body simulations 2.2.2 and tracers studies 2.2.3, to understand precisely where does the approximation fails and to get hints from the existence of dark matter substructure discussed in section 1.2.3.

2.2.2 N-Body simulations

N-body simulations evolve in time the phase space distribution $f(\vec{x}, \vec{v}, t)$ of a set of N particles that are drawn from an initial power spectrum, being therefore able to track directly the dark matter velocity distribution. For cold dark matter, the collisionless Boltzmann equation and the Poisson equation describe the evolution of the gravitational field $\Phi(\vec{x})$

$$\frac{df}{dt} = \frac{\partial f}{\partial t} + \sum_i v_i \frac{\partial f}{\partial x_i} + \sum_i \frac{\partial \phi}{\partial x_i} \frac{\partial f}{\partial v_i}, \quad (25)$$

$$\rho_{\text{DM}}(\vec{x}, t) = \int f(\vec{x}, \vec{v}, t) d^3v, \quad (26)$$

$$\nabla^2\Phi(\vec{x}) = 4\pi G\rho_{DM}(\vec{x}). \quad (27)$$

Here, d/dt is the Lagrangian derivative and ρ_{DM} is the dark matter density. N-body simulations solve this problem by discretizing the distribution function into N phase space elements $\{\vec{x}_i, \vec{v}_i\}$ for $i = 1, \dots, N$. These phase-space regions represent the dark matter particles of the simulation. As an illustrative example, the Aquarius simulation, [69], consider up to 1 billion dark matter particles (10^9), but there are way more dark matter particles in the Milky Way

$$M_{\chi,MW} \sim 10^{12}M_{\odot}, \quad m_{\chi} \sim 10^{-37} \text{ GeV}$$

$$\Rightarrow \sim 10^{52} \text{ dark matter particles in the Milky Way}$$

This sets a discrepancy of roughly 10^{43} orders of magnitude between reality and simulation. Therefore, the conclusions drawn from N-body simulations are limited by the phase space resolution. Another caveat is that the dark matter velocity distribution is usually obtained from galaxies with similar characteristics to the Milky Way, but such galaxies may not present a solar system at the very same distance from the galactic center as we do. N-body simulations are however useful as they allow to determine the phase space distribution of dark matter in the non-linear regime and study the properties of Milky Way-like halos under the CDM paradigm. Precisely, equations 25, 26 and 27 allow to trace the dynamics of a system of N particles subject to the potential imposed by the particles phase space distribution.

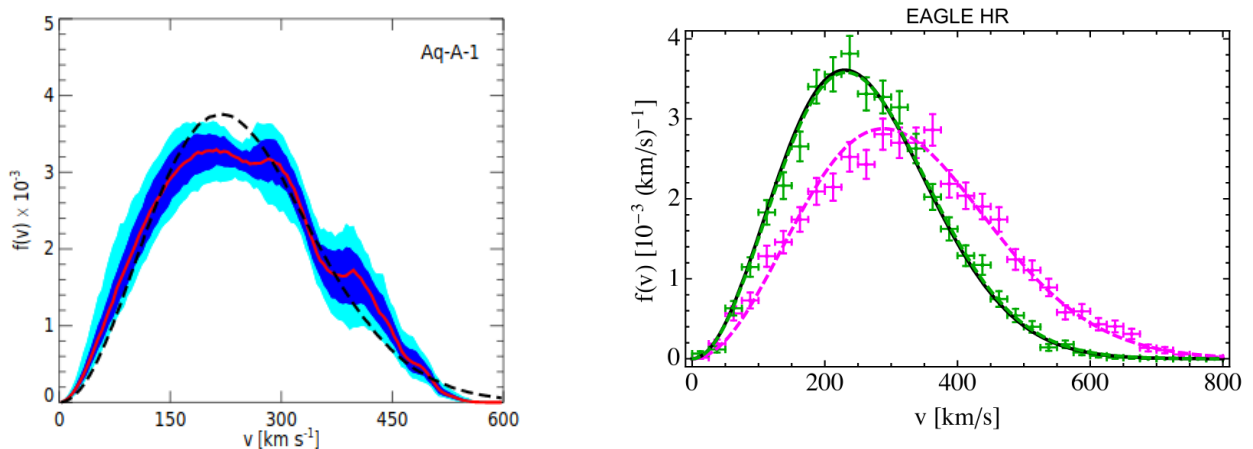


Figure 9: On the left, the dark matter speed distribution obtained from the dark matter-only Aquarius simulation. The dark and light blue contours enclose 68 and 95 per cent of all the measured distributions at each velocity, [71]. The peaks at high velocities might be an indication of a debris flow of dark matter particles. On the right, the results from the hydrodynamical EAGLE simulation, where the green line represents the closest simulated velocity distribution to the SHM (in solid black), and the pink one the largest deviated velocity distribution obtained, [72].

There are two types of simulations: dark matter-only simulations and hydrodynamical simulations, which include the effect of baryonic physics, see Figure 2.2.2. Hydrodynamical simulations seem to provide a more realistic description of the gravitational potential, and

could solve the core-cusp problem, [53], regarding the discrepancy of the dark matter-only simulations motivated density profiles, such as NFW, which predict a cuspy profile in the center of the galaxy, and the extracted density profiles from the rotation curve of the galaxy, flat in the center. Nonetheless, dark matter-only simulated galaxies seem to deviate less with respect to kinematical studies of tracers, [70][58], which will be discussed in next section 2.2.3 and are in better agreement with self-consistent theoretical methods of phase space distribution functions predictions, based in the Eddington inversion, [43]. Moreover, the resolution is better than for hydrodynamical simulations, [55].

2.2.3 Tracers observations

The dark matter velocity distribution in the solar neighbourhood can be inferred from the study of tracers, low-metallicity stars not farther than 10 kpc from the sun, which are believed to trace the dark matter component, [14]. A study of such type is [70], where the authors use the distribution of accreted stars in SDSS and Gaia, [44], to demonstrate that a non-trivial fraction of the dark matter halo within Galactocentric radii of 7.5-10 kpc is in substructure. They develop a two-component model for the dark matter velocity distribution, where the observation of a metal-poor and isotropic stellar halo is likely associated with tidal debris from the oldest luminous mergers that built up the Milky Way, while the anisotropic component at intermediate metallicities is due to tidal debris from a more recent merger. Based in this two-component separation of the velocity distribution, it is possible to derive the Jeans equations in spherical coordinates, under the assumptions, for both components, of spherical symmetry and uncorrelated spherical velocities. Furthermore, the isotropic distribution is assumed to be in steady state, while the anisotropic component is not, and their velocities have vanishing mean at present-day.

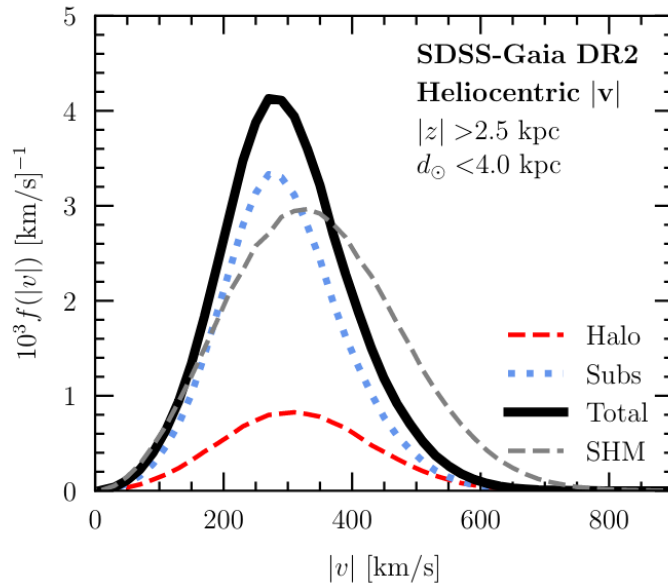


Figure 10: Dark matter velocity distribution in the SDSS-Gaia DR2 joint analysis at [70]. The dotted blue line represents the contribution of the dark matter component that is in substructure, and the red dotted line the dark matter halo contribution. In solid black the sum of both distributions is shown.

In this study, the authors perform a mixture model likelihood analysis, allowing to statistically identify the individual populations of accreted stars over the full metallicity range of the sample. The summed velocity distribution appears to be more conservative than the SHM, see Figure 10. A similar analysis using data provided by the GAIA mission, [44], proposes a refinement of the SHM, named the SHM⁺⁺, based in the consideration of a strongly radially anisotropic population of our stellar halo, the so-called *Gaia Sausage*. This new model update the usual parameters of the SHM: the circular rotation speed, v_0 , the local DM density ρ_0 and the escape speed v_{esc} , and adds two new parameters: the sausage anisotropy β and the sausage fraction ν , see Table 1.

SHM		
Local DM density	ρ_0	0.3 GeV cm^{-3}
Circular rotation speed	v_0	220 km s^{-1}
Escape speed	v_{esc}	544 km s^{-1}
Velocity distribution	$f_{SHM}(\vec{v})$	Equation 23
SHM ⁺⁺		
Local DM density	ρ_0	$0.55 \text{ GeV} \pm 0.17 \text{ cm}^{-3}$
Circular rotation speed	v_0	$233 \pm 3 \text{ km s}^{-1}$
Escape speed	v_{esc}	544 km s^{-1}
Sausage anisotropy	β	0.9 ± 0.05
Sausage fraction	η	0.2 ± 0.1
Velocity distribution	$f_{SHM^{++}}(\vec{v})$	Equation 28

Table 1: Updated parameters of the SHM, according to [58]

The anisotropic component of the Milky Way is taken into account by splitting the velocity distribution into two components, in a similar way as for the SDSS-Gaia DR2 study: A Maxwell-Boltzmann-like component of the nearly round dark halo, which weights as 80% of the total dark matter velocity distribution of the Milky Way, and the velocity distribution of the Gaia sausage, which weights 20%, see Figure 11. The anisotropic velocity distribution of the Gaia component takes the form

$$f_S(\vec{v}) = \frac{1}{(2\pi)^{3/2} \sigma_r \sigma_\theta^2 N_{S,esc}} \exp\left(-\frac{v_r^2}{2\sigma_r^2} - \frac{v_\theta^2}{2\sigma_\theta^2} - \frac{v_\phi^2}{2\sigma_\phi^2}\right) \times \theta(v_{esc} - |\vec{v}|), \quad (28)$$

where the velocity dispersion in spherical coordinates are functions of the circular velocity v_0 and the anisotropic parameter β , and there is a normalisation constant $N_{S,esc}$, which is an anisotropic analogue of equation 23.

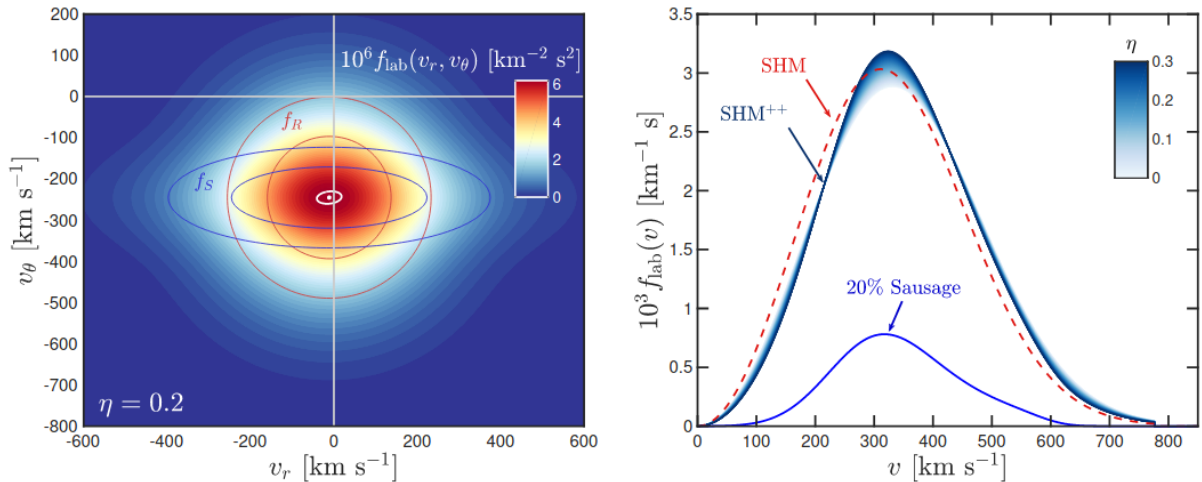


Figure 11: On the left, the velocity distribution for the SHM⁺⁺ in the radial and horizontal directions on the Earth frame. The SHM like component is denoted as $f_R(v)$, and the Sausage component, $f_S(v)$, whose radial anisotropy is clearly visible. On the right, the dark matter velocity distributions for the SHM (red dashed) and the SHM⁺⁺ (blue), shaded for different sausage fraction components η . The total velocity distribution is slightly more aggressive than the SHM, [58].

Although data provided by the SDSS and Gaia stars catalogue indicate the existence of dark matter substructure in the Milky Way, in particular, a dark matter anisotropic component, these studies present significant differences not only among them but also with the N-body simulated Milky Way-like galaxies discussed in previous section 2.2.2, obtained from an initial power spectrum of density fluctuations. The main caveat of these kinematical reconstructions of the dark matter halo is that they rely on observational data which has uncertainties in the kinematics of stars and the surface density of baryons, as we already discussed for the local dark matter density determination in section 2.1. Furthermore, both isotropic and anisotropic components are not well correlated in the case of recent mergers. Another arguable argument disfavoring them is that dark structures such as subhalos are not taken into account.

2.2.4 Maximum entropy velocity distribution

Here, we present a new method to compute the dark matter velocity distribution in an independent way from the methods shown above. We will make use of the *principle of maximum entropy*, [16], which states that the probability distribution that better represents the current state of knowledge of a system is the one that maximizes the *Shannon entropy*, [19], see Appendix B.1, while reproducing the precisely known prior data about the system. In other words, it means that given some prior information about our physical system, the *maximally uninformative* probability distribution about the system among the set of all distributions satisfying the prior, is the one with largest entropy. The Maxwell-Boltzmann velocity distribution can be obtained by this means, under the constraint of conservation of the expectation value (average) of the energy $E(v^2)$ and the logarithm of the velocities

$E(\log(v))$. The constraint in the logarithm is discussed by Jaynes in [73], where he argues that the differential entropy is only an appropriate continuum generalization of the discrete Shannon entropy if the phase-space discretization that one chooses is uniform. We will therefore construct the maximally entropic velocity distribution of the Milky Way dark matter halo, under the basic restrictions of the dark matter velocities to be smaller than the escape velocity of the Milky Way, the conservation of the expected value of the energy, and the velocity distribution to be positive-defined. If we further impose isotropy, the problem is the following

$$\text{Maximize : } H(f) = - \int dv f(v) \log \left(\frac{f(v)}{m(v)} \right) \quad (29)$$

subject to:

$$\int_v f(v) dv = 1$$

$$\int_v f(v) v^2 dv = K$$

$$0 \leq v \leq v_{max}$$

where the discretization of the phase-space is encoded in $m(v)$. We want to describe the statistics of a system in velocity space \vec{v} , using a probability distribution on the modulus of the velocity vector $|\vec{v}|$, assuming isotropy. In D-dimensions, the density of states with velocity between v and dv is $\propto v^{D-1}$, so that in 3D we need to choose $m(v) = \text{constant} \cdot v^2 [\frac{km}{s}]^{-1}$. From the Karush-Kuhn-Tucker conditions, see Appendix A.2, the lagrangian is:

$$\begin{aligned} \mathcal{L}(v, \vec{\lambda}, \vec{\mu}) = & - \int f(v) \log(f(v)) dv - \lambda_0 \left(\int f(v) dv - 1 \right) - \lambda_1 \left(\int f(v) v^2 dv - K \right) \\ & + 2 \int f(v) \log(v) dv - \mu_1 (v - v_{max}) + \mu_2 v, \end{aligned} \quad (30)$$

and leads to

$$f(v) = e^{-\lambda_0} v^2 e^{-\lambda_1 v^2}, \quad (31)$$

which is a maxwellian profile as in the SHM. The difference in the parameters depend on the lagrange multipliers λ_0 and λ_1 , which are determined by

$$e^{-\lambda_0} \left[\frac{\sqrt{\pi} e r f(\sqrt{\lambda_1} v_{max})}{4 \lambda_1^{3/2}} - \frac{v_{max} e^{-\lambda_1 v_{max}^2}}{2 \lambda_1} \right] = 1 \quad (32)$$

$$e^{-\lambda_0} \left[\frac{3 \sqrt{\pi} e r f(\sqrt{\lambda_1} v_{max})}{8 \lambda_1^{5/2}} - \frac{v_{max} e^{-\lambda_1 v_{max}^2} (2 \lambda_1 v_{max}^2 + 3)}{4 \lambda_1^2} \right] = K \quad (33)$$

and thus can only be obtained if K is known. If the energy of the dark matter particles of the system is just given by their non-relativistic kinetic energy $E = m_\chi v^2/2$, we only need to determine the velocity dispersion of the dark matter particles of the Milky Way

halo to solve the system of equations 32 and 33. We could analogously to the proceeding described in 2.2.1, obtain consistently with our distribution the velocity dispersion of the dark matter particles by first solving the collisionless Boltzmann equation and then integrate the density profile over the volume of the galaxy. This process is however technically difficult and we leave it for future research. We take as a prior information of our system that the velocity dispersion of the dark matter particles is given by the value from [67], where the velocity dispersion is calculated by integrating the mass of the galaxy using a density profile corresponding to an isothermal sphere, obtaining $\sigma_v \approx 156$ km/s.

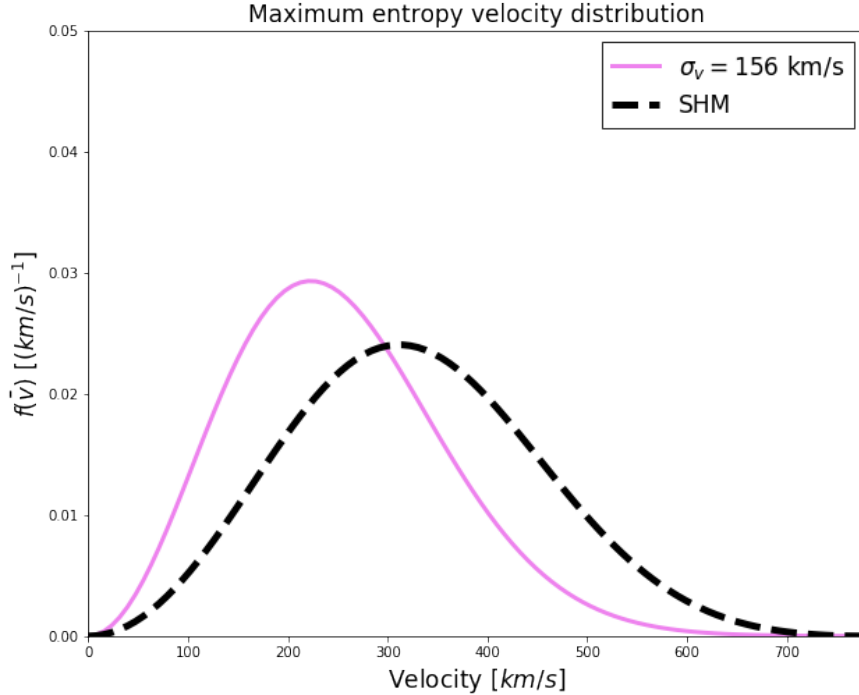


Figure 12: Maximally entropic velocity distribution for a system of dark matter particles with velocities $v \leq v_{esc}$, in the Earth frame, for the value of the velocity dispersion according to [67].

This approach is interesting because it does not apply an unphysical truncation at the Milky Way escape speed, but rather include this restriction in the velocity of the dark matter particles *a priori*. Furthermore, it allows to derive the maximally uninformative distribution of dark matter particles from a set of prior initial assumptions, therefore is particularly appropriate for halo-independent analyses of dark matter searches sensitive to uncertainties in the velocity distribution, like those that we will perform in section 5. The principle of maximum entropy will be used in section 6 in a different way, we refer the reader there for a bayesian interpretation of the method. Nevertheless, this technique is not complete, since the derivation of the maximally entropic velocity distribution should be performed in 3 dimensions, without implying automatically isotropy, as the directionality of the dark matter particles is crucial in current direct detection dark matter searches that aim to detect an annual modulation signal, [74].

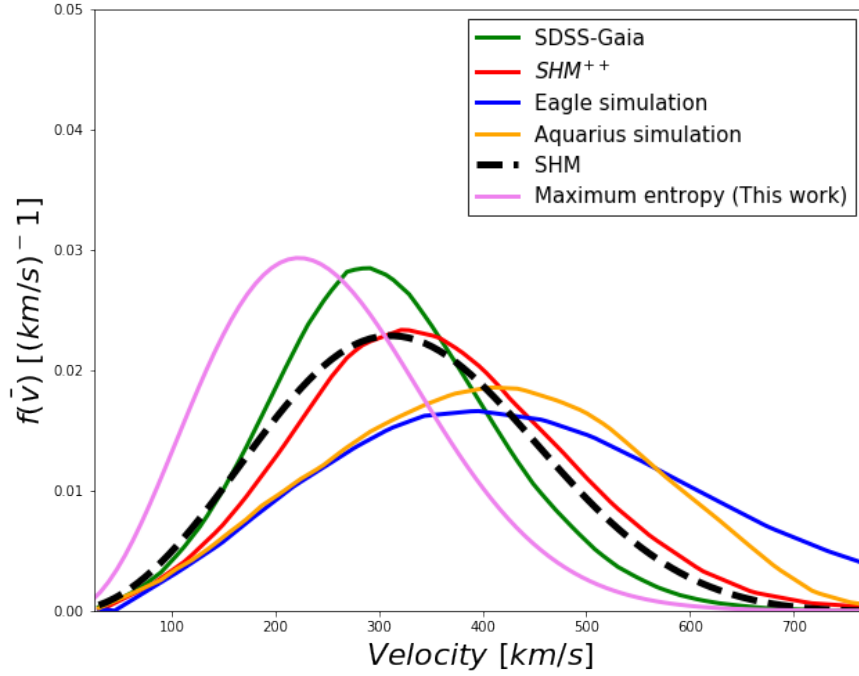


Figure 13: Dark matter velocity distribution according to the different studies discussed in this thesis, in the Earth frame. In dotted black, the SHM, [23](#). In green, the SDSS-Gaia DR2 study, [\[70\]](#). In red, the SHM⁺⁺ study, [\[58\]](#). In orange and blue, dark matter-only and hydrodynamical simulations results, respectively, [\[69\]](#)[\[72\]](#). In pink, our result obtained by using the principle of maximum entropy and the velocity dispersion of the standard halo model, $\sigma_v = 156$ km/s

To conclude, we have presented several alternative methods to obtain the dark matter velocity distribution in the solar neighbourhood, all of them presenting incompatibilities, see [Figure 13](#). How does this uncertainty affect the predictions of dark matter observables at experiments? This is what we will study in the following sections, starting by describing the different dark matter searches taking place nowadays.

3 Dark Matter searches

There are three main approaches to search for dark matter. Collider searches attempt to produce new neutral particles, indirect searches look at astrophysical sources of standard model particles that could be explained by the annihilation of dark matter particles, and direct searches measure the recoil of dark matter particles in a detector placed on Earth, usually operated underground. In this section we give a general overview of the state of the art of dark matter searches, focusing in neutrino and direct detection searches.

3.1 Collider searches

The search for dark matter at colliders is the search for missing energy. The main attempts to find dark matter at the LHC have been performed in the framework of effective field theories (EFT), [75], and simplified models, [76]. EFT's present some advantages w.r.t simplified models, for example, they have a limited number degrees of freedom (interaction scale, dark matter mass) and allow for a model independent comparison with direct detection searches, while simplified models require at least four model parameters: the mediator mass, dark matter mass and coupling strengths of the mediator to the dark sector and the standard model ($m_{mediator}, m_\chi, g_\chi, g_q$), and don't allow for a proper model independent comparison with direct detection experiments. Nevertheless, EFT's are not valid for current energy scales at colliders $\sqrt{s} = 13$ TeV, since they require that the center of mass energy of the collision is smaller than the mediator mass $q^2 \ll m_{mediator}^2$. In the framework of simplified models, there are two differentiated dark matter searches : mono-X searches and mediator searches. The first consists on looking for single jet, photon, higgs, Z, etc., events, [77], while mediator searches look for resonances like Z' mediator in dijet or dilepton events, [78], see Figure 14.

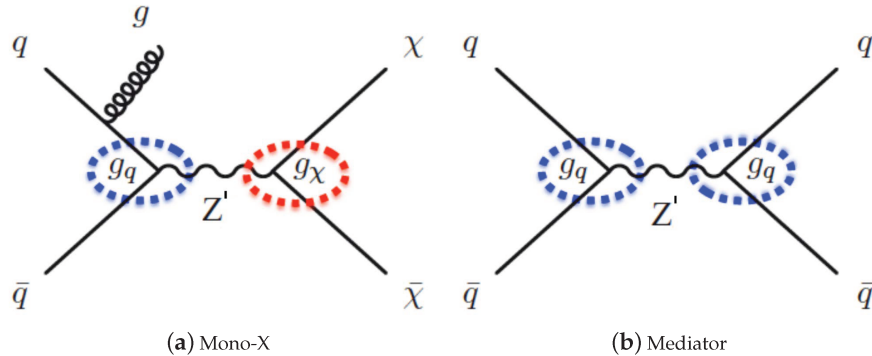


Figure 14: (a) Mono-X searches. Dark matter interaction with SM particles is mediated by Z' and therefore there are two couplings parameters : the coupling of Z' to standard model particles g_q and the coupling to the dark sector g_χ . (b) Mediator searches. The dark matter mediating particle Z' is produced and decaying back to standard model particles. The only model parameters here are the Z' mass and the coupling of Z' to standard model particles g_q

The results presented by LHC present a strong dependence on the choice of the couplings g_χ, g_l, g_q to dark matter, standard model leptons and quarks, respectively. Fixing these

values allow for comparison with the dark matter relic density and direct detection limits on the mass-cross section plane $m_\chi - \sigma$, see Figure 15. Collider bounds are more stringent than direct detection limits at low dark matter masses $m_\chi \leq 6$ GeV, in the spin-independent case, and in the complete parameter space, in the spin-dependent case, see Figure 14. However, plots are usually presented in the mass-mass plane of the mediator and dark matter particle. The translation of LHC results to direct-indirect detection plots is difficult to interpret, since LHC results only hold for the mediator under consideration and the specific choice of the couplings taken, [79].

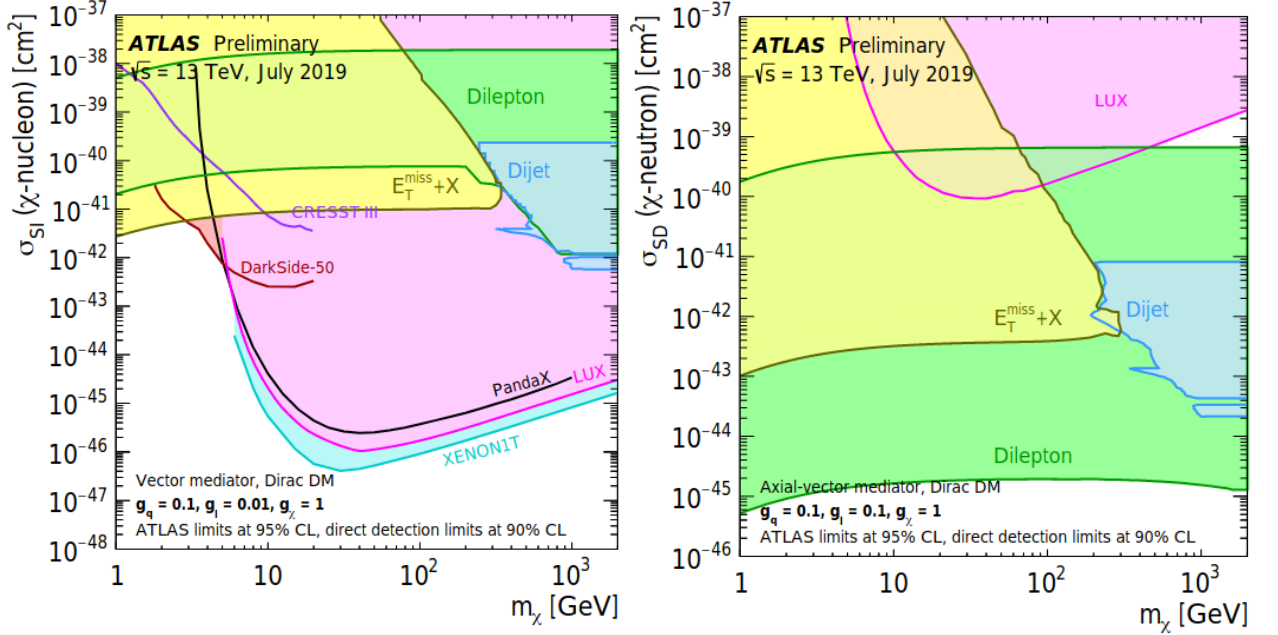


Figure 15: On the left, a comparison of the inferred limits with the constraints from direct detection experiments on the spin independent WIMP–nucleon scattering cross-section in the context of the Z' -like simplified model with leptophilic vector couplings. On the right, the spin dependent results in the case of leptophilic axial-vector couplings. LHC limits are shown at 95% CL and direct-detection limits at 90% CL, [80].

3.2 Indirect searches

If WIMPs are produced thermally, they can annihilate into standard model particles. This allows to analyze if dark matter annihilation (into different channels) could explain some astroparticle physics anomalies, such as the observed gamma ray excess from the center of the galaxy, [81], the positron excess, [82], the antiprotons and antideuterons flux, [83], or an eventual increase of the neutrino flux, [84][21].

Neutrino searches are of particular interest since they provide an alternative search method comparable with direct detection experiments. Could an excess of the solar neutrino flux on Earth-based experiments happen due to dark matter annihilation? This was first suggested in [85][86][87] and in the following we will review the formalism for a latter halo-independent comparison of such signatures with direct detection experiments.

3.2.1 Capture mechanism : Detecting dark matter with neutrino experiments

Dark matter particles can be gravitationally captured in the sun, scattering with the sun nuclei, sinking to the core, where they can annihilate into standard model particles, see Figure 16. This could enhance the solar neutrino flux detectable on earth, [86]. A WIMP with a velocity v_∞ at large distances from the sun has a velocity $w(r) = \sqrt{v_\infty^2 + v_{sun,esc}^2(r)}$ at a distance r from the center of the sun, being $v_{sun,esc}(r)$ the escape velocity of the sun at a radius r .

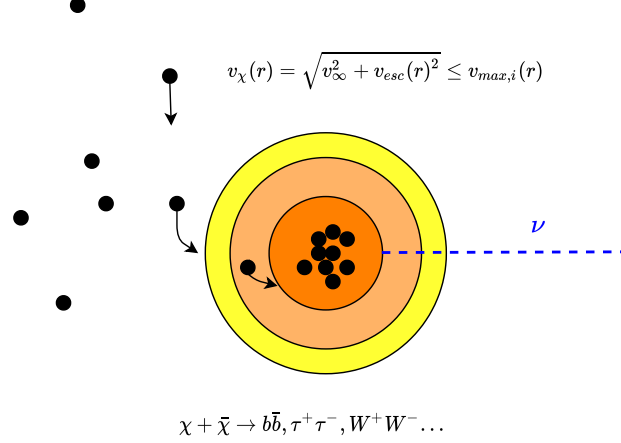


Figure 16: Schematic representation of the dark matter capture mechanism. The dark matter particle velocity at radii r must be smaller than a certain maximum velocity which depends on the recoiling element, see equation 36, in order to be captured. Once accumulated in the core, dark matter particles can annihilate into standard model particles. Some annihilation channels studied by experimental neutrino collaborations are shown, [84][21].

Dark matter particles get gravitationally captured when they transfer enough energy to the nucleus to have velocities lower than $v_{esc,sun}(r)$. This sets a minimum value of the energy that a dark matter particle χ needs to loose by scattering in order to be captured, which is $E_R^{min} = \frac{m_\chi}{2} v_\infty^2$. In the following, we describe the capture formalism of [55]. The capture rate per unit time is defined as

$$\Omega(w) = \nu_N(r) w \int_{E_R^{min}}^{E_R^{max}} dE_R \frac{d\sigma}{dE_R}(w, E_R), \quad (34)$$

where $\nu_N(r)$ is the number density profile of the nucleus N , $\frac{d\sigma}{dE_R}$ (will be described in detail in section 4.2), and the maximal recoil energy $E_R^{max} = 2\mu_{\chi,N}^2 w^2 / m_N$. We use the number density of the solar model AGSS09, [88] and take into account the 29 most abundant elements in the sun for spin-independent scattering. The capture rate per unit volume is

$$\frac{dC}{dV} = \frac{\rho_\chi}{m_\chi} \int_0^{v_{max}(r)} dv^3 \frac{f(\vec{v})}{v} w \Omega(w), \quad (35)$$

where $v_{max}(r)$ arises from the condition $E_R^{min} \leq E_R^{max}$ and is

$$v_{max}(r) = 2 \cdot v_{sun,esc}(r) \cdot \frac{\sqrt{m_\chi \cdot m_N}}{|m_\chi - m_N|}. \quad (36)$$

The total capture rate is obtained integrating equation 35 over the total solar volume

$$C = \sum_i \int_0^{R_\odot} dr 4\pi \cdot r^2 \nu_{N_i} \frac{\rho_{loc}}{m_\chi} \int_0^{v_{max}(r)} dv^3 \frac{f(\vec{v})}{v} (v^2 + v_{sun,esc}(r)^2) \int_{m_\chi v^2/2}^{2\mu_{\chi,N_i}^2 (v^2 + v_{sun,esc}(r)^2)/m_{N_i}} dE_R \frac{d\sigma_{\chi,i}}{dE_R}(w, E_R). \quad (37)$$

Thermal WIMPs can self-annihilate in the core of the sun once their number density n is large enough. The annihilation rate is proportional to n^2 and reads

$$\Gamma_A = \frac{1}{2} C_A n^2, \quad (38)$$

where C_A is the annihilation constant for the sun. Scattering of dark matter particles with nuclei inside the sun can also increase their velocity above the escape velocity of the sun. This process is called thermal evaporation, [89], and must be included in the evolution of the number density of dark matter particles, which can be written as

$$\frac{dn}{dt} = C - C_A n^2 - C_E n, \quad (39)$$

where C_E is the evaporation rate of dark matter particles in the sun. In [90] it is discussed that evaporation of dark matter is only relevant for light dark matter masses $m_\chi \leq 4$ GeV, so this effect will be neglected in the mass range studied by neutrino experiments Super-Kamiokande and Icecube, [21][84]. By specifying the initial condition $n(t=0) = 0$, we can solve equation 39 obtaining

$$n(t) = \sqrt{\frac{C}{C_A}} \tanh\left(\frac{t}{\tau}\right), \quad (40)$$

where $\tau = 1/\sqrt{C \cdot C_A}$ is the equilibration time. After sufficient time $t \gg \tau$, the number of dark matter particles does not vary anymore. Using the estimate of C_A from [12],

$$C_A = 1.2 \cdot 10^{-52} \cdot \left(\frac{\langle\sigma v\rangle}{2.2 \cdot 10^{-26} \text{cm}^3 \text{s}^{-1}}\right) \cdot \left(\frac{m_\chi}{\text{TeV}}\right)^{\frac{3}{2}} \frac{1}{s}. \quad (41)$$

If we take a typical WIMP thermally averaged cross section $\langle\sigma v\rangle \geq 10^{-28} \frac{\text{cm}^3}{s}$, with mass $m_\chi = 100$ GeV and the age of the sun to be $t_\odot = 4.5 \cdot 10^9$, we obtain

$$\left(\frac{t_\odot}{\tau}\right) = \tanh(t_\odot \cdot \sqrt{C \cdot C_A}) \approx 1 \quad (42)$$

when using capture rates currently probed by IceCube or Super-Kamiokande. We can assume $n(t) = \sqrt{\frac{C}{C_A}}$ which leads to the following annihilation rate

$$\boxed{\Gamma_A = \frac{C}{2}} \quad (43)$$

so that, for every two captured dark matter particles there is one annihilation event, i.e. all captured dark matter particles end up annihilating in the core of the sun. In this framework, the number of high energetic solar neutrinos coming from the sun is completely determined by the capture rate of dark matter particles. This statement only holds for certain dark matter-nucleus scattering cross section and velocity distributions. Furthermore, we would like to comment that this approximation is sensitive to the WIMP mass and thermally averaged cross section and could no longer be valid in certain regions of the parameter space. From equation 36, we notice that neutrino telescopes are sensitive to velocities smaller than v_{max} . In section 4 we will see that direct detection experiments probe velocities larger than a certain velocity threshold v_{min} . This aspect of the searches make them complementary, and section 5.5 of this thesis is dedicated to combine their results in a halo-independent way, studying the impact of the velocity distribution.

3.3 Direct searches

A large region of the WIMP parameter space is tested by measuring direct interactions of dark matter particles with a detector placed on Earth. This approach was first proposed in the 80's by Goodman and Witten, where they suggested the possibility of using neutrino experiments to detect particles with coherent weak interactions as well as spin-dependent interactions, [91]. Since then, several experimental efforts have tried to detect dark matter-induced scattering in a detector, based in different target materials and signatures, [92]. But, how large is the WIMP realisable parameter space?. We are aware of astrophysical/cosmological and geophysical constraints that, in principle, would restrict the $m_{DM}-\sigma_{DM}$ region to be studied by direct detection experiments:

- The catalogue of **astrophysical/cosmological constraints** is varied and relies on different types of studies. Gravitational lensing on the galaxy cluster Abell 2218 sets an upper bound on the direct WIMP-nucleon cross section of $\sigma_{DM} < 7 \times 10^{13} \text{pb} \times m_\chi / (\text{GeV}/c^2)$, [93]. Some works set lower bounds on the dark matter particle mass from the number of Milky Way satellites, since the number of satellites predicted decreases with decreasing mass of the dark matter particle. In [94], a lower bound is derived for different dark matter candidates, being the result $m_{DM} \geq 2.3 \text{ keV}$ for a thermal DM particle. This limit is comparable to the ones obtained from the analysis of the DM phase space distribution in dwarf spheroidal galaxies (dSphs). In [95], a conservative lower limit of $m_\chi \geq 0.41 \text{ keV}$ is derived, valid for a fermionic DM particle. Strong interactions of dark matter with baryons also allow to set stringent constraints. These are related to the change in the predicted elements abundances from big bang nucleosynthesis (BBN) and the gamma ray flux produced by the decay of neutral pions presumably originated in collisions between dark matter particles and cosmic rays. These set a limit of $\sigma_{DM} < 9 \times 10^9 \text{ pb} \times m_\chi / (\text{GeV}/c^2)$, [93]. Cosmological constraints arise from the CMB, [96] and the Lyman- α forest, [97]. Another popular cosmologically-motivated bound for fermionic WIMPs is the Lee-Weinberg bound, [98]. The mass of WIMP's should not be lower than $m_\chi \geq 2 \text{ GeV}$, otherwise WIMP's would freeze out too early and their relic density would overclose the universe. A later paper of Kolb and Olive would update such calculation setting new limits of $m_\chi \geq 1.3\text{--}4.2 \text{ GeV}$ for Dirac dark matter, and $m_\chi \geq 4.9\text{--}13 \text{ GeV}$ for Majorana dark matter, [99].

These bound for light and sub-GeV dark matter are however circumvented if dark matter is made of scalar or pseudoscalar particles, if dark matter interacts via a light mediator, [100], or when considering alternative non-thermal scenarios, [101].

- **Geophysical constraints** are also stringent and come from different studies. We discussed in previous section 3.2.1 the WIMP capture mechanism by the sun, but if the WIMP-nucleon scattering cross section is high enough, capture by the Earth may also happen, and the annihilation of WIMPs in the core would lead to a heat flow from the center of the Earth, which is restricted by geophysical measurements, [93]. An analogous analysis for capture in the Moon leads to an exclusion of spin independent cross section of $\sigma_\chi \geq 10^{-37}$

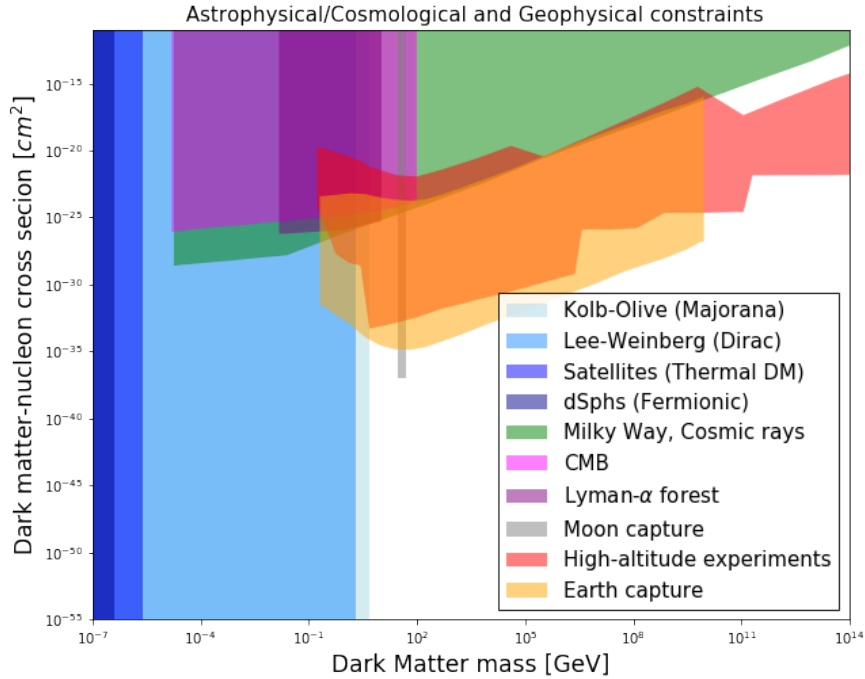


Figure 17: Dark matter mass-cross section bounds. The bounds that are valid only for specific dark matter particle models are shown in gradient blue colors, [99][98][94][95]. The rest of the bounds apply to any dark matter particle, [93][10][97][102]. The white region would represent the model-independent analyzable region of the parameter space available for direct detection experiments. Notice that, of course, the graded blue bounded region need to be explored, since such bounds only apply to specific dark matter models and standard dark matter cosmological freeze out. The neutrino floor is not shown as it depends on the target detector under consideration and it represents a technical challenge but not a real physical bound.

These constraints leave a large room for direct detection experiments to explore low WIMP-baryon scattering cross sections down to the coherent neutrino scattering floor, where the coherent scattering of neutrinos in the target nucleus as a whole would entail a major background reduction technical challenge for direct detection experiments, [103]. Direct detection experiments are based in different detector types. Among these are ionization detectors, based for example in Germanium crystals, like the CoGeNT experiment, [104], light scintillators, based for example in NaI crystals, like DAMA/LIBRA, [105], cryogenic ionization

detectors, based for example in Germanium, like CDMS, [106], liquid noble experiments, usually based in liquid Xenon, like XENON1T and PandaX, [107][108], or bubble chambers, filled with C_3F_8 in the case of PICO, [109]. Since the detectors, signatures probed, and data taking/analysis architectures are wide and varied among experiments, the sensitivity reach in the dark matter mass-cross section is different for each experiment, see Figure 18.

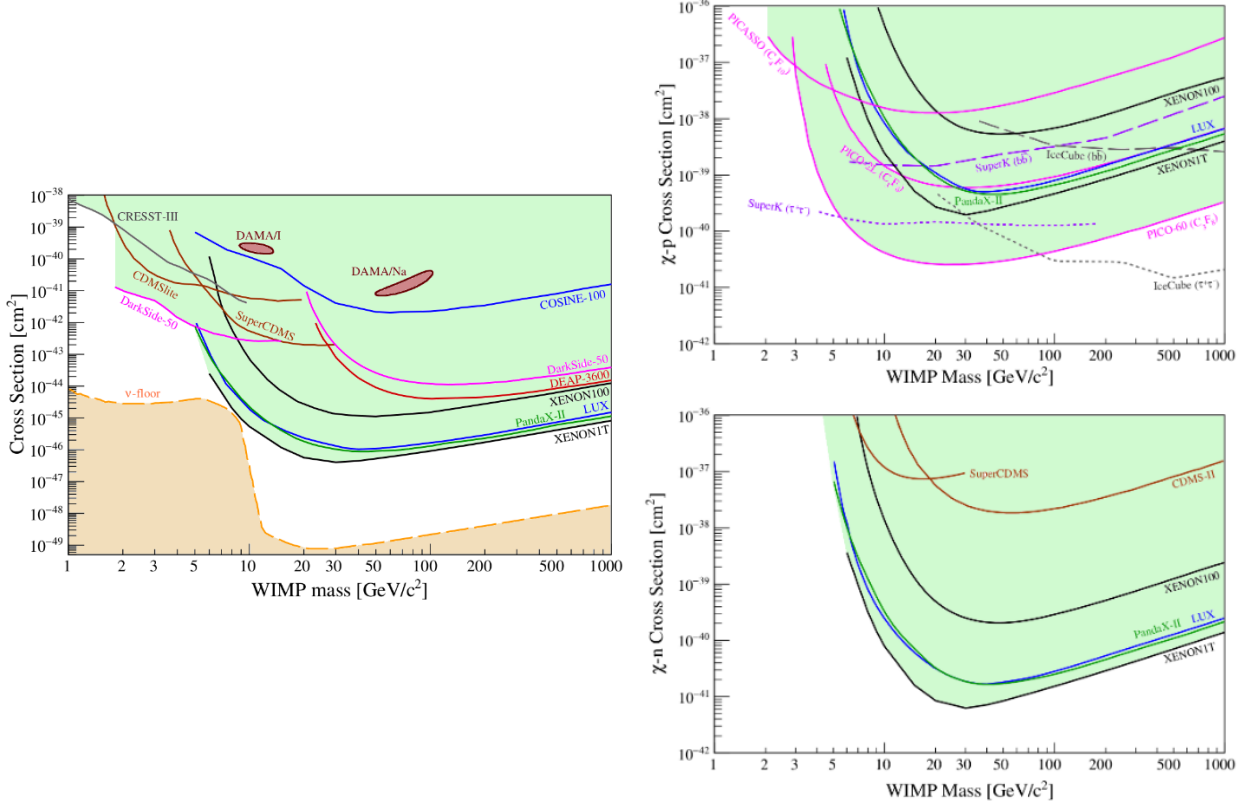


Figure 18: On the left, the landscape of dark matter direct detection constraints in the parameter space of dark matter mass and spin independent cross section with protons/neutrons (taken from [110]). The green region is currently ruled out. Not all current operating experiments are shown due to their large number (~ 30). Masses below 1 GeV are not shown, see extensive light dark matter results in Figure 19. The positive analysis of DAMA are shown in coloured shaded regions, [105]. The coherent neutrino scattering floor is shown in coloured orange, though it is importance to notice that this depends on the target material under consideration, see for example CRESST calculation, [111]. On the right, the constraints for spin dependent interactions with protons (up) and neutrons (down). The results from IceCube and Super-Kamiokande on dark matter capture in the sun are shown in dotted lines.

3.3.1 The CRESST Experiment

The Cryogenic Rare Event Search with Superconducting Thermometers (CRESST), is located in the Laboratori Nazionali del Gran Sasso. CRESST detectors consist on scintillating CaWO_4 crystals which operate as calorimeters at cryogenic temperatures. The scintillating property of the crystals allow to have an additional signal channel for particle identification.

In addition to the phonon/heat signal, the simultaneously emitted scintillation light is absorbed in a separate silicon-on-sapphire absorber and measured with Superconducting Phase Transition thermometers (TES). The scintillation light depends on the interacting particle, yielding event-by-event discrimination between the dominant background (β/γ -interactions) and the searched nuclear recoils. On the contrary, the phonon channel gives a precise measure of the energy deposition in the crystal, independently from the interacting particle. This, combined with the low energy threshold due to the presence of Oxygen in the crystal, makes CRESST very suited for low-mass dark matter detection. The CRESST-II and the CRESST-III programs, [17][18] provide one of the most stringent dark matter-nucleon scattering cross section bounds for light and sub-GeV dark matter masses, $m_\chi \leq 10$ GeV, for both spin independent (SI) and spin dependent (SD) interactions, see Fig 19.

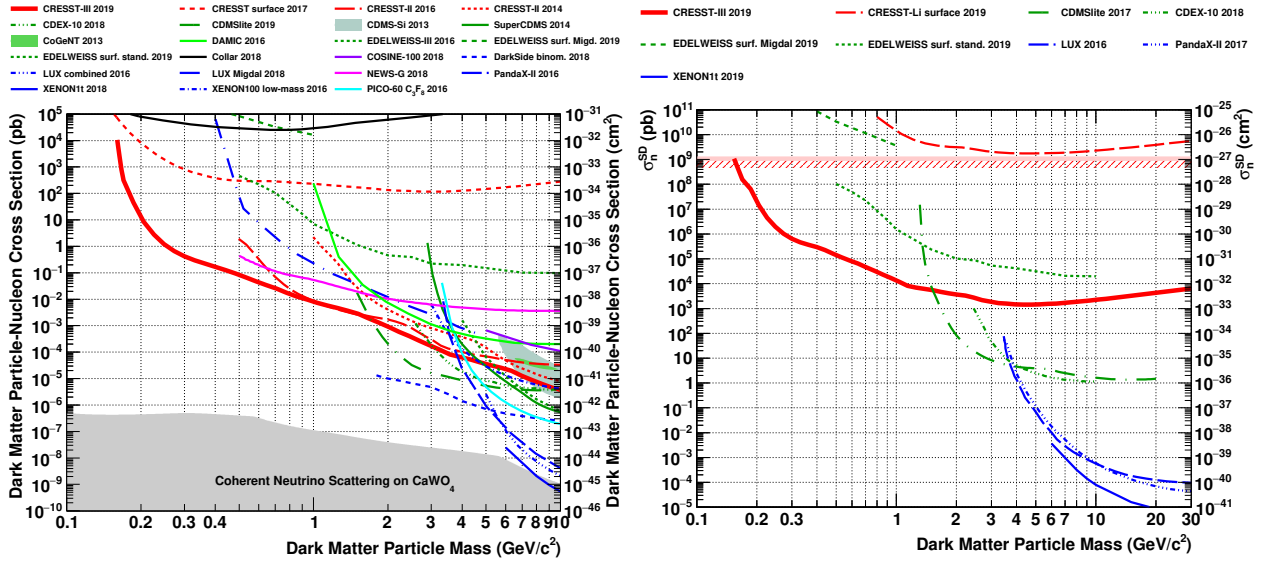


Figure 19: On the right, CRESST III results on spin-independent dark matter nucleus scattering depicted in the cross section versus dark matter particle mass. On the right, the spin-dependent constraint from dark matter interactions with the ^{17}O isotope. CRESST is the world leading experiment for spin independent DM scattering for masses below 1.6 GeV, and for spin dependent interactions below 0.6 GeV. Results are reported with 90% confidence level (CL).

4 Direct detection formalism

In this section, we describe the direct detection formalism necessary to compute the expected WIMP-nucleus recoil rate on a certain experiment. First, it is necessary to make a small discussion about the Earth frame of reference in which the WIMP scatterings are going to be measured, since the velocity distribution of dark matter particles will not be computed in the galactic center frame but on the Earth rest frame. We follow the usual parametrization of direct detection reviews, [112][113]. The velocity of the observer \vec{v}_{obs} with respect to the galactic rest frame can be decomposed into the velocity of the Sun with respect to the galactic rest frame as well as the velocity of the Earth with respect to the Sun

$$\vec{v}_{obs} = \vec{v}_{\odot} + \vec{v}_{\oplus} = \vec{v}_{LSR} + \vec{v}_{\odot,pec} + \vec{v}_{\oplus}, \quad (44)$$

where $v_{LSR} = (0, v_c, 0)$ is the motion of the local standard of rest (LSR) and $v_c \approx 220$ km/s is the local circular speed. Furthermore, $v_{\odot,pec} = (11.1, 12.24, 7.25)$ km/s is the Sun's peculiar motion. We notice that \vec{v}_{obs} actually present a phase dependence on the time of the year at which the recoil is measured, which is relevant for annual modulation searches, [114]. Nevertheless, we omit this precise description since this work does not consider modulation dark matter searches. The dark matter-induced scattering off the nucleus N_i in the detector is given by

$$\frac{dR_i}{dE_R} = \frac{\xi_i \rho_{loc}}{m_{DM} m_{N_i}} \int_{v \geq v_{min,i}(E_R)} d^3v \frac{f(\vec{v} + \vec{v}_{obs})}{v} \frac{d\sigma_{DM,i}}{dE_R}(v, E_R), \quad (45)$$

which has units of [counts/kg·day·keV]. The velocity of the dark matter particles in the laboratory frame is given by \vec{v} , and \vec{v}_{obs} is the velocity of the observer with respect to the galactic frame in equation 44. The astrophysical inputs are ρ_{loc} , the local density of dark matter particles discussed in section 2.1, and $f(\vec{v} + \vec{v}_{obs})$, the velocity distribution of dark matter particles in the galactic rest frame discussed in section 2.2. $m_{N,i}$ is the target nuclei i mass, and ξ_i is the mass fraction of the nuclei isotope under consideration. The total scattering rate is then given by

$$R = M \cdot T \cdot \int_0^\infty \sum_i \epsilon_i(E_R) \frac{dR_i}{dE_R} dE_R, \quad (46)$$

where M is the mass of the detector, T the exposure time and $\epsilon_i(E_R)$ are the recoil efficiencies of the nucleus N_i , determined experimentally.

We haven't determined the lower bound in the velocity integration $v_{min,i}(E_R)$ and the differential cross section of the dark matter-nucleon interaction $\frac{d\sigma_{DM,i}}{dE_R}(v, E_R)$. These are given by the kinematics of the scattering and the dark matter particle model under consideration, respectively, and will be discussed in the following sections 4.1 and 4.2

4.1 Kinematics of DM-nucleus scattering

The scattering of cold dark matter particles (bounded to the Milky Way) with the target nucleus happens in the non-relativistic regime, $v_\chi \sim 0.003c$. For terrestrial nuclei (this is not the case in the core of the sun, for example), the dark matter particles velocities are

significantly larger than thermal nuclei velocities $|\vec{v}_{i,\chi} - \vec{v}_N| \approx v_\chi$, so we can safely assume $p_{i,N} \approx 0$. Therefore we will derive here the non-relativistic equations in the laboratory frame. Figure 20 illustrates the scattering of a dark matter particle of mass m_χ with initial velocity $\vec{v}_{i,\chi}$ on a target nucleus of mass m_N in both elastic and inelastic cases.

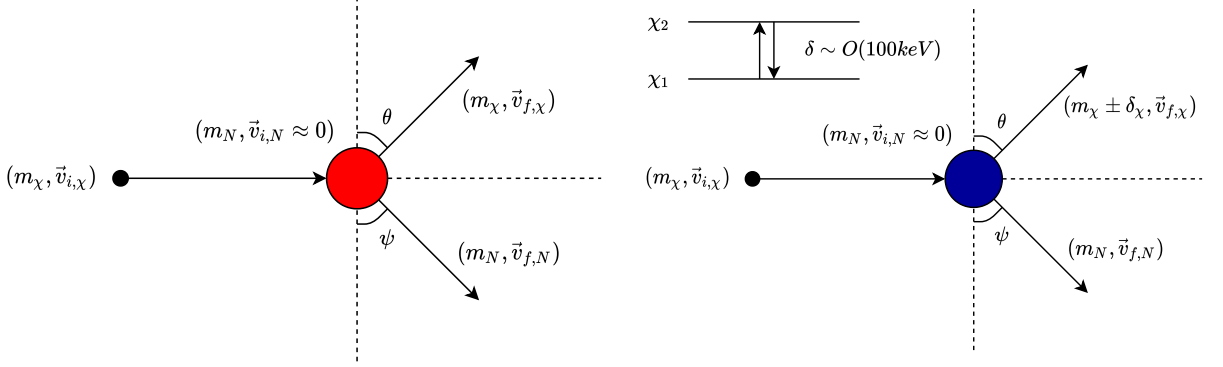


Figure 20: Coordinate representation of dark matter-nucleus scattering in the laboratory frame, in both elastic (left) and inelastic (right) cases. The mass splitting δ can be positive or negative depending on the reaction being endothermic or exothermic, [14].

From the conservation of energy and momentum

$$E_{i,\chi} + Q = E_{f,\chi} + E_{f,N} + E_{exc} = E_{total} + E_{exc}, \quad (E_{i,N} \approx 0), \quad (47)$$

$$p_{i,\chi} = p_{f,\chi} \cos\theta + p_{f,N} \cos\psi, \quad (48)$$

$$0 = p_{f,\chi} \sin\theta - p_{f,N} \sin\psi, \quad (49)$$

where $E = p^2/m$, $Q = m_{\chi,i} + m_{N,i} - m_{\chi,f} - m_{N,f}$ and E_{exc} is the excitation energy of the particles after the reaction. Rearranging equations 48 and 49 we obtain the following relation for momenta

$$p_{i,\chi}^2 + p_{f,\chi}^2 - 2p_{i,\chi}p_{f,\chi} \cos\theta = p_{f,N}^2, \quad (50)$$

and using equation 47 for the conservation of energy we get

$$p_{f,N}^2 = 2m_N \left(E_{total} - \frac{p_{f,\chi}^2}{2m_{f,\chi}} \right). \quad (51)$$

Now, substituting in 50 and solving the quadratic equation for $p_{f,\chi}$ one obtains the general solution

$$p_{f,\chi} = \frac{2p_{i,\chi} \cos\theta \pm \sqrt{4p_{i,\chi}^2 \cos^2\theta - 4 \frac{m_N}{\mu_{\chi f,N}} (p_{i,\chi}^2 - 2m_N E_{total})}}{2 \frac{m_N}{\mu_{\chi f,N}}}, \quad (52)$$

where $\mu_{\chi f,N} = \frac{m_N \cdot m_{f,\chi}}{m_N + m_{f,\chi}}$ is the usual reduced mass of the dark matter particle after scattering $m_{f,\chi}$ and the target nucleus m_N . From equation 52 we can derive the remaining kinematic variables. Direct detection experiment often measure the recoil energy E_R , i.e the kinetic energy transferred to the nucleus in the collision,

$$E_R = E_{f,N} - E_{i,N} = E_{total} - E_{f,\chi} = E_{i,\chi} - E_{f,\chi}, \quad (53)$$

where the kinetic energy of the incoming dark matter particle is $E_{i,\chi}$ is known and the final energy $E_{f,\chi} = \frac{p_{f,\chi}^2}{m_{f,\chi}}$ can be obtained from equation 52. The difference between the elastic and inelastic cases is only given by solving this equation for $v_{f,\chi}\cos\theta$ using $m_{i,\chi} = m_{f,\chi}$ for the elastic case and $m_{f,\chi} = m_{i,\chi} + \delta$, $\delta \neq 0$ for the inelastic one. The maximum energy that can be transferred to a nucleus depends on the dark matter particle initial velocity v_χ and mass splitting δ , yielding

$$E_R^{max} = \frac{\mu_{\chi,N}^2 m_N v_\chi^2 \pm \sqrt{\mu_{\chi,N}^4 m_N^2 v_\chi^2 - 2\mu_{\chi,N}^3 \delta m_N^2 v_\chi^2 - \mu_{\chi,N} m_N \delta}}{m_N^2}, \quad (54)$$

which, for the elastic scattering case, $\delta = 0$ reads,

$$E_R^{max} = \frac{2\mu_{\chi,N}^2 v_\chi^2}{m_N}. \quad (55)$$

This sets the minimum speed $v_{min}(E_R)$ for which a dark matter particle is capable to cause a nuclear recoil of energy E_R

$$v_{min}(E_R) = \frac{1}{\sqrt{2m_N E_R}} \left(\frac{E_R(m_\chi + m_N)}{m_\chi} + \delta \right) \quad (56)$$

For the elastic case, it is reduced to

$$v_{min}(E_R) = \sqrt{\frac{E_R m_N}{2\mu_{\chi,N}^2}} \quad (57)$$

This quantity will be of crucial importance for direct detection experiments, since every experiment register recoil events in a different energy range and this limits their capability to access certain dark matter masses and velocities. The purpose of this section was to derive $v_{min}(E_R)$, and conclude from equation 52 that the energy transfer is governed by the ratio of masses between the dark matter particle and the target nuclei, and the distribution of the scattering angle in the laboratory frame θ . We notice that in the literature the derivation here exposed is usually performed in the center of mass frame and they refer to the scattering angle θ in this frame, [113]. We can anticipate that the CRESST III experiment, due to its low energy threshold $E_{th} = 0.03$ keV, is able to probe a significantly larger region of the velocity spectrum for light and sub-GeV dark matter than other experiments. This also allows CRESST to test larger mass splittings δ if dark matter interacts inelastically. The inelastic scenario is discussed in section 7.

4.2 Effective field theories to describe DM-nucleus interactions

All evidence (except from the CMB and BBN) that we have of dark matter is based on its gravitational influence on visible matter at astronomical scales. In order to probe its particle nature and possible non-gravitational interactions, it is necessary to describe a model compatible with the Standard Model (SM). Ultraviolet complete extensions of the SM are well motivated and contain a dark matter particle, such as Supersymmetry, [12]. We will

study the viability of a concrete supersymmetric dark matter candidate, *sneutrinos*, in section 5.4.2. Another popular phenomenological alternative is to use the so-called simplified models, which introduce new degrees of freedom and symmetries to the SM lagrangian, not always being gauge invariant but that are meant to have an ultraviolet completion. We will study the viability of one of these extensions, the *Z-mediated* dark matter, in section 5.4.1.

Nevertheless, due to the large number of currently available simplified models on the community, a more general framework such as that of Effective Field Theories (EFT's) seems more appropriate to model the dark matter interactions with nuclei, since it can be used to describe the low energy physics of many proposed extensions of the SM. This is the framework in which most dark matter direct detection experiments attempt to make predictions and set upper limits on. We can study all the possible interactions of the dark matter field χ , e.g a massive Dirac fermion, in terms of Lorentz-invariant effective four-fermion operators (at leading order)

$$\mathcal{L}_{eff} \supset \sum_q \alpha_q (\bar{\chi} \Gamma_\chi \chi) (\bar{q} \Gamma_q q), \quad (58)$$

where the sum runs over all quarks q , [113][14] α_q are the effective DM-quark couplings and $\Gamma_{\chi,q} \in \{\mathbb{1}, \gamma^\mu, \gamma^5 \gamma^\mu, \sigma^{\mu\nu}, \sigma^{\mu\nu} \gamma^5\}$, are the effective operators. The effective coupling $\alpha_q(q^2, m_\phi)$ is proportional to the particle mediator of the dark matter interaction with quarks as $1/m_\phi^2$ for contact interactions ($q \ll m_\phi^2$) or to the center of mass frame energy of the scattering as $1/q^2$ for long-range interactions ($q^2 \gg m_\phi^2$). Now, it is necessary to map the quark operator to a nucleon operator and use this to obtain the matrix element for the DM-nucleus scattering. After taking the non-relativistic limit, the scattering amplitude \mathcal{M} enters the differential cross section (averaging/summing initial and final-state spins), [14]:

$$\frac{d\sigma}{dE_R} = \frac{2m_N}{\pi v_\chi^2} \langle |\mathcal{M}|^2 \rangle, \quad (59)$$

where v is the relative velocity between the DM particles and the nucleus. The matrix element \mathcal{M} encodes all the particle physics information of the model. The total (elastic) scattering cross section can be obtained by integrating over all recoil energies

$$\sigma_N = \int_0^{E_R^{max}} dE_R \frac{d\sigma_N}{dE_R}, \quad E_R^{max} = \frac{2\mu_{\chi,N}^2 v_\chi^2}{m_N}. \quad (60)$$

According to the cross section dependence on the nuclear spin, interactions are divided in two classes.

4.2.1 Spin-independent interactions

Spin-independent interactions can happen due to scalar-scalar and vector-vector couplings of dark matter particles χ to SM quarks q , with operators $\Gamma_{\chi,q} = \mathbb{1}$, $\Gamma_{\chi,q} = \gamma^\mu$, respectively

$$\mathcal{L}^{SI} = \sum_q [\alpha_q^S \bar{\chi} \chi \bar{q} q + \alpha_q^V \bar{\chi} \gamma^\mu \chi \bar{q} \gamma_\mu q], \quad (61)$$

where the first term represents the scalar interaction and the second term represents the vector interaction. Dark matter particles in the form of WIMPs interact coherently with

the target nucleus, since they have a de Broglie wavelength of the length scale of an atomic nucleus

$$\frac{\lambda}{2\pi} = \frac{\hbar}{p} = \frac{197 \text{ MeV} \cdot \text{fm}}{100 \times 10^3 \text{ MeV} \times 10^{-3} c} \approx 2fm, \quad (62)$$

assuming a WIMP mass of 100 GeV and a velocity of the order of the escape velocity of the Milky Way ~ 500 km/s. Hence, it was proposed by J.Engel, [115], that the Helm form factor can be used for spin-independent interactions, which is the Fourier transform of the nucleon density and usually parameterized in terms of the momentum transfer $q = \sqrt{2m_N E_R}$

$$F^2(q) = \left(\frac{3j_1(qr_0)}{qr_0} \right)^2 \exp(-q^2 s^2), \quad (63)$$

where j_1 is the spherical Bessel function for $n=1$, $s \approx 1$ is the thickness parameter of the nucleus surface, and $r_0 = \sqrt{r_{nuc}^2 - 5s^2}$, with the nuclear radius $r_{nuc} = 1.2A^{1/3}$ fm. Its parameters are obtained from data of electron scattering experiments, so one assumption is that the WIMP scatters are distributed as the charge in the nucleus, [93]. At small momentum transfer, the DM particles do not probe the size of the nucleus and the cross section is unaffected. However, as the momentum transfer increases, the interactions become sensitive to the size of the nucleus and the cross section is weakened. This energy dependence is parameterized in the form factors $F^2(E_R)$.

The matrix element \mathcal{M}_{scalar} for the scattering between a dark matter particle χ and a nucleus N via a scalar mediator in the non-relativistic limit reads, see [14] for a complete derivation,

$$\mathcal{M} = [f^p Z + f^n (A - Z)] F^2(E_R), \quad (64)$$

and, according to equation 59, the differential cross section is

$$\frac{d\sigma_{scalar}}{dE_R} = \frac{2km_N}{\pi v_\chi^2} [Z f^p + (A - Z) f^n]^2 F^2(E_R), \quad (65)$$

where k is a constant that arises from summing and averaging initial state respectively final state spins ($k = 1$ if the WIMP is a Dirac particle and 4 if it is Majorana), [55]. A and Z denote the mass number and the atomic number of the nucleus element. f^p and f^n parameterize the coupling strength of dark matter to protons respectively neutrons. For protons, they are given by

$$f^p = \sum_{q=u,d,s} \frac{m_p \cdot \alpha_q^S}{m_q} f_{Tq}^p + \frac{2}{27} f_{TG}^p \sum_{q=c,b,t} \frac{m_p \cdot \alpha_q^S}{m_q}, \quad (66)$$

where f_{Tq}^p represent the contributions of the light quarks (u, d, s) to the proton mass, and are defined as $m_p f_{Tq}^p = \langle p | m_q q \bar{q} | p \rangle$. f_{TG}^p refers to the WIMP interaction with the gluon scalar density in the nucleon, being $f_{TG}^p = 1 - \sum_{q=u,d,s} f_{Tq}^p$. Their values are determined experimentally. Integrating out according to equation 60, the contribution from the scalar couplings leads to the following expression for the WIMP-nucleus cross section at zero momentum transfer

$$\sigma_{0,scalar} = \frac{k\mu_{\chi,N}^2}{\pi} [Z f^p + (A - Z) f^n]^2. \quad (67)$$

The vector coupling vanishes for Majorana particles but survives for Dirac fermions, giving rise to the following WIMP-nucleus cross section at zero momentum transfer

$$\sigma_{0,vector} = \frac{\mu_{\chi,N}^2 B_N^2}{64\pi} \delta(k-1), \quad (68)$$

with

$$B_N = \alpha_u^V (A+Z) + \alpha_d^V (2A-Z), \quad (69)$$

where α_u^V and α_d^V are the coupling constants for up-quarks respectively down-quarks as only valence quarks contribute to this term, [113]. The total WIMP-nucleus cross section then reads

$$\sigma_0^{SI} = \frac{\mu_{\chi,N}^2}{\pi} \left[(Zf^p + (A-Z)f^n)^2 k + \frac{B_N^2}{64} \delta(k-1) \right]. \quad (70)$$

Assuming equal coupling to protons and neutrons $f^p = f^n$ as well as Majorana dark matter, the expression reduces to

$$\sigma_0^{SI} = \frac{\mu_{\chi,N}^2}{\pi} A^2 (f^p)^2. \quad (71)$$

Direct detection experiments use different target nuclei so it is convenient to write the differential scattering rates in terms of the WIMP-proton cross section. In the case of $f^p = f^n$, the WIMP-proton and the WIMP-nucleus at zero momentum transfer cross sections are related as, [14][60],

$$\sigma_0^{SI} = \frac{\mu_{\chi,N}^2}{\mu_{p,n}^2} A^2 \sigma_{p,n}^{SI}, \quad (72)$$

where $\mu_{\chi,p,n}$ and $\mu_{\chi,N}$ are the dark matter-nucleon respectively the dark matter-nucleus reduced mass and σ_0^{SI} is defined as,

$$\frac{d\sigma_{SI}}{dE_R} = \frac{m_N \sigma_0^{SI} F^2(E_R)}{2\mu_{\chi,N}^2 v^2}, \quad (73)$$

where σ_0^{SI} is the total, point-like WIMP-nucleon cross section at zero momentum transfer. Taking this into account, the differential scattering cross section in terms of the interactions with nucleons is given by

$$\boxed{\frac{d\sigma_{SI}}{dE_R} = \frac{m_N}{2\mu_{\chi,p,n}^2} A^2 \sigma_{p,n}^{SI} F^2(E_R)} \quad (74)$$

where all the information on the WIMP model is encoded in $\sigma_{p,n}^{SI}$. This formula is only valid for elastic scattering, since the integration 60 would change in the inelastic case, being the upper value of the integration of the recoil energy given by 54. We notice that the cross section decreases with the inverse square of the speed of the dark matter particles, so we would naively expect less high energetic recoils than low energetic ones at experiments. This is interesting since the experimental backgrounds for high energetic events are usually better suppressed than at low recoiling energies, for example at CRESST, [17][18]. We further notice that the differential cross section scales with the squared number of nucleons A^2 for $f^p = f^n$, so that heavy nuclei is favoured w.r.t light nuclei. For this reason heavy target elements such as ^{184}W at CRESST or ^{131}Xe at XENON1T are used. The use of complementary targets is essential to not miss a dark matter signal due to a destructive interference $f^p/f^n \approx -(A-Z)/Z$, as it is discussed in [55].

4.2.2 Spin-dependent interactions

Spin-dependent interactions arise from the axial-vector coupling between dark matter and quarks, with operator $\Gamma_{\chi,q} = \gamma^\mu \gamma^5$. For a Dirac or Majorana fermion dark matter, the lagrangian of the spin-dependent interactions reads

$$\mathcal{L}^{SD} = \sum_q \alpha_q^A (\bar{\chi} \gamma_\mu \gamma^5 \bar{\chi}) (\bar{q} \gamma^\mu \gamma^5 q), \quad (75)$$

while for a bosonic (spin 1) WIMP, the interaction term reads,

$$\mathcal{L} = \sum_q \alpha_q^A \epsilon^{\mu\nu\rho\sigma} (B_\rho \overleftrightarrow{\partial}_\mu B_\nu) (\bar{q} \gamma^\mu \gamma^5 q), \quad (76)$$

where B_ρ are the spin-1 dark matter vector fields. According to [113], the nucleus N matrix element for both cases is

$$\langle N | \bar{q} \gamma^\mu \gamma^5 q | N \rangle = 2\lambda_q^N \langle N | J_N^\mu | N \rangle, \quad (77)$$

where J_N^μ is the spin operator of the nucleus. The coefficients λ_q^N relate the quark spin matrix elements to the angular momentum of the nucleons and are parametrized as

$$\lambda_q^N \simeq \frac{\Delta_q^{(p)} \langle S_p \rangle + \Delta_q^{(n)} \langle S_n \rangle}{J}, \quad (78)$$

where J is the total spin of the nucleus. $\Delta_q^{(p,n)}$ are obtained from the axial-vector current in a nucleon and describe the amount of spin carried by a quark of flavor q inside the proton and neutron. Their values were calculated in [116]. $\langle S_{p,n} \rangle$ are the expectation values of the spin content in the proton group respectively the neutron group in the nucleus. Their values were calculated in [117]. In order to achieve an expression for spin-dependent differential cross section, we need to know the dark matter proton respectively neutron coupling constants. These are determined by adding up the contributions from all quarks

$$a_{p,n} = \sum_{q=u,d,s} \frac{\alpha_q^A}{\sqrt{2}G_F} \Delta_q^{p,n}, \quad (79)$$

where G_F is the Fermi constant. The form factor squared can be expressed as

$$F^2(E_R) = \frac{S_A(E_R)}{S_A(0)}, \quad (80)$$

where a strong isospin decomposition into isoscalar $a_0 = a_p + a_n$, and isovector, $a_1 = a_p - a_n$ is assumed in the parameterization, yielding

$$S(E_R) = a_0^2 S_{00}(E_R) + a_0 a_1 S_{01}(E_R) + a_1^2 S_{11}(E_R), \quad (81)$$

whose parameters are determined experimentally, [113]. The resulting differential cross section for a fermionic (spin 1/2) WIMP is given by

$$\boxed{\frac{d\sigma_{SD}}{dE_R} = \frac{4km_N G_F^2 (J+1)}{\pi v^2 J} [a_p \langle S_p \rangle + a_n \langle S_n \rangle] \frac{S_A(E_R)}{S_A(0)}} \quad (82)$$

The main difference from the spin-independent dark matter-nucleus interactions is that the spin-dependent differential scattering cross section does not increase with the number of nucleons, but rather depend on the nucleus spin J . Indeed spin-dependent interactions can be tested only on isotopes with $J \neq 0$. Furthermore, the differential cross section is proportional to the expectation values of the spin content in the proton group respectively the neutron group in the nucleus $\langle S_{p,n} \rangle$, which differ for different isotopes and do not favour heavy ones, [117]. Thus, the ideal targets to test spin-dependent interactions are constituted elements with $J \neq 0$, $\langle S_{p,n} \rangle = 1/2$ and low masses. Some examples include Fluorine at PICO, ^{17}O at CRESST, [18], or recently ^7Li , [118].

5 Parametrization of dark matter astrophysical uncertainties

We have discussed in section 2.2 that the Maxwell-Boltzmann velocity distribution used by experiments presents deviations with respect to the results obtained from simulations and tracers observations. Therefore, we need to account for this astrophysical uncertainty in the results of dark matter searches, in particular direct detection experiments and neutrino telescopes, sensitive to the velocity distribution of dark matter particles. In this section, we review the methodology developed in [120][121][55] to optimize the velocity distribution of dark matter particles, in order to perform combined halo-independent analyses of different dark matter experiments. We furthermore propose an alternative new method to the technique of [121] to measure deviations with respect to the Maxwell-Boltzmann velocity distribution, 5.1. Our method will be based in information divergences, [122], and therefore we will discuss them in advance, 5.2. Later, we will apply the general methodology to the CRESST III experiment, [18], and discuss the obtained results, 5.3. In addition, we apply the methodology to the XENON1T experiment, [107], and contrast the results with the cross sections predicted by two specific dark matter models, analyzing the importance of the astrophysical uncertainties when interpreting the viability of such models, 5.4. Finally, we compute halo-independent upper limits from the combination of CRESST II and Super-Kamiokande, 5.5.

5.1 Methodology: Optimization of the dark matter velocity distribution

We follow the notation of [55]. Our purpose is to optimize the outcome $N^{(A)}$ of a experiment A under the constrains from further $p+q$ experiments. We can have $\alpha = 1, \dots, p$ upper limits $N^{(B_\alpha)} \leq N_{max}^{(B_\alpha)}$ and $\alpha = p+1, \dots, p+q$ lower limits $N^{(B_\alpha)} \geq N_{min}^{(B_\alpha)}$ from experiments B_α . In this work, the outcomes $N^{(A)}$, $N^{(B_\alpha)}$ will be the recoil rate of a direct detection experiment, in equation 46, and the capture rate of dark matter particles in the Sun, given in equation 37. Since we want to optimize the velocity distribution of dark matter particles, we need to rewrite it in terms of δ -functions

$$f(\vec{v}) = \int_{v_0 \leq v_{esc}} dv_0^3 f(\vec{v}_0) \delta(\vec{v} - \vec{v}_0), \quad (83)$$

where $v_0 = |\vec{v}_0|$. In the discrete limit, this decomposition as a sum of dirac functions is justified by the Padé approximation, [123], and we interpret it as a superposition of streams with a fixed velocity \vec{v}_0 and weight $f(\vec{v}_0)$. In the limit of infinite streams we would recover a continuous probability distribution, [124]. For each stream \vec{v}_0 , we would obtain an experimental outcome $N_{\vec{v}_0}$ when considering the dark matter velocity distribution as a single stream $f(\vec{v}) = \delta(\vec{v} - \vec{v}_0)$, so that the total experimental outcome would be given by

$$N = \int_{v_0 \leq v_{esc}} dv_0^3 f(\vec{v}_0) N_{\vec{v}_0}. \quad (84)$$

For a single stream \vec{v}_0 , the experimental outcomes that we will consider in this thesis, that is, the recoil rate in a direct detection experiment and the capture rate of dark matter particles

in the sun, given by equations 46 and 37, are reduced to

$$R_{\vec{v}_0} = \sum_i \frac{M T \xi_i \rho_{loc}}{m_{N_i}, m_{DM}} \int_0^{\frac{2\mu_{N_i}^2 v_0^2}{m_{N_i}}} dE_R \epsilon_i(E_R) v_0 \frac{d\sigma_{DM,i}}{dE_R}(m_{DM}, E_R), \quad (85)$$

$$C_{\vec{v}_0} = \sum_i \int_0^{R_\odot} dr 4\pi r^2 \eta_i(r) \frac{\rho_{loc}}{m_\chi} \frac{(v_0^2 + v_{sun,esc}(r)^2)}{v_0} \theta(v_{max}(r) - v_0) \int_{m_\chi v_0^2/2}^{\frac{2\mu_{N_i}^2 (v_0^2 + v_{sun,esc}(r)^2)}{m_{N_i}}} dE_R \frac{d\sigma_{\chi,i}}{dE_R}(v_0, E_R), \quad (86)$$

where the kinematical constraint given by 57 in 85, that is, that the dark matter particle velocities v_0 need to be larger than $v_{min}(E_R)$ in order to produce a recoil, appears as a heaviside function $\theta(v_0 - v_{min}(E_R))$ that sets an upper limit in the recoil integration. We notice that in the case of inelastic scattering this upper bound would be set by equation 54. Analogously, the velocity integral for the capture rate is bounded from above, from the kinematical constraint of equation 36, leading to the heaviside factor $\theta(v_{max}(r) - v_0)$. Now, we can formulate the general problem of finding an upper limit on the outcome N^A subject to constraints from further experiments N^{B_α} as an optimization problem with the velocity distribution f as the primal variable

$$\text{Optimize: } \mathcal{N}^{(A)}[f] = \int d^3v f(\vec{v}_0) N_{\vec{v}_0}^A \quad (87)$$

subject to:

$$\int d^3v_0 f(\vec{v}_0) = 1$$

$$\int d^3v_0 f(\vec{v}_0) N_{\vec{v}_0}^{(B_\alpha)} \leq N_{max}^{(B_\alpha)}, \quad \alpha = 1, \dots, p.$$

$$\int d^3v_0 f(\vec{v}_0) N_{\vec{v}_0}^{(B_\alpha)} \geq N_{min}^{(B_\alpha)}, \quad \alpha = p+1, \dots, p+q.$$

$$f(\vec{v}_0) \geq 0$$

where the objective function $\mathcal{N}^{(A)}$ is a functional of the velocity distribution. From the KKT necessary conditions, see Appendix A.2, this problem cannot be solved analytically, [55]. However, as we have already discussed, expression 83 can be discretized into n streams with velocities \vec{v}_i for $i = 1, \dots, n$, which yields

$$f(\vec{v}) = \sum_{i=1}^n c_{\vec{v}_i} \delta(\vec{v} - \vec{v}_i), \quad (88)$$

where the continuous probability densities $f(v_0)$ are now given discretely by $c_{\vec{v}_i}$. More technical discussions regarding this aspect are covered in [55][125][126]. With this, the optimization problem 87 is recasted as

$$\textbf{Optimize: } N^{(A)}(c_{\vec{v}_1}, \dots, c_{\vec{v}_n}) = \sum_{i=1}^n c_{\vec{v}_i} N_{\vec{v}_0}^A \quad (89)$$

subject to:

$$\sum_{i=1}^n c_{\vec{v}_i} = 1$$

$$\sum_{i=1}^n c_{\vec{v}_i} N_{\vec{v}_i}^{(B_\alpha)} \leq N_{max}^{(B_\alpha)}, \quad \alpha = 1, \dots, p.$$

$$\sum_{i=1}^n c_{\vec{v}_i} N_{\vec{v}_i}^{(B_\alpha)} \geq N_{min}^{(B_\alpha)}, \quad \alpha = p + 1, \dots, p + q.$$

$$c_{\vec{v}_i} \geq 0$$

where the objective function $N^{(A)}(c_{\vec{v}_1}, \dots, c_{\vec{v}_n})$ is now a function of the weights $c_{\vec{v}_i}$. The problem is convex, since the functions 85 and 86 are convex if defined in a convex velocity set. We take the velocity space to be the ball in the usual euclidean metric M , $B_{v_{esc}}(0) = \{\vec{v}_0 \in M, d(\vec{v}_0, 0) < v_{esc}\}$ of radius the escape velocity of the Milky Way v_{esc} centered at 0, which is convex, [127]. A discrete subset $C \subset B_{v_{esc}}(0)$ made of n uniformly discretized velocities \vec{v}_i would also be convex. Therefore the problem 89 can be solved using convex optimization techniques, see Appendix A.1. We notice that the objective function and the problem inequalities are linear functions of the primal variables $c_{\vec{v}_i}$. Hence, the problem can be solved using linear programming, see Appendix A.3, once transformed into its standard form. A nice attempt to find an analytical solution to this problems using lagrange multipliers can be found in [55]. We will use in the following the publicly available code **CVXPY**, [119], to solve problems with this structure numerically.

The optimization problem 89 presents many applications discussed in [120]. In this thesis, we will use it to derive upper limits on the dark matter cross section from null results of CRESST II and Super-Kamiokande, independently of the dark matter halo velocity distribution. This approach is performed in section 5.5. There, for a fixed cross section and dark matter mass, we calculate the minimal capture rate in the sun from varying the dark matter velocity distribution, subject to the upper limit from CRESST II, that satisfies the constraint on dark matter annihilation rates in the Sun from Super-Kamiokande.

Nevertheless, in the case of combining direct detection experiments only, we notice that the optimized approach only works for the maximization case, since in the case of minimization, (which is indeed the most relevant for us, since we want to be conservative due to our ignorance of the dark matter velocity distribution in the Milky Way), the halo-independent upper limits can't be calculated, because all dark matter weights $c_{\vec{v}_i}$ above the velocity threshold of the experiment $v_{min}(E_{thr})$ are set to zero by the algorithm, and therefore the experiment is not sensitive to a dark matter signal at all. In [121], this problem is addressed by including an additional constraint in the optimization problem 89, that sets a maximal

deviation that the optimized velocity distribution $f(\vec{v})$ can have with respect to the Maxwell-Boltzmann $f_{MB}(\vec{v})$, equation 23. This is achieved in [121] by parameterizing the deviations using point-to-point *relative differences* in velocity space, i.e

$$\left| \frac{f(\vec{v}) - f_{MB}(\vec{v})}{f_{MB}(\vec{v})} \right|, \leq \Delta \quad (90)$$

where the phenomenological parameter Δ allows to quantify the deviation of the velocity distribution from the SHM form. This constraint can be included in the optimization problem 89, so that, for a given Δ , the velocity distribution that maximizes/minimizes the signal rate in a dark matter experiment can be calculated. This allows to calculate the most conservative/aggressive limits on the $\sigma - m_\chi$ parameter space of a certain experiment A , for the subset of admissible velocity distributions fulfilling the constraint 90. The problem now reads

$$\textbf{Optimize: } N^{(A)}(c_{\vec{v}_1}, \dots, c_{\vec{v}_n}) = \sum_{i=1}^n c_{\vec{v}_i} N_{\vec{v}_0}^{(A)} \quad (91)$$

subject to:

$$\sum_{i=1}^n c_{\vec{v}_i} = 1$$

$$c_{\vec{v}_i} \leq (\Delta + 1) f_{MB}(\vec{v}_i)$$

$$c_{\vec{v}_i} \geq \max \{0, (1 - \Delta)\} f_{MB}(\vec{v}_i)$$

$$c_{\vec{v}_i} \geq 0$$

where the constraints from further experiments upper limits present in problem 89 could also be included. Nevertheless, they do not play an important role when combining direct detection experiments in the minimization case since velocity distributions more conservative than the Maxwell-Boltzmann will always respect the current experimental limits, and therefore the constraints on the deviation w.r.t the Maxwell-Boltzmann are the ones which set the optimized velocity distributions.

This method is very powerful since it allows to interpolate between the most aggressive and most conservative upper limits of a dark matter experiment when varying the dark matter velocity distribution, having the Maxwell-Boltzmann as the reference distribution. However, it present some caveats. It consists in a point-to-point comparison, so that every point in velocity space is restricted in exactly the same amount to deviate w.r.t the Maxwell Boltzmann, being therefore the shape of the optimized velocity distributions very similar to the Maxwell-Boltzmann. Dark matter substructure such as streams, debris flows or subhalos peaking at certain regions of the velocity distribution would never satisfy the constraint of equation 90 and therefore those velocity distributions would be discarded by our algorithm. Furthermore, the optimized velocity distributions obtained using *relative differences* to parameterize the deviations from the SHM strongly penalise the high velocity tail of the distribution, presenting a sharp cut off at the peak velocity, which is compensated reweighting the

low velocity tail. This is clearly visible in Figure 23 and will be thoroughly discussed in the following section 5.2. We need to account for deviations of the Maxwell-Boltzmann in a proper way, such that the feasible set of distribution functions respecting a certain deviation is as most generic as possible, so that our optimized limits are truly independent from the dark matter halo. In the following section, we propose an alternative method to parametrize deviations with respect to the Maxwell-Boltzmann that will allow for a more statistically solid halo-independent analysis of direct dark matter searches.

5.2 Parametrizing deviations from the SHM: Information theory divergences

We want to find an appropriate distance measure to parameterize the deviation of the true velocity distribution from the SHM. The importance of choosing an appropriate distance to measure how far from the truth is a certain set of models lies in the fact that each distance measure deals differently with the structure of the models of interest and provides a different information about the phenomena under study. This will be translated in our case to understand which features are accounted between velocity distributions associated to a certain distance measure. In our case, as we will work with a truncated Maxwell-Boltzmann velocity distribution as the reference model, the most relevant features are deviations in the tails of the distributions and shifted values of the most probable speed. Before presenting our methodology in a computable analogous form to problem 115, it is necessary to introduce some concepts that will be relevant to understand our approach.

In measure theory, a measurable space or Borel space is given by the tuple (\mathcal{X}, A) , where \mathcal{X} is a set and A is a σ -algebra on \mathcal{X} . A probability space is given by the triplet (\mathcal{X}, A, P) consisting on a Borel space where \mathcal{X} is the sample space of all possible outcomes, A is the collection of all events under consideration, and a probability measure $P : \mathcal{F} \rightarrow [0, 1]$ assigning probabilities to events. In this probability space is where the distance measures discussed in this manuscript are defined. In information theory, *divergence* refers to a weaker definition of "distance" between two probability distributions (or more generally, probability measures) on a given set (Borel space). In particular, the divergence need not to be symmetrical, i.e generally $D(P, Q) \neq D(Q, P)$. Of particular importance are the *f-divergences* [128], a class of divergences defined as

$$D_f(P, Q) = \int_{\mathcal{X}} f \left(\frac{dP}{dQ} \right) dQ, \quad (92)$$

where P and Q are two probability measures defined on (\mathcal{X}, A) , such that P is absolutely continuous with respect to Q , so that the Radon-Nikodym derivative is given by dP/dQ , and f is a convex function such that $f(1) = 0$. If μ is any measure on the set (a reference distribution) \mathcal{X} such that the probability densities $p = \frac{dP}{d\mu}$ and $q = \frac{dQ}{d\mu}$ exist, the *f-divergence* can be expressed as

$$D_f(P, Q) = \int_{\mathcal{X}} f \left(\frac{p(x)}{q(x)} \right) q(x) d\mu(x). \quad (93)$$

For a continuous random variable, taking the usual *Lebesgue measure* dx , it can be written

$$D_f(P, Q) = \int_{\mathcal{X}} f\left(\frac{p(x)}{q(x)}\right) q(x) dx. \quad (94)$$

In this thesis, we will work with three different *f-divergences* to parameterize the deviations with respect to the Maxwell-Boltzmann velocity distribution. These will be related analytically between each other *a priori*, and later we will compare their performance in our specific physics problem and interpret the different results obtained. The information divergences that we will use are the *total variation distance*, the χ^2 -*divergence* and the *KL-divergence*.

The *total variation distance* between two probability measures P and Q defined on a Borel space (\mathcal{X}, A) is obtained by taking $f = \frac{1}{2} |t - 1|$, and reads

$$\delta(P, Q) = \sup_{x \in \mathcal{X}} |p(x) - q(x)|. \quad (95)$$

Informationally, this is the largest possible difference between the probabilities that the two probability distributions can assign to the same event.

The *Pearson χ^2 divergence* is obtained using $f(t) = t^2 - 1$ and is then defined as

$$D_{\chi^2}(P, Q) = \int_{x \in \mathcal{X}} dx \frac{(p(x) - q(x))^2}{p(x)}, \quad (96)$$

and the reverse result $D(Q, P)$ is obtained by taking $f(t) = \frac{1}{t} - 1$ and is named the *Neyman χ^2 divergence*.

The *KL divergence* is obtained by taking $f(t) = t \log t$ and is then defined as

$$D_{KL}(P, Q) = \int_{x \in \mathcal{X}} dx p(x) \log \left(\frac{p(x)}{q(x)} \right). \quad (97)$$

We are interested in defining distance measures between velocity distributions, i.e probability distributions of a continuous random variable, although we will work in the end with discrete probability distributions, due to the discretization of the optimized velocity distributions expressed in previous section 5.1, equation 83. If P and Q are discrete probability distributions of a random variable x , the *total variation distance* reads,

$$\boxed{\delta(P, Q) = \sup_{x \in \mathcal{X}} |P(x) - Q(x)|} \quad (98)$$

The *Pearson χ^2 -divergence* reads,

$$\boxed{D_{\chi^2}(P, Q) = \sum_{x \in \mathcal{X}} \frac{(P(x) - Q(x))^2}{P(x)}} \quad (99)$$

and the *KL-divergence*,

$$\boxed{D_{KL}(P, Q) = \sum_{x \in \mathcal{X}} P(x) \log \left(\frac{P(x)}{Q(x)} \right)} \quad (100)$$

We will focus our study in the *KL-divergence*. The reason is that the *KL-divergence* is, by its definition, a very well motivated distance measure to compute deviations with respect to the Maxwell-Boltzmann distribution. In order to justify this statement properly, we need to look in detail at the KL-divergence properties, [129]:

- It is not a metric, $D_{KL}(P, Q) \neq D_{KL}(Q, P)$.
- It is non-negative, $D_{KL}(P, Q) \geq 0$.
- It is convex in the pair of discrete probability distributions P and Q , i.e given two pairs of probability distributions $(P_1, Q_1), (P_2, Q_2)$,

$$D_{KL}(\lambda P_1 + (1 - \lambda)P_2, \lambda Q_1 + (1 - \lambda)Q_2) \leq \lambda D_{KL}(P_1, Q_1) + (1 - \lambda)D_{KL}(P_2, Q_2)$$

for $0 \leq \lambda \leq 1$

- For discrete probability distributions, the *KL* divergence can be expressed as

$$D_{KL}(P, Q) = - \sum_{x \in \mathcal{X}} P(x) \log(Q(x)) + \sum_{x \in \mathcal{X}} P(x) \log(P(x)) = H(P, Q) - H(P) \quad (101)$$

where $H(P, Q)$ is the cross-entropy of P and Q and $H(P)$ is the entropy of P .

The *KL-divergence* is interpreted as the *relative entropy* of P with respect to Q . From a Bayesian inference point of view, $D_{KL}(P, Q)$ is a measure of the *information gained* when one revises one's beliefs from the prior probability distribution Q to the posterior probability distribution P . This is the interpretation that we will use in section 6.

Since the Maxwell Boltzmann velocity distribution, which is the reference distribution that we want to compare with the true dark matter velocity distribution, can be obtained as the distribution that maximizes the Shannon entropy of a system under the constraint of conservation of energy, as we have discussed previously in section 2.2.4, the *KL-divergence* is the most suitable distance to quantify such difference, representing the *KL-divergence* the relative Shannon entropy between two distributions. Nevertheless, though the *KL-divergence* is well motivated theoretically as a distance measure for our specific physics problem, the usage of further divergences provides additional information about the system under study that could escape the *KL-divergence* constraint. For this reason, to establish bounds on the *KL-divergence* in terms of the *total variation distance* and the χ^2 -*divergence* helps to understand the scaling between them and to constrain the true set of feasible dark matter velocity distributions that wouldn't give a dark matter signal in a certain experiment and deviate a certain amount from the Maxwell Boltzmann.

Theorem 1 *The KL-divergence $D_{KL}(P, Q)$ and the total variation distance $\delta(P, Q)$ divergence are related via Pinsker's inequality*

$$2\delta(P, Q)^2 \leq D_{KL}(P, Q).$$

This theorem establish a lower bound on the *KL-divergence* in terms of the *total variation distance*. The *KL-divergence* and the χ^2 -*divergence* are related via

Theorem 2 *The KL-divergence $D_{KL}(P, Q)$ and the χ^2 divergence $D_{\chi^2}(P, Q)$ satisfy the next inequalities*

$$D_{KL}(P, Q) \leq \log(D_{\chi^2}(P, Q) + 1) \leq D_{\chi^2}(P, Q)$$

In particular, $D_{KL}(P, Q) = D_{\chi^2}(P, Q) \Leftrightarrow P = Q$.

A complete proof of theorems 1 and 2 can be found in Appendix B.2. This result provides an upper bound for the *KL-divergence* in terms of the χ^2 -*divergence*, when computed both from the distribution P to Q (Pearson divergence). Unfortunately, in the specific optimization problems that we will work with, only the χ^2 from Q to P (Neyman divergence) can be used while keeping the convexity of the problem. Since information divergences are not symmetric, this bound is no longer viable. We have attempted to perform a mathematical proof of this bound but we noticed that it is necessary to determine how are $\int_{\mathcal{X}} dx \frac{q(x)^2}{p(x)}$ and $\int_{\mathcal{X}} dx \frac{p(x)^2}{q(x)}$ related, which is not trivial for normalized distributions and thus depends on p and q . Nevertheless, due to Pinsker's inequality 1, we have to a lower bound for the *KL-divergence* in terms of the total variation distance that provides us with a very useful additional information.

After all this technical discussion about information divergences, we go back to our physics problem. We design the following optimization problem based in information divergences

$$\textbf{Optimize: } \mathcal{N}^{(A)}[f] = \int d^3v f(\vec{v}_0) N_{\vec{v}_0}^{(A)} \quad (102)$$

subject to:

$$\int d^3v_0 f(\vec{v}_0) = 1$$

$$D_{f_1}(f, f_{MB}) \leq K_1$$

$$D_{f_2}(f_{MB}, f) \leq K_2$$

$$f(\vec{v}_0) \geq 0$$

where the constraint 90 in the problem 115 has been substituted by the constraint of the *f-divergence* from the true distribution $f(\vec{v})$ to the Maxwell-Boltzmann distribution $f_{MB}(\vec{v})$ to be smaller than a certain value K_1 , or, alternatively, the *f-divergence* from the Maxwell-Boltzmann distribution to the true distribution to be smaller than a certain value K_2 . This problem can be formulated on general grounds, as we have done, but one needs to write it in its discretized form for each *f-divergence* under consideration and check the convexity of the problem and its solvability. The three information divergences that we have selected (*KL-divergence*, *total variation distance* and *Neyman divergence χ^2*) satisfy the convexity requirements of problem 102 and can be recasted as Second Order Cone problems (SOCP's), see Appendix A.4 solvable by **CVXPY**, concretely with its internal solver **ECOS**, [130]. In the case of the *total variation distance*, equation 98, the constraint would be simply linear

on the weights $c_{\vec{v}_i}$, so convexity is guaranteed. In the case of the *Neyman divergence* χ^2 , equation 99, the constraint is quadratic on the weights and can be solved using *quadratic programming*, [131], a class of problems that can be transformed into Second Order Cone Problems (SOCP's) as described in [55]. The KL-divergence can also be converted into a convex constraint by transforming it into a form in which belongs to the exponential cone, see Appendix A.5. Then it can be solved using *exponential cone programming*, [132]. Our constraint would be given by $K_2 \geq D_{KL}(f_{MB}, f)$ and is equivalent to

$$K_2 \geq D(f_{MB}, f) \iff -K_2 \leq f_{MB} \log(f/f_{MB}) \iff (f, f_{MB}, -K_2) \in K_{\text{exp}}, \quad (103)$$

where the exponential cone K_{exp} is described in Appendix A.5. Our optimization problem can be therefore written as

$$\textbf{Optimize: } N^{(A)}(c_{\vec{v}_1}, \dots, c_{\vec{v}_n}) = \sum_{i=1}^n c_{\vec{v}_i} N_{\vec{v}_0}^{(A)} \quad (104)$$

subject to:

$$\sum_{i=1}^n c_{\vec{v}_i} = 1$$

$$-K_2 \leq f_{MB}(\vec{v}_i) \log(c_{\vec{v}_i}/f_{MB}(\vec{v}_i))$$

$$c_{\vec{v}_i} \geq 0$$

and solved using **CVXPY**. We would like to point out that, in the consulted literature, the *KL-divergence* is typically used in convex optimization problems as the objective function, but not as a constraint of the optimization problem under consideration. We can safely state that this methodology is maybe not new but definitely not widespread, not only in this physics context but in generic convex optimization studies.

5.3 Analyzing the impact of astrophysical uncertainties in CRESST III

In the previous section, we have presented our methodology to account for astrophysical uncertainties at direct detection experiments and neutrino searches. In this section, we will use it to derive upper limits on the dark matter mass-cross section of the CRESST III experiment, [18], accounting for deviations with respect to the Maxwell-Boltzmann velocity distribution. Our results go from the most aggressive limit to the most conservative, although in some cases we will stop the computation once the deviations lead to velocity distributions kinematically unseen by the experiment. We will use the different distance measures that we have discussed in section 5.2 to parameterize the deviations, in order to analyze the obtained results properly and cross-check them. We will perform our computation for both spin-independent, see Figure 21, and spin-dependent cases, see Figure 22. We will use Poissonian statistics, even though the CRESST collaboration usually present their limits using the Yellin methods, [133]. Hence, our limits will be generally more conservative than the official CRESST ones. Nevertheless, at sufficiently low masses, $m_\chi \leq 2$ GeV, which is the range in which CRESST is a competitive experiment, see Figure 19, our spin-independent limit (when using the SHM), matches the CRESST official one or even performs better at sub-GeV masses. For the spin-independent limits we have implemented the CRESST III experiment into the DDCalc-2.2.0 software, [134][135], while for the spin-dependent case we have used a self-implemented code from scratch, using the energy recoil data and efficiencies provided by the CRESST collaboration in [136]. In Appendix C, we discuss the different statistics and compare explicitly the performance between different statistical techniques, including a dedicated discussion about the DDCalc-2.2.0 software.

In the following, we discuss the results presented in Figure 21 and 22. We will only discuss the spin independent results, since the conclusions apply analogously for the spin dependent case. In the upper left plot of Figure 21, CRESST III poissonian upper limits are computed using *relative differences* as a distance measure to compute deviations from the SHM in the way described at [121], for both the minimization and maximization cases. Our results present a similar behaviour than [121], although their work was performed for XENON1T, PICO, and IceCube experiments. In the upper right panel, the parameterization chosen is the *total variation distance*. In the lower left we use the *Neyman χ^2 divergence*, and on the lower right we work with the *KL-divergence*.

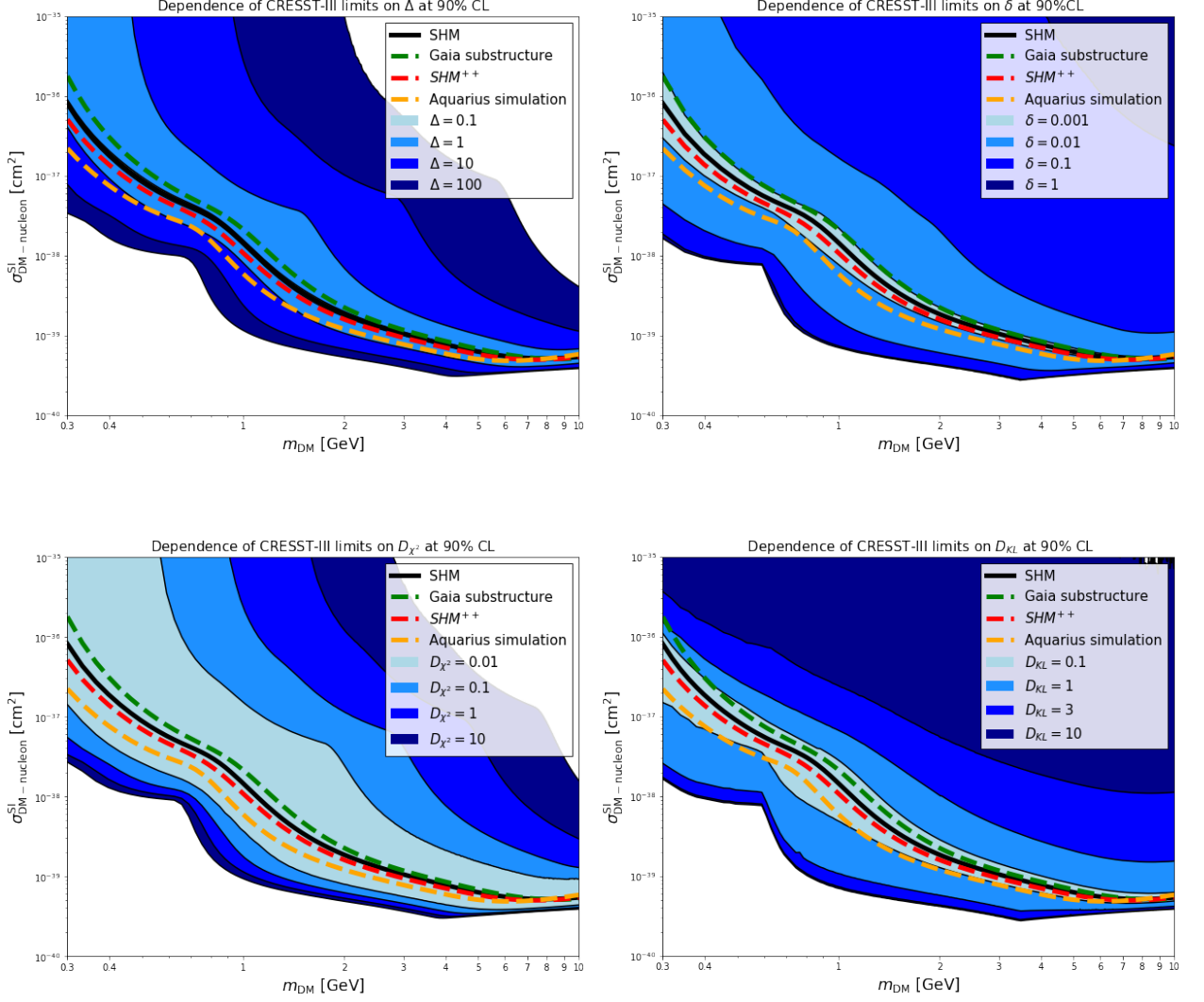


Figure 21: CRESST III spin-independent upper limits on the dark matter mass-cross section parameter space for different deviations w.r.t the Maxwell-Boltzmann (MB) distribution, at 90% CL. The colour bands represent the feasible set of velocity distributions that satisfy the CRESST III constraint and deviate a certain value with respect to the MB. We show in dotted colours the specific results for three different halo models discussed in section 2.2. The SHM limit is shown on solid black. The neutrino floor for CaWO_4 , [111] lies below our plot boundaries. The results are valid for both DM-proton and DM-neutron elastic scattering, setting $f^p = f^n$, see equation 74. The different plots show the results obtained for different distance measures: *Relative differences* (upper left), *total variation distance* (upper right), *Neyman χ^2 -divergence* (lower left) and *KL-divergence* (lower right). These plots have been obtained using DDCalc-2.2.0, [135] and a discretization in velocity space of 2000 points.

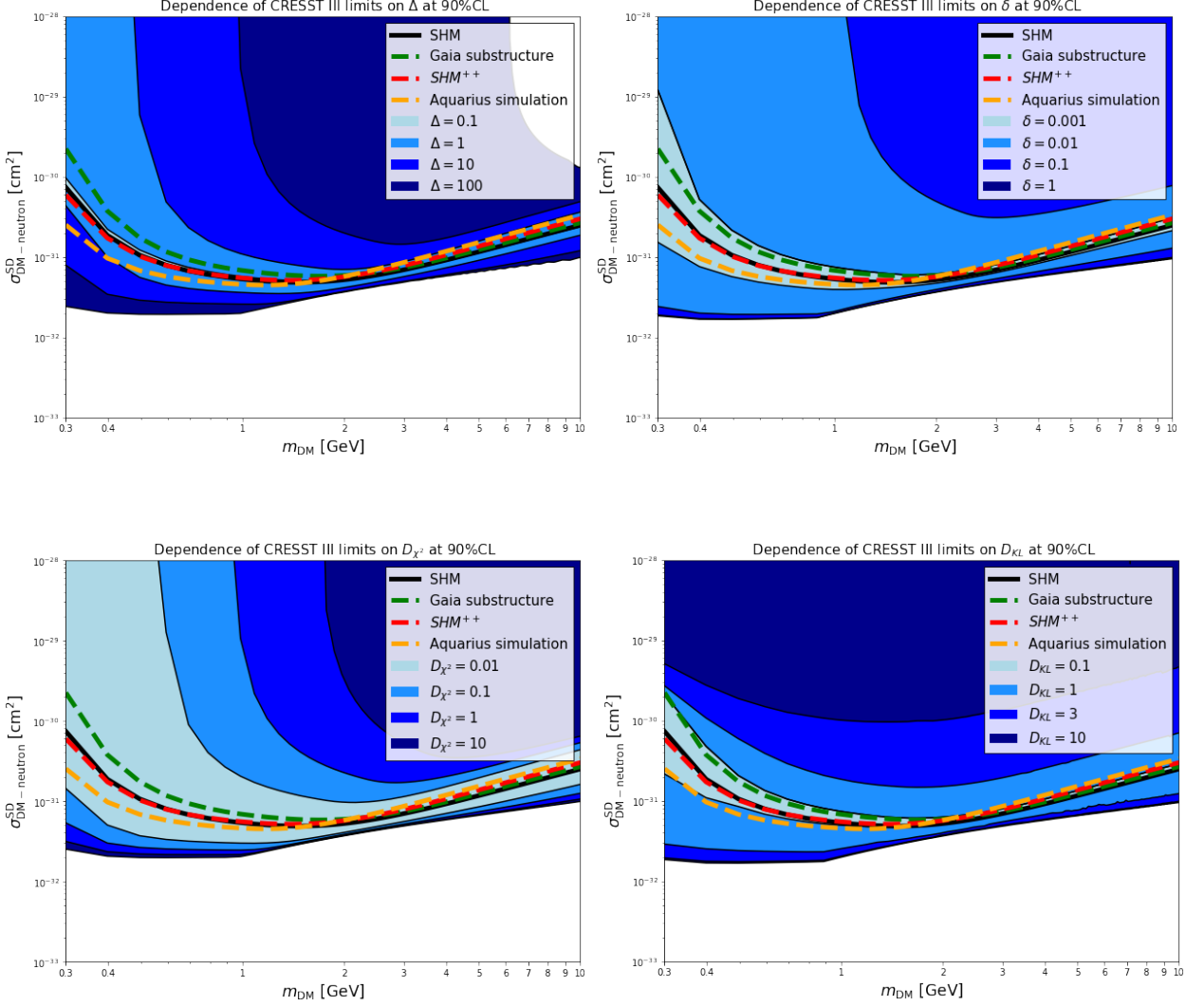


Figure 22: CRESST III spin-dependent upper limits on the dark matter mass-cross section parameter space for different deviations w.r.t the Maxwell-Boltzmann (MB) distribution, at 90% CL. The colour bands represent the feasible set of velocity distributions that satisfy the CRESST III constraint and deviate a certain value with respect to the MB. We show in dotted colours the specific results for three different halo models discussed in section 2.2. The SHM limit is shown on solid black. The neutrino floor for CaWO_4 , [111]. The results are valid for DM-neutron elastic scattering, and would differ for DM-proton case, see section 4.2.2. The different plots show the results obtained for different distance measures: *Relative differences* (upper left), *total variation distance* (upper right), *Neyman χ^2 -divergence* (lower left) and *KL-divergence* (lower right). These plots have been obtained using our own code implementation, not yet publicly available, where we have used the ^{17}O isotope of CaWO_4 CRESST target in the abundance given by [18]. The discretization space was reduced to 100 points due to the larger computational cost of this implementation. We notice however that the difference between 100 and 2000 points is merely aesthetical, and that physics output is analogous.

The maximization case is not specially interesting, since most distance measures perform in a similar way approaching a single stream of all dark matter particles moving at the Milky Way escape velocity. For the minimization case, the discrepancy between different methods is not only due to their different scaling, which is difficult to determine for the case of *relative differences*, since it is a point-to-point comparison between both distributions and the information divergences are given by a single number (point-to-point deviations are integrated), but also due to the way in which the distance measure applies. At low masses, the *relative differences* behaviour can be explained kinematically. As Δ increases, the high velocity tail is suppressed and, at some certain deviation, the experiment is not sensitive to such velocity distributions anymore. This is clearly visible in Figure 23, where the optimized velocity distributions for the different distance measures used are shown. We notice that the χ^2 -*divergence* shows a similar behaviour as the relative differences, being the deviation at low masses very large $m_{DM} \sim 0.6$ GeV, and compensated at high masses, $m_{DM} \sim 10$ GeV, where the experiment is kinematically sensitive to the complete velocity spectrum and deviations are washed out. They are washed out because the χ^2 -*divergence* optimized velocity distributions present a very particular shape of two pronounced peaks in both the low and high velocity tails, suppressing completely the Maxwell-Boltzmann most probable speed peak, see Figure 23.

The *total variation distance* and the *KL-divergence* perform quite differently. The *total variation distance* shows a larger impact of astrophysical uncertainties at low masses, but the optimized velocity distributions do not lie completely below the velocity threshold of the experiment, but retain a fraction of the kinematically accessible spectrum, so that the bands do not deviate so sharply at low masses. This effect is more pronounced in the case of the *KL-divergence*, which does not suppress the high velocity tail at low dark matter masses, and this explains that the upper limits do not deviate so largely w.r.t to the collaboration upper limit. The *KL-divergence* parametrization tells us, against our kinematic intuition, that there could be feasible velocity distributions that cause an uncertainty in the results shown by the CRESST experiment that is larger at high masses than at low masses. This can happen since the *KL-divergence* does not penalize the high velocity tail so strongly but smoothly interpolates between the Maxwell-Boltzmann-like velocity distribution and the most aggressive/conservative velocity distributions. The CRESST experiment is sensitive to the complete dark matter velocity spectrum at 10 GeV, so differences between the distributions at low masses are taken into account. For sufficiently low masses $m_{DM} \leq 1$ GeV, only the high velocity tail is seen and there the KL does not penalize it so strongly, therefore being the difference in the upper limits not so large. We notice that Pinsker's inequality presented in Theorem 1 holds for our analysis. Indeed, the *total variation distance* scaling is significantly lower than the *KL-divergence*, obtaining similar deviations for values of $\delta = 0.001$ and $D_{KL} = 0.1$ in the case of the *total variation* and the *KL-divergence*, respectively. We have, as well, shown the upper limits for three specific halo models discussed in section 2.2 in dotted colours. We notice that for each distance measure, even though the deviation is not so strong, $\mathcal{O}(1)$ uncertainties, these fall in different bands, which motivates the need of using different distance measures to make a proper halo-independent analysis. In Table 2, we have computed the distance measure between different halo models and the Maxwell-Boltzmann velocity distribution, in order to get a hint of which deviations (bands) of our analysis are consistent with experimental results and are physically motivated. We notice that, in the case

of tracers studies, see section 2.2.3, we obtain deviations in the lightest and next to lightest blue bands, leading in some regions to uncertainties of $\mathcal{O}(10 - 10^2)$. For the case of N-body simulations, these uncertainties can reach values of $\mathcal{O}(10^3)$ in some regions of the parameter space. These of course depend on the distance measure under consideration and remark that for the *KL-divergence* we do not encounter physically motivated deviations larger than $\mathcal{O}(1)$.

Deviations from SHM for different velocity distributions				
Distance measure	SDSS-Gaia DR2	SHM ⁺⁺	Aquarius simulation	Eagle simulation
Averaged Δ	0.37	2.06	4.25	22.95
Max Δ	5.3	102	164	1256
Total variation	0.0064	0.0033	0.0083	0.0086
KL divergence	0.037	0.019	0.14	0.22
χ^2 (Neyman)	0.060	0.096	0.73	9.73

Table 2: Deviations from SHM for different velocity distributions and distance measures. Since the relative difference is a point-to-point comparison, we show the average value and the maximum value of the array of deviations. This table is used as a reference to interpret the results of Figure 21 and 22.

We notice in Table 2 that *relative differences* and the χ^2 -*divergence* yield larger deviations for the SDSS-Gaia DR2 w.r.t the SHM than the SHM⁺⁺, while for the *total variation distance* and the *KL-divergence* happens the contrary. By looking at Figure 13, where we plotted all velocity distributions discussed in this thesis, we notice that SDSS-Gaia DR2 presents a good agreement with the SHM up to velocities of ~ 200 km/s. On the other hand, the SHM⁺⁺ deviates w.r.t the SHM for all points in velocity space from velocities of ~ 100 km/s. The average *relative differences* between points on the SHM⁺⁺ and the SHM is therefore larger than for SDSS-Gaia DR2 when considering the complete velocity spectrum. A similar behaviour occurs with the χ^2 -*divergence*, since it represents the integration of all squared *relative differences*, see equations 90 and 99. On the contrary, the *total variation distance* compute a larger deviation for SDSS-Gaia DR2, since this distance measure penalizes the absolute maximum deviation between two points of the distributions, which is clearly larger in SDSS-Gaia DR2 for points near peak speed ~ 320 km/s. The same occurs for the the *KL-divergence*, since this distance measure accounts for the relative entropy, although the interpretation here is more subtle. In Figure 23 we appreciate that the optimized velocity distributions obtained with the *KL-divergence* parametrization are smoother than the optimized velocity distributions obtained with different distance measures, and penalize less the

high-velocity tail than the rest. This helps to understand why this distance measure yields larger deviations of the SDSS-Gaia DR2 than the SHM⁺⁺, since SDSS-Gaia penalizes the region close to the peak speed and the low velocity tail more than the SHM⁺⁺.

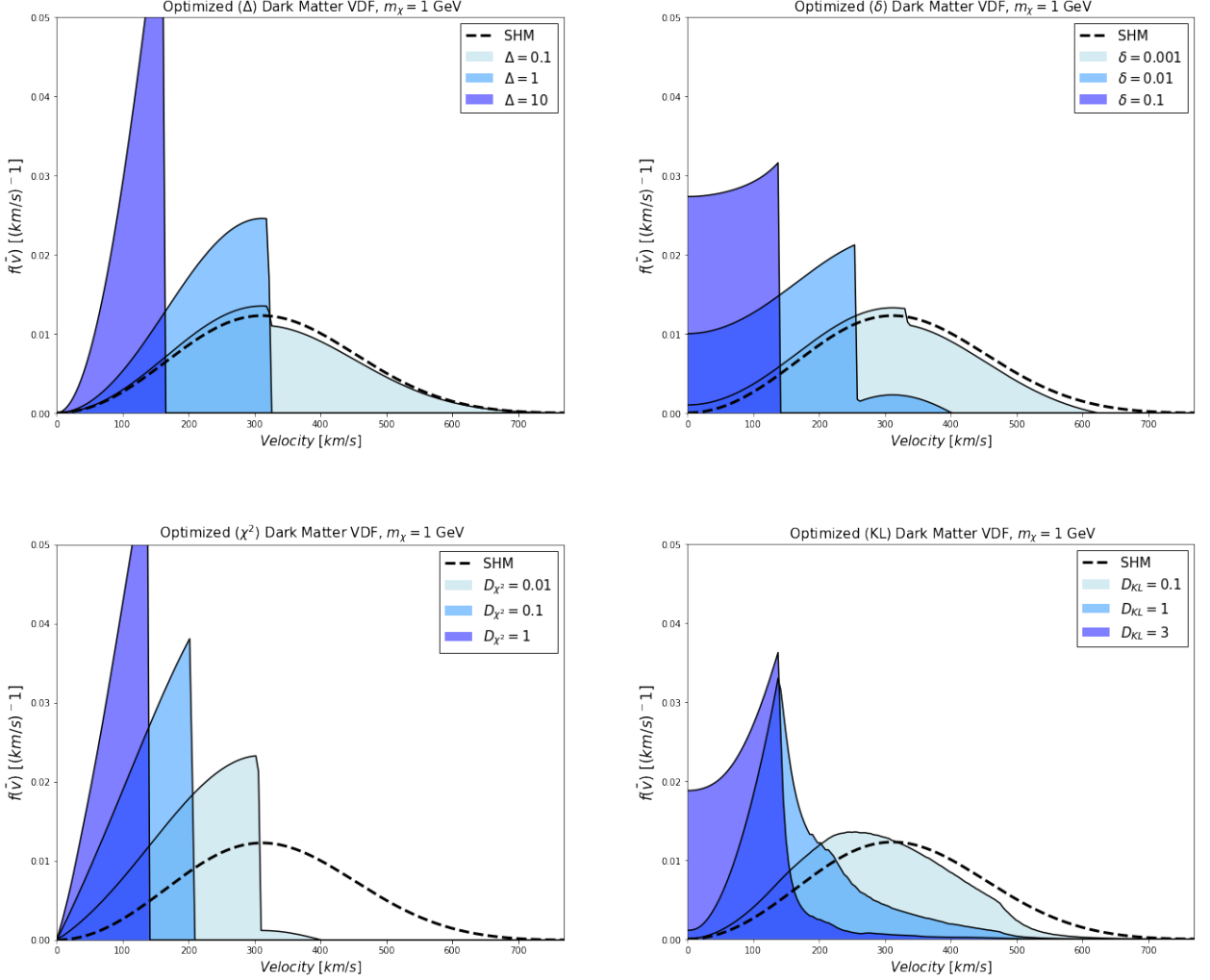


Figure 23: Optimized velocity distributions for different distance measures and deviations w.r.t the Maxwell Boltzmann velocity distribution, for a dark matter particle mass of $m_\chi = 1 \text{ GeV}$ and a fixed cross section of $\sigma_\chi = 10^{-40} \text{ cm}^2$.

From all the above discussion, the *KL-divergence* is the distance measure that yield more conservative results and therefore the most suited for a halo-independent analysis. We conclude that the *KL* divergence is a statistically more robust way to account for astrophysical uncertainties than the *relative differences* used in [121], since it is less constrained by initial assumptions on the shape of the distribution, and the feasible set of velocity distributions that respect their constraint is more varied than for other distance measures. The presence of the logarithm causes the optimized velocity distributions to present smoother shapes, that could match physically motivated velocity distributions like those discussed in section 2.2. However, we emphasize that this methodology does not reconstruct the dark matter velocity distribution from CRESST data, but rather are mathematically optimized distributions that allow for an interpolated model-independent analysis.

5.4 A proof of concept : Ruling out specific DM models

In this section, we will apply our methodology for the specific purpose of testing in a halo-independent manner concrete dark matter particle models. In particular we will study the viability of Z -mediated dark matter, [137][138][139], and *Sneutrino* dark matter, [140][141][142], dark matter.

5.4.1 Testing Z -mediated DM in a halo-independent manner

The Z -boson and the Higgs are the only particles naturally present in the Standard Model which are able to play the role of mediator between the visible and the dark sector. The Z -portal scenario is present in a large number of extensions of the SM (sneutrinos, higgsinos, heavy neutrinos, models involving kinetic mixing or dark photons, etc), [140][143][144][145]. The lagrangian modelling the Z -boson mediated dark matter interaction with the SM sector is given by

$$\mathcal{L} = \frac{g}{4\cos\theta_W} (\bar{\chi}\gamma^\mu (V_\chi - A_\chi\gamma^5) \chi Z_\mu + \bar{f}\gamma^\mu (V_f - A_f\gamma^5) f Z_\mu), \quad (105)$$

with g the electroweak coupling ($g \approx 0.65$), $V_{f,\chi}$ and $A_{f,\chi}$ the vectorial respectively axial charges. f represents the SM fermions with:

$$V_f = 2(-2q_f \sin^2\theta_W + T_f^3); A_f = 2T_f^3, \quad (106)$$

θ_W being the Weinberg angle and T_f^3 the isospin number of the fermion f with electric charge q_f . At low energies, $\Psi\gamma^i\bar{\Psi} \rightarrow 0$ and $\Psi\gamma^0\gamma^5\bar{\Psi} \rightarrow 0$, and thus only $V_\chi\Psi\gamma^0\bar{\Psi}Z_\mu$ vector-vector and $A_\chi\Psi\gamma^i\gamma^5\bar{\Psi}Z_\mu$ axial-axial interactions are not suppressed by powers of velocity or momentum transfer, [138]. Therefore, The spin-independent (SI) WIMP-nucleon elastic cross section is exclusively dependent on V_χ and the spin-dependent (SD) WIMP-nucleon elastic cross section on A_χ . They can be derived from the lagrangian 105. We take the formulae provided by [137] but use our own notation consistent with the discussion performed in section 4.2. For the SI case we have

$$\sigma_{SI}^p = \frac{g^4 |V_\chi|^2 \mu_{\chi p}^2}{4\cos^2\theta_W \pi m_Z^4} \frac{[\alpha_u^V (A + Z) + \alpha_d^V (2A - Z)]^2}{A^3}, \quad (107)$$

$$\sigma_{SI}^n = \sigma_{SI}^p \frac{\mu_{\chi n}^2 (2\alpha_u^V + \alpha_d^V)^2}{\mu_{\chi p}^2 (\alpha_u^V + 2\alpha_d^V)^2}, \quad (108)$$

where m_Z is the Z -boson mass, and $\alpha_{u,d}$ are the vector-vector coupling constants for u and d quarks, respectively, as it was already described in section 4.2.1. For the SD case the cross section reads

$$\sigma_{SD}^p = \frac{3kg^4 \mu_{\chi p}^2}{4\cos^2\theta_W \pi m_Z^4} \left[\frac{\alpha_u^A (\Delta_u^p S_p^A + \Delta_d^p S_n^A) + \alpha_d^A ((\Delta_d^p + \Delta_s^p) S_p^A + (\Delta_u^p + \Delta_s^p) S_n^A)}{S_p^A + S_n^A} \right]^2, \quad (109)$$

$$\sigma_{SD}^n = \sigma_{SD}^p \frac{\mu_{\chi n}^2 (\alpha_u^A \Delta_u^p + \alpha_d^A (\Delta_d^p + \Delta_s^p))^2}{\mu_{\chi p}^2 (\alpha_u^A \Delta_u^n + \alpha_d^A (\Delta_d^n + \Delta_s^n))^2}, \quad (110)$$

where $k = 4$ for Majorana dark matter and $k = 1$ for Dirac dark matter. We included this factor here, while it was skipped in [137]. $S_{p,n}^A$ are the proton and neutron contributions to the nucleus spin. $\Delta_q^{(p,n)}$ describe the amount of spin carried by a quark of flavor q inside the proton and neutron. Their results are given by [117] as it was discussed in section 4.2.2. For a target detector with several isotopes it is necessary to sum the terms depending on A, Z over all of them weighted by their relative abundance in the material. For the SD case only the isotopes with odd number give non-zero contribution, as we discussed in section 4.2.2

Due to the dark matter relic abundance constraint, [11], large vectorial couplings are indeed prohibited by direct detection limits, [137]. In all these extensions, the axial and vectorial coupling are assumed to be of the same order of magnitude coupling $A_\chi \approx V_\chi$. The reason is that in a framework of $SU(2)_L \times U(1)$ breaking the original $SU(2)_L$ condition $A_\chi = V_\chi$ is only mildly modified by the dynamic of the breaking.

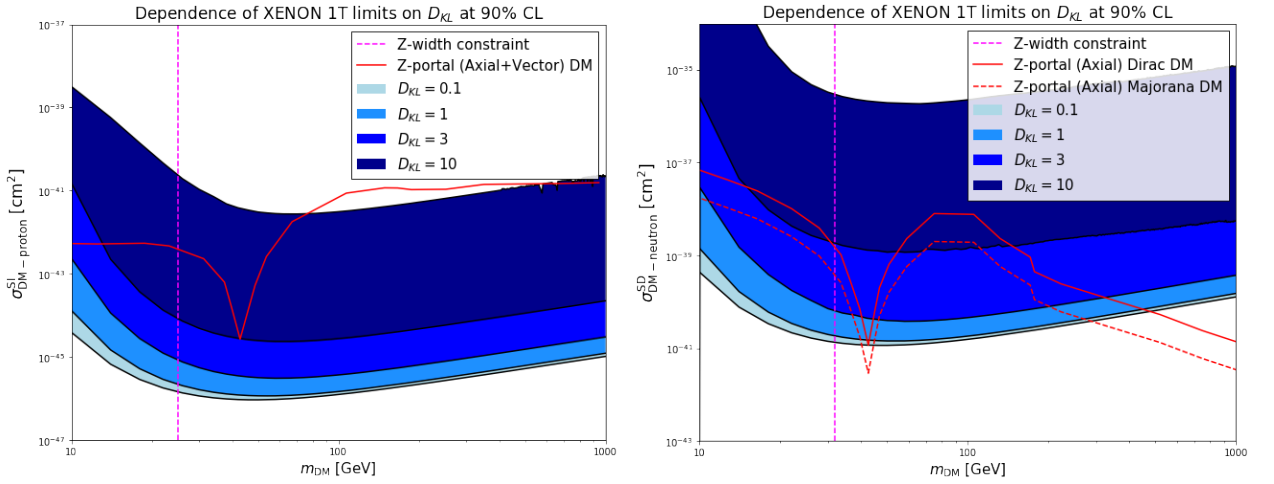


Figure 24: Dependence of XENON 1T upper limits on D_{KL} at 90% CL, for spin independent (left) and spin dependent (right) scattering with protons and neutrons, respectively. The coloured bands correspond to the minimization case of problem 104 only. In dotted pink a constraint from the invisible Z -width from LEP is shown, [33]

The left plot of Figure 24 shows the Z -mediated WIMP-neutron SI cross section when considering equal axial and vectorial couplings ($A_\chi = V_\chi$) and the dependence of XENON 1T limits on deviations from the SHM using the KL -divergence. A lower bound coming from the Z -invisible width from LEP, [33], and the dark matter relic abundance is also shown, [138]. It was already known from previous analyses that the XENON1T results restricted the viability of such a dark matter candidate, [137], [138]. The novelty here is that, even when considering astrophysical uncertainties in a strongly conservative manner, that is, for $D_{KL}(f_{MB}, f) = 10$, the region of the parameter space between ~ 15 -1000 GeV remains excluded. The region near the Z -boson mass pole is still ruled out for conservative deviations of $D_{KL}(f_{MB}, f) = 3$. It is only for sufficiently low masses $m_\chi \leq 15$ GeV, that moderate deviations from the Maxwell-Boltzmann, $D_{KL}(f_{MB}, f) = 1$, could rescue this model. This region would still be incompatible with the collider bound from the invisible Z -width. Also, it is important to notice, as it can be seen in table 5.3, that most halo models considered in

the literature deviate from the Maxwell-Boltzmann in the range $D_{KL}(f_{MB}, f) \in (0, 1)$, and no region of the parameter space of SI interacting Z -mediated DM can be rescued for such deviations.

The interpretation of the results for SD WIMP-neutron interaction (only-axial Z -mediated) shown in Figure 24 is quite different. The lower bound coming from the invisible Z -width $m_\chi \geq 32\text{GeV}$ is slightly more constraining, [138]. Results for both Dirac and Majorana particles are shown. In this case, the region near the Z -mass pole can be rescued when considering small deviations from the SHM, $D_{KL} \in (0, 3)$. This model also alleviates the XENON1T bound for masses larger than $m_\chi \geq 100\text{ GeV}$ within $D_{KL} \in (0, 3)$, and escape completely the SHM limit for $m_\chi \geq 300\text{ GeV}$, for Majorana dark matter, and $m_\chi \geq 500\text{ GeV}$, for Dirac dark matter. The SD WIMP-neutron cross section weakens at high masses, since the relic abundance constraint needs to be saturated. Analogously to the SI case at low masses, moderate deviations from the SHM allow to recover this region of the parameter space, though still in contradiction with the Z -width constraint.

We would like to point out that deviations obtained with different distance measures, such as the *total variation distance* or the χ^2 -*divergence*, yield more conservative results at high masses, being the "recovery" of the Z -mediated model even less spectacular, though near the Z pole and at low masses the results would be much more aggressive as we discussed for the CRESST III results in section 5.3. Nevertheless, we also argued there the suitability of the KL -*divergence* to account for astrophysical uncertainties and therefore the presented results are the most reliable statistically. More technical discussions regarding the validity of these results is still convenient and this section only pretends to be a *proof of concept* of our developed halo-independent analysis, aiming to show its possibilities to discuss direct detection bounds on specific dark matter models. In next section we will go one step beyond and analyze a particular class of Z -mediated models: *Sneutrino* dark matter in the Minimal Supersymmetric Standard Model (MSSM).

5.4.2 Testing *Sneutrino* DM in a halo-independent manner

The usual supersymmetric frameworks provide the neutralino as the lightest supersymmetric particle (LSP), fully stable, (i.e it does not decay), and thus a natural dark matter candidate. Neutralinos are mass eigenstates of a linear superposition of the SUSY partners of the neutral Higgs and of the $SU(2)$ and $U(1)$ neutral gauge bosons [146]

$$\chi_i = \alpha_{i1}\tilde{B}^0 + \alpha_{i2}\tilde{W}^0 + \alpha_{i3}\tilde{H}_u^0 + \alpha_{i4}\tilde{H}_d^0. \quad (111)$$

In particular, the superpartner of the $U(1)_Y$ hypercharge gauge boson, the bino \tilde{B} , has received extensive discussion, [12], as it reproduces the observed dark matter cosmological abundance for certain choice of superpartner masses.

There is another natural election for the LSP : Sneutrinos. Sneutrino as a cold dark matter candidate has been studied in the past, [140][141][142]. Its simplest realisation in the Minimal Supersymmetric Standard Model (MSSM) is ruled out by the combination of direct detection + collider constraints. In the following, we will review the sneutrino as the LSP in the MSSM as it was already discussed in [141]. We will follow the notation and take the

same model parameters as [141]. This study does not pretend to be a model-building of sneutrinos in the MSSM. We only aim to contrast the result for the sneutrino cross section already derived in the past with the latest XENON1T results in a halo-independent manner, accounting conservatively for the dark matter astrophysical uncertainties.

In the MSSM, sneutrinos are the scalar partners of the left-handed neutrinos. Therefore it shares with the neutrino the same quantum numbers: both are electrically neutral, colorless, have same hypercharge but different masses, since SUSY is broken, and different spins. \hat{L}^I superfields contains the fermionic $SU(2)_L$ doublets $L^I \equiv (\nu_L^I, l_L^I)$ and its corresponding scalar doublets $\bar{L}^I \equiv (\bar{\nu}_L^I, \bar{l}_L^I)$, where $I = e, \mu, \tau$. All terms of the supersymmetric lagrangian including sneutrino fields are not shown here, [141]. The part of the superpotential relevant for the leptonic sector is

$$W = \epsilon_{i,j}(\mu \hat{H}_i^1 \hat{H}_j^2 - Y_l^{I,J} \hat{H}_i^1 \hat{L}_j^I \hat{R}^J), \quad (112)$$

where \hat{H}^1, \hat{H}^2 are the two Higgs-doublet superfields, R^J are the right-handed lepton superfields, μ is the usual Higgs mixing parameters and $Y_l^{I,J}$ is a matrix which contains the Yukawa couplings. In the MSSM, $Y_l^{I,J}$ is real and diagonal in flavour space and the Yukawa couplings are linked to the charged lepton masses by the usual relation $m_I = v_1 Y_l^{II}$, where v_1 is the vacuum expectation value of the neutral component of the H^1 Higgs field. The soft-supersymmetry breaking potential relevant for the sneutrino sector is:

$$V_{soft} = (M_L^2)^{IJ} \bar{L}_i^{I*} \bar{L}_j^J + [\epsilon_{ij}(\lambda_i^{IJ} H_i^1 \bar{L}_j^I \bar{R}^J) + h.c] \quad (113)$$

where λ_i^{IJ} is, as Y_l^{IJ} , real and diagonal in flavour space. M_L is also diagonal and all their values are taken equal to m_L in order to reduce the number of parameters. The scalar potential is then given by $V = V_{soft} + V_F + V_D$, where the D-term describe gauge interactions and the F-term is given by the derivatives of the superpotential W with respect to the scalar variables, [146].

From all what has been stated, the mass term for each family of the sneutrino field $\bar{\nu}_L$ is

$$V_{mass} = \left[m_L^2 + \frac{1}{2} m_Z^2 \cos 2\beta \right] \bar{\nu}_L^* \nu_L \quad (114)$$

where $\beta = \arctan(\frac{v_2}{v_1})$, and v_2 is the vacuum expectation value of the neutral component of the H^2 Higgs field. In this case, the three sneutrinos are also (degenerate) mass-eigenstates with squared-mass $m_1 = m_L^2 + \frac{1}{2} m_Z^2 \cos(2\beta)$. m_1 refers to the mass of the lightest sneutrino mass eigenstate. The phenomenology of the sneutrino slightly depends on β , so that m_L is the main free parameter.

Colliders present experimental bounds for MSSM sneutrinos. Colliders bound arise due to the non-observation of the corresponding charged sleptons. If only considering low-energy supersymmetry, it is assumed in [141] that all the soft mass parameters of the charged and neutral leptons are common at the electroweak scale and $m_L = m_R$ is set. In this case the lower bound of the sneutrino mass is the same as the one coming from the invisible width of the Z boson, [33], yielding $m_{\bar{\nu}} \geq 43.7 GeV$ for one neutrino species and $m_{\bar{\nu}} \geq 44.7 GeV$ for three degenerate sneutrinos.

The sneutrino relic abundance can be computed, by taking into account all the relevant annihilation channels and coannihilation processes which may arise when the sleptons are close in mass to the sneutrinos, [140]. We do not show them here but refer to [140][141]. We use the results on the sneutrino mass m_1 -nucleon scattering cross section from [141], which use the following parameters: the consideration of neutralinos at least 30% heavier than the lightest sneutrino, so that the lightest neutralino mass is $m_\chi = \min(294\text{GeV}, 1.3m_1)$, and the values for the Higgs masses, which are 120 GeV (notice that this value is outdated, but it does not affect the results significantly) for the lightest CP-even state h and at 400 GeV for the heaviest CP-even H and for the CP-odd state A

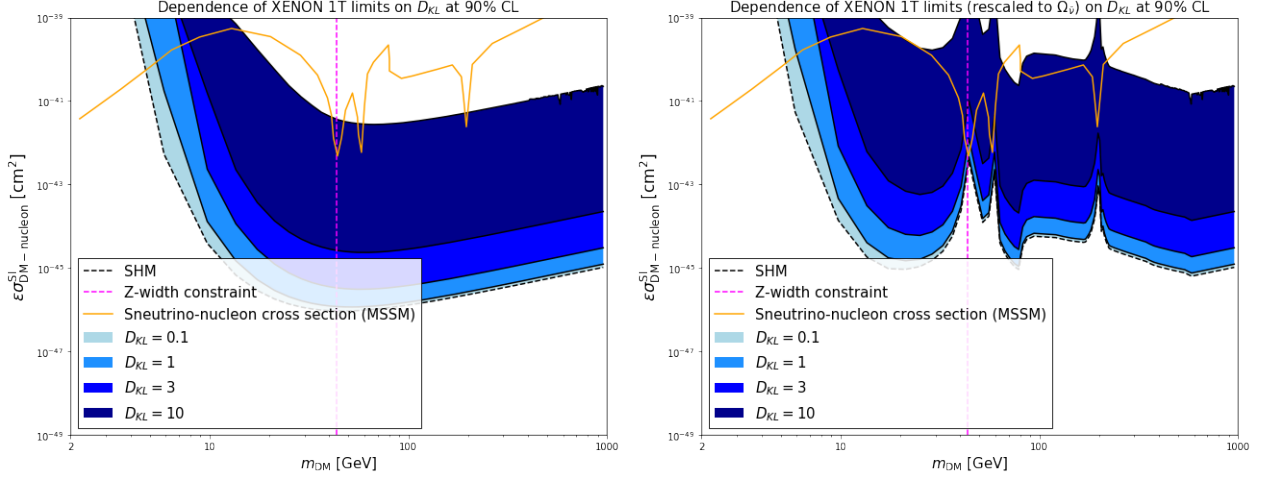


Figure 25: Dependence of XENON1T limits on D_{KL} at 90% CL, contrasted to the spin independent sneutrino-nucleon scattering cross section taken from [141]. A lower bound on the sneutrino mass coming from invisible Z -width constraint is also shown in dotted magenta. The factor ϵ accounts for the rescaling of the sneutrino cross section that saturates the cosmological sneutrino relic abundance. On the right plot, we have naively scaled the XENON1T limits to the case in which the local density of dark matter particles for each mass would be given by the cosmological sneutrino abundance multiplied by the canonical value of $\rho_{loc}=0.3 \text{ GeV}/\text{cm}^3$. The three poles in the sneutrino cross section refer (from left to right) to the Z , h to the degenerate H and A poles in the (co)annihilation cross section, which occur when m_1 is close to half the mass of the exchanged particle.

The results of Figure 25 show that sneutrino in the MSSM as described in [140][141] remains ruled out when considering strong deviations from the Maxwell-Boltzmann velocity distribution $D_{KL}(f_{MB}, f) \in (0, 10)$ in the region of the parameter space 10-1000 GeV. For lower masses the model escapes the XENON1T bounds as well as further experimental bounds from low mass experiments such as CRESST, but these sneutrino masses are in contradiction with the invisible Z -width constraint. Furthermore, for such low masses, the sneutrino cosmological relic abundance is far from being in agreement with the dark matter relic abundance. When rescaling XENON1T bounds to the sneutrino relic abundance, the discrepancy is slightly alleviated but still strong. There might be a saviour for sneutrinos in supersymmetric theories with lepton number violation, [24]. These would cause a lift between the sneutrino's odd and even CP eigenstates $\bar{\nu}^+, \bar{\nu}^-$, that would prevent elastic scattering through Z -exchange. We discuss some aspects of inelastic scattering in section 7.2. Here, we

can conclude that sneutrino dark matter in the MSSM scattering elastically with nuclei is ruled out independently of the dark matter halo by the XENON1T experiment.

5.5 Combined halo-independent analysis of CRESST II and SK

The Icecube and Super-Kamiokande collaborations are able to reconstruct the directionality of neutrino-like events in their detectors and thus quantify the flux of neutrinos coming from the Sun. Therefore, according to the WIMP capture mechanism and annihilation in the sun described in section 3.2.1, they are able to present limits in the dark matter m_χ - σ_χ parameter space for a non-observation of an excess of the flux of neutrinos coming from the sun. These experiments are able to compare the observed angles and energy spectrum to signal expectations from different simulated WIMP masses and annihilation channels induced neutrino fluxes, [84][21]. All three flavours of signal neutrinos are considered in their analyses. When WIMPs annihilate into W^+W^- , the W bosons decay promptly and neutrino emission from the leptonic decay channels peaks at energies close to the mass of the WIMP. The $\tau^+\tau$ channel produces a similar distribution of neutrinos in energy with a higher overall normalization. When the WIMP annihilates predominantly to bottom quarks $b\bar{b}$, the neutrino emission peaks at energies much below the mass of the WIMP, since the b quarks hadronize before they can decay to produce neutrinos, [84].

There is extensive work dedicated to perform combined halo-independent analyses of Icecube and Super-Kamiokande with direct detection experiments for both SI and SD dark matter, [120][121][147]. Nevertheless, we notice that these studies predominantly use the stringent results of direct detection experiments such as XENON1T, LUX or PICO. It happens though, that such experiments are only sensitive to the high velocity tail of the dark matter velocity distribution at low masses ($m_\chi \leq 10$ GeV), due to their limited energy thresholds. This kinematical constraint has been discussed in section 4.1. Furthermore, as we also explained in section 3.2.1, the capture mechanism sets an upper bound on the WIMP velocities that can get gravitationally bound by the sun. This upper bound is larger as the WIMP mass gets smaller: $v_{max}(r) \propto \frac{\sqrt{m_{DM}m_N}}{|m_{DM}-m_N|}$. As an example, the LUX direct detection experiment velocity threshold for a dark matter mass of 4 GeV, is of ~ 640 km/s. The point that we aim to show here is that the upper velocity $v_{max}(r)$ of such a dark matter particle will be smaller than this value for several elements in the sun, while for others the difference between these velocity thresholds will be, comparatively to the whole dark matter velocity spectrum, very small. This fact, while it doesn't prevent from performing such a halo-independent analysis in the low mass range, lacks from reliability, as it is very sensitive to small changes in the phase-space distribution of the dark matter particles (e.g the distribution could shut-off just below this values, being therefore no 4 GeV dark matter particles having velocities in the analysis range). Notice that the above discussion is not applicable for larger dark matter masses $m_\chi \geq 10$ GeV, since Xenon-based dark matter experiments are able to prove a larger region of the velocity space for such dark matter masses.

Being exposed this issue, and in order to complement these analyses in the dark matter mass range from 4 GeV to 10 GeV accounting for a wider region of the velocity space, we need to combine Super-Kamiokande results with a direct detection experiment with a lower energy

(velocity) threshold, such as the CRESST experiment. Though the CRESST III run has a lower energy threshold than CRESST II, we use the last one due to its stringent results (larger exposure) for sufficiently high masses. The difference between using CRESST II or CRESST III is not indeed very relevant since both runs cover almost completely the velocity space for dark matter masses above 4 GeV. Lower masses can't be proven by neutrino searches due to dark matter evaporation effects in the Sun, [89]. According to the method described in problem 89, our minimization problem takes the form:

$$\text{Minimize: } C^{(SK)}(c_{\vec{v}_1}, \dots, c_{\vec{v}_n}) = \sum_{i=1}^n c_{\vec{v}_i} C_{\vec{v}_i}^{(SK)} \quad (115)$$

subject to:

$$\sum_{i=1}^n c_{\vec{v}_i} = 1$$

$$R^{(CRESST)}(c_{\vec{v}_1}, \dots, c_{\vec{v}_n}) \leq N_{obs}^{CRESST}$$

$$c_{\vec{v}_i} \geq 0$$

where N_{obs}^{CRESST} is the poissonian number of observed events by CRESST at 90%CL. The dark matter cross section σ_χ can be consequently obtained from

$$2 \cdot \Gamma_{A,SK} = C^{(SK)}(c_{\vec{v}_1}, \dots, c_{\vec{v}_n}), \quad (116)$$

where $\Gamma_{A,SK}$ is the experimental annihilation rate result from SK, [21].

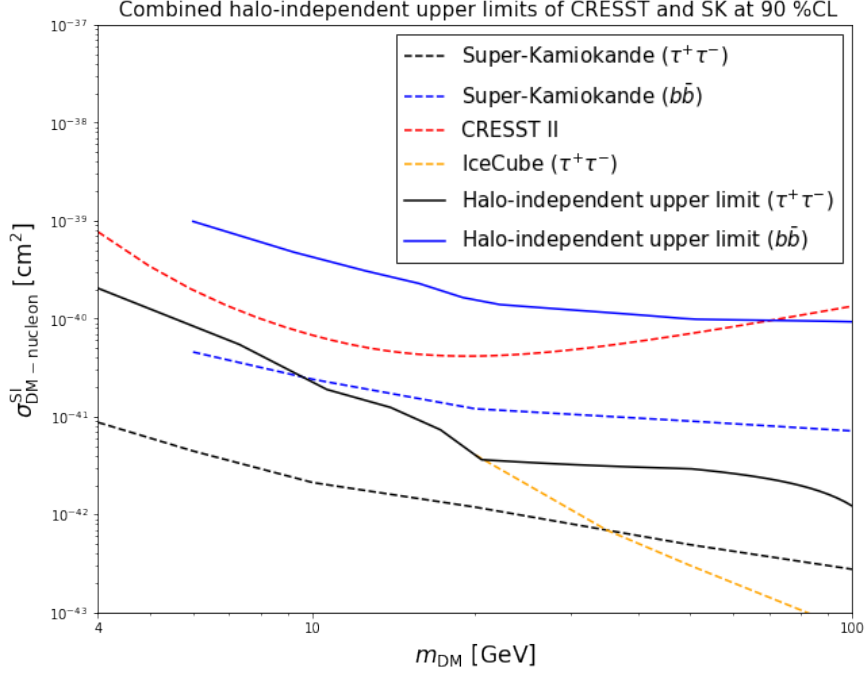


Figure 26: Combined halo-independent upper limits on the dark matter mass-spin independent cross section of CRESST II and Super-Kamiokande, for the most aggressive ($\tau^+\tau^-$, in solid black) and more conservative ($b\bar{b}$, in solid blue) annihilation channels. The annihilation of dark matter particles into W^+W^- is relevant for masses $m_{DM} \geq m_W$ however here omitted since the results lie between the other channels. The annihilation channel into taus goes down to $m_\chi \geq 6$ GeV, since lower masses are not kinematically allowed, [21].

Figure 26 shows the results of our calculation. We are particularly interested in the mass range going from 4 to 10 GeV, where our limits are most competitive compared to previous analyses, [120][121]. For the annihilation channel into taus $\tau^+\tau^-$, our halo-independent limit is ~ 1 order of magnitude more conservative than neutrino collaborations limit. For the annihilation channel into bottom quarks $b\bar{b}$, we also encounter a halo-independent limit $\mathcal{O}(1)$ more conservative than the Super Kamiokande bound.

6 A bayesian approach to the dark matter velocity distribution problem

In previous sections, we have been able to derive halo-independent upper limits on the dark matter mass-cross section by combining direct detection experiments and neutrino searches. Moreover, we have interpolated between the most aggressive and the most conservative upper limits from one single experiment by parametrizing the deviation with respect to the Maxwell-Boltzmann velocity distribution using information divergences (though our methodology shown in problem 102 allows to include more than one experiment). We briefly discussed in section 5.3 that the optimized velocity distributions that we obtain with such methodology are difficultly interpretable as feasible dark matter velocity distributions with a physical meaning. Instead, they are optimized mathematical solutions to our convex problem under consideration, even though the parametrization chosen to account for deviations with respect to the Maxwell Boltzmann highly impacts the shape of such distributions. We argued that the *KL-divergence* is the most suited distance measure to smoothly interpolate with respect to the Maxwell-Boltzmann, since it consists in the relative entropy between two distributions and the Maxwell-Boltzmann is constructed on entropic grounds, as we discussed in section 2.2.4. There, we constructed the maximally entropic velocity distribution under basic physically-motivated requirements (conservation of energy and uniform discretization of phase space). In this section, we aim to combine elements of both approaches, to try to extract real and useful information about the dark matter velocity distribution from the non-observation of dark matter at experiments, using Bayes theorem. Our work will be motivated by similar studies, [124][148], although our approach will include noticeable differences and will be solvable using convex optimization techniques, see Appendix A.1.

6.1 The quantified maximum entropy method

According to Bayes theorem

$$p(f|data, prior) = \frac{p(data|f, prior) \cdot p(f|prior)}{p(data|prior)}, \quad (117)$$

and using Markov's assumption, which considers that a variable x_t depends only on its direct predecessor state x_{t-1} and not on $x_{t'}$ with $t' < t - 1$ [150],

$$p(f|data, prior) = \frac{p(data|f) \cdot p(f|prior)}{p(data|prior)}, \quad (118)$$

where we will consider f as the "updated" most credible prior dark matter velocity distribution, given the data as the null results from some direct detection experiments and the truncated Maxwell-Boltzmann velocity distribution as the prior distribution. We want to apply the *principle of maximum entropy* discussed in section 2.2.4, but assuming this time the Maxwell-Boltzmann as a prior knowledge. For this we will follow the *quantified maximum entropy* approach, [149]. This method was proposed by J. Skilling as a technique for obtaining probabilistic estimates of positive additive probability distributions from noisy and incomplete data. Skilling proposes the construction of an entropic prior that penalises deviations from our prior knowledge, which in our case is the Maxwell-Boltzmann velocity

distribution $f_{MB}(\vec{v})$. Thus, we construct an entropic prior making use of the *KL-divergence* (relative entropy), already discussed in section 5.2, equation 100

$$p(f|prior) \propto e^{-\beta D_{KL}(f_{MB}, f)}, \quad (119)$$

where β is a regularization parameter which describes the strength of our prior information: $\beta = 0$ corresponds to no prior information while $\beta \rightarrow \infty$ corresponds to $f(v) = f_{MB}(v)$ regardless of any data, [124]. For the probability of having the data given a certain velocity distribution $p(data|f)$, we can use a χ^2 factor that penalises deviations from the observed data

$$\chi^2[f]^{(\alpha)} = \sum_{\alpha} \left(\frac{R_{f(v)}^{(\alpha)}(\sigma_{DM}, m_{DM}) - N_{obs}^{(\alpha)}}{\Delta^{(\alpha)}} \right), \quad (120)$$

where we define $\Delta^{(\alpha)}$ to be the average uncertainty on the recoil spectrum energies of a dark matter direct detection experiment α , and $R_{f(v)}^{(\alpha)}(\sigma_{DM}, m_{DM})$ is the expected dark matter scattering rate of a direct detection experiment α for a certain velocity distribution, dark matter-nucleon cross section and dark matter mass.

The factor in the denominator reflects the probability of having the data given the prior and can be constructed by a constant factor,

$$p(data|prior) = e^{\frac{1}{2}\chi^2(f_{MB})}. \quad (121)$$

The posterior probability then takes the form,

$$p(f|data, prior) \propto e^{-\beta D_{KL}(f_{MB}, f) - \frac{1}{2}\chi^2(f)}, \quad (122)$$

which is a convex function and can be transform in a solvable second order cone problem SOCP, see Appendix A.4. We can interpret β by noting that an n nat (natural unit of information, see Appendix B.1) departure from $f(v)$ is punished by a factor equivalent to a χ^2 of $2\beta n$. We have constructed the posterior distribution reflecting the credibility of $f(v)$ as the dark matter velocity distribution explaining the observed recoil rate in one (or more) direct detection experiments, given a dark matter particle mass m_{DM} , a cross section σ_{DM} , and the strength of our prior β . The approach now will be to maximize the posterior for any velocity distribution $f(v)$ expressed as a superposition of streams, like we did in equation 83, given constraints on the observed rate of the direct detection experiments not yet considered in the posterior. Formally, our optimization problem takes the form,

$$\textbf{Maximize:} \quad -\beta D_{KL}(f_{MB}, f) - \frac{1}{2}\chi^2[f]^{(\alpha)}, \quad \alpha = 1, \dots, p \quad (123)$$

subject to:

$$\sum_{i=1}^n c_{\vec{v}_i} = 1$$

$$R^{(\alpha)}(c_{\vec{v}_1}, \dots, c_{\vec{v}_n}) \leq N_{obs}^{(\alpha)}, \quad \alpha = p+1, \dots, q$$

$$c_{\vec{v}_i} \geq 0$$

where we maximize the logarithm of the posterior in equation 122 and where the objective is convex (*KL-divergence* belonging to the exponential cone, and χ^2 quadratic on the weights $c_{\vec{v}_i}$, see section 5.2). The index α goes from 0 to p experiments, whose recoil rates will be used as a penalisation factor for those velocity distributions producing rates that deviate from the measured number of events by those experiments, and from $p+1$ to q for those experimental constraints that we will choose to be strict, that is, not as a penalisation factor in the objective function but constraints that must be strictly fulfilled by the optimized velocity distribution. The input in this optimization problem is the dark matter mass m_{DM} , the dark matter cross section σ_{DM} and the confidence in our prior β . Therefore, we can compute, for a given dark matter mass, cross section and strength of prior β , the maximally entropic velocity distribution that respects the experimental constraints from a given number of dark matter experiments. To be precise, the experimental constraints $\alpha = 1, \dots, p$ are allowed to be violated for sufficiently large confidence in our prior β , but will be respected when this value is small. If no strict constraints are considered, $q = p$, this method allows to interpolate between the Maxwell-Boltzmann prior $f_{MB}(\vec{v})$, and the best velocity distribution χ^2 fit to a certain number of experiments p , constructing maximally entropic velocity distributions among those extreme results.

6.2 Extracting information of the DM velocity distribution from CRESST III

We will apply the discussed methodology to the CRESST III experiment. In particular, we will solve the convex optimization problem 123, where we will consider one single experiment $p = 1$, CRESST III, accounting for the χ^2 factor in the objective function. The philosophy of our approach is schematized in Figure 27

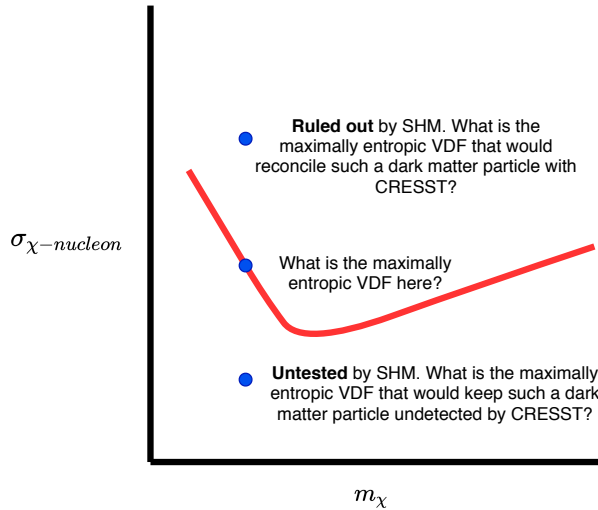


Figure 27: Philosophy of our approach. VDF refers to Velocity Distribution Function.

First, let's look at the performance of our approach for two points in the parameter space: Ruled out by CRESST III, see left plot of Figure 28, and a point not yet proved, see Figure

right plot of Figure 28. We notice that, for a point already ruled out of the parameter space, our reconstructed velocity distributions are naturally more conservative than the Maxwell-Boltzmann velocity distribution, in order to escape the CRESST constraint penalising the objective function. For small values of β , our velocity distributions highly weight the region below CRESST velocity spectrum. As it was expected, for sufficiently high values of β , that is, high confidence in our prior, the reconstructed velocity distributions approach the SHM form. Analogously, for points of the parameter space not yet probed by CRESST, the reconstructed velocity distributions are more aggressive than the Maxwell-Boltzmann, approaching a single stream at the escape velocity of the Milky way. As one increases the value of β , the SHM shape is recovered.

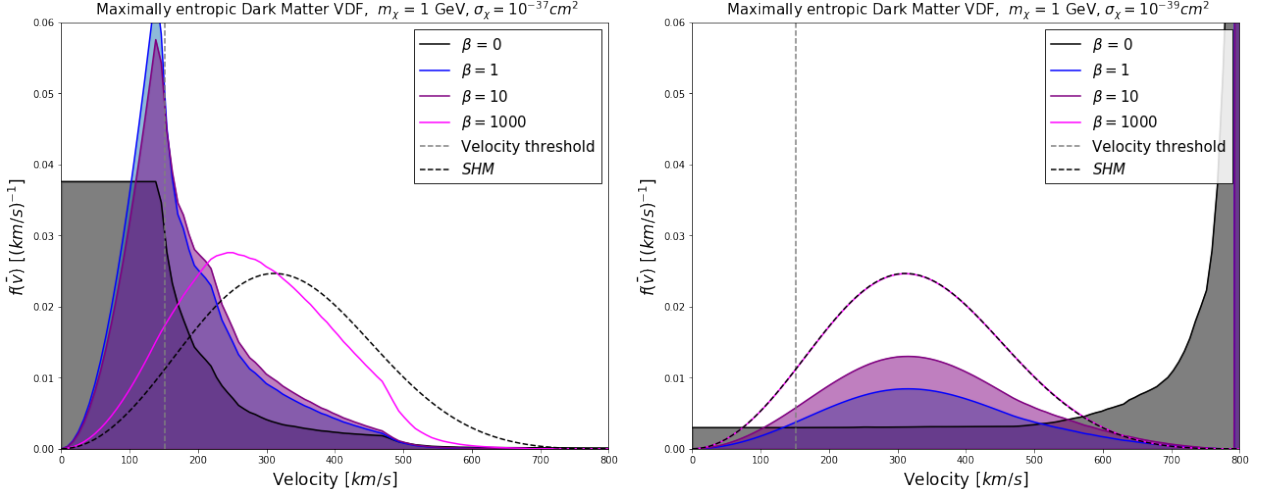


Figure 28: Maximally entropic reconstructed velocity distributions obtained with the *quantified maximum entropy* method, for different values of confidence in our prior β , and a dark matter mass of 1 GeV and cross section of 10^{-37}cm^2 (left) and 10^{-38}cm^2 (right). The CRESST III kinematical velocity threshold for such a dark matter particles is shown in dotted grey.

We are particularly interested in those points of the parameter space corresponding to upper limits provided by collaborations, corresponding to the extreme dark matter parameter configurations that experiments are able to test. In Figure 29 we show our results for different dark matter masses.

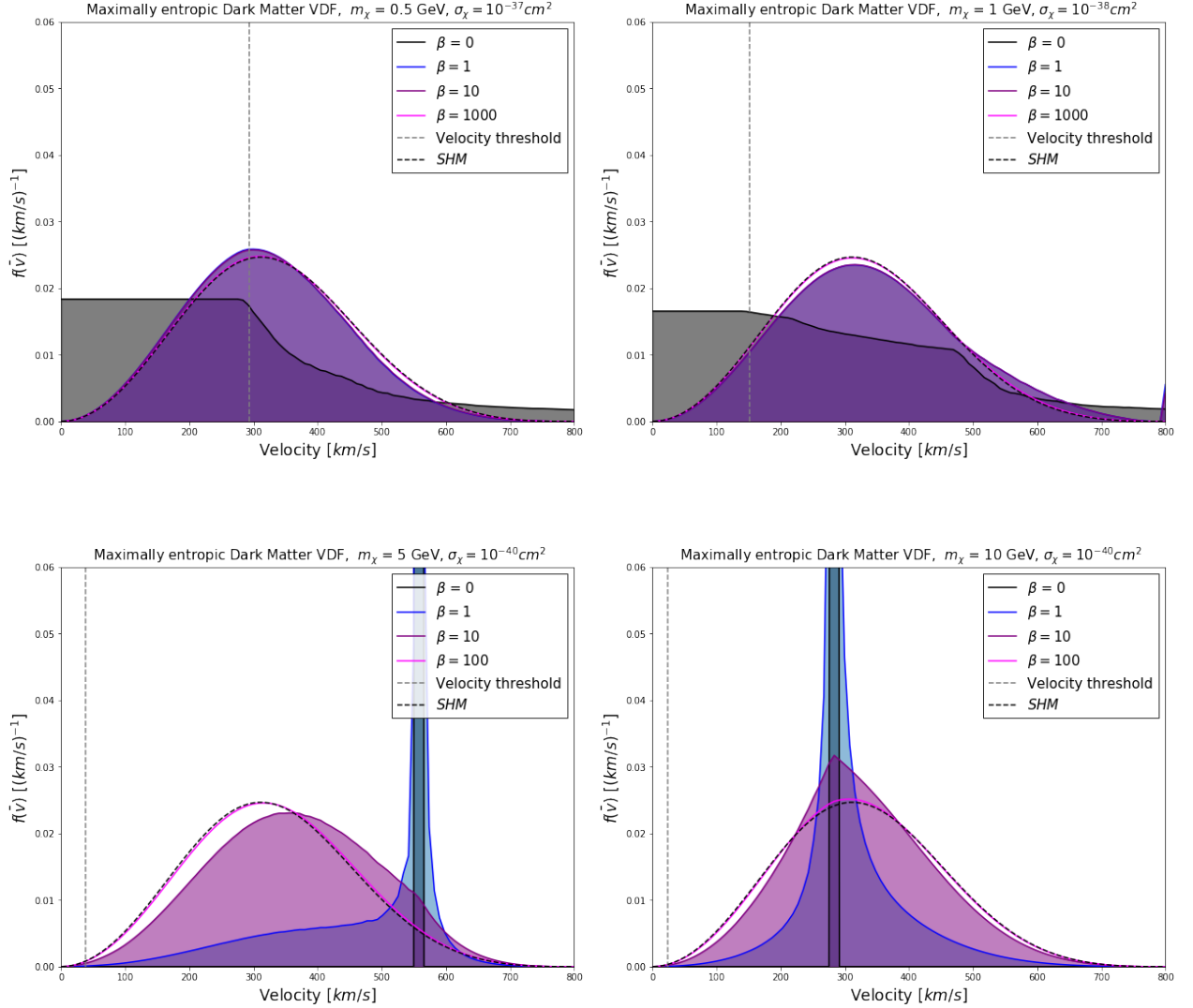


Figure 29: Maximally entropic reconstructed velocity distributions obtained with the *quantified maximum entropy* method, for different values of confidence in our prior β , and dark matter masses-cross section combinations corresponding to the CRESST III limit. The CRESST III kinematical velocity threshold for a such dark matter particles is shown in dotted grey.

We distinguish three scenarios according to the value of β :

- **$\beta = 0$, i.e, no confidence in the prior distribution:**

For sub-GeV Dark Matter, we obtain maximally entropic (uninformative) distributions, presenting a flat distribution up to the experimental velocity threshold, above which the probability distribution decays. The maximally entropic velocity distribution is by definition given by a equally weighted distribution (i.e a flat line in our plot), and the observed decay compensation is an artifact of the optimization problem constraints (positive and normalized distribution + χ^2 fit). For dark matter masses of 5 GeV and 10 GeV, the posterior distribution consists on a single stream. This result is very interesting since it indicates that the best χ^2 fit to CRESST observed number of

events is given by a stream of dark matter particles with a single velocity. A similar behaviour of the quantified maximum approach was observed in [124] when studying DAMA/LIBRA data.

- $\beta \in (0, 10]$, **i.e., "limited" confidence in the prior distribution:** For sub-GeV dark matter, we notice that for a small value of $\beta = 1$, which corresponds to a penalisation factor of $2n$ for each n deviation, we are close to completely recover the Maxwell-Boltzmann velocity distribution. For higher dark matter masses, larger values of the strength parameter β are necessary to obtain smoother distributions. From this sizable differences in the interpolation parameters it is possible to infer that the CRESST III observed number of dark matter events favours a Maxwell-Boltzmann-like velocity distribution for sub-GeV Dark Matter masses more "naturally" than it does as we move to higher dark matter masses.
- $\beta \rightarrow \infty$, **i.e., absolute confidence in the prior distribution:** We are able to recover the Maxwell-Boltzmann VDF for $\beta = 100$. No provided data from experiments can change the credibility of our prior. This sets an upper bound in the interpolation range that facilitates the interpretation of the results obtained for different dark matter masses.

We would like to emphasize that this work has been motivated by [124] and [148], but there are noticeable differences among them. In [124], the data used in the bayesian analysis is the DAMA/LIBRA dark matter signal with constraints in the modulated moments, while here we simply use the CRESST III observed dark matter rate (though we generalize to use further constraints from additional direct detection experiment or neutrino searches). We would like to point out a similar behaviour with [124] in the interpolated dark matter velocity distributions, though using completely independent data sets. For small values of β , both analysis favour a distribution consisting on a few streams, while at large β we recover the truncated Maxwell Boltzmann distribution. Still, there are some differences. For a Dark Matter mass of $m_\chi = 10$ GeV and $\sigma_\chi = 10^{-41} \text{cm}^2$, which falls inside the DAMA Island dark matter signal region, [105], our updated velocity distribution after consideration of CRESST III data favours a most probable speed of ~ 290 km/s, while [124] favours a most probable speed of ~ 360 km/s. The truncated Maxwell-Boltzmann velocity distribution presents an intermediate value of the most probable speed of ~ 320 km/s.

There is a caveat in the analysis [124] and [148] that we would like to comment, where a similar approach using XENON1T is used. DAMA/LIBRA can't access kinematically the whole dark matter velocity spectrum for the signal they observe at 10 GeV dark matter mass. XENON1T neither. The lack of information on the low velocity tail of the distribution makes very difficult to properly reconstruct the complete velocity distribution, since the only information in this region is given in the prior distribution. It is only for sufficiently heavy dark matter masses ~ 50 -100 GeV that these experiments are able to probe the whole spectrum. The advantage of this work is that CRESST is sensitive to a larger part of the velocity spectrum, even at sub-GeV masses, and provides a dark matter recoil spectrum consisting on a large number of events, though not interpreted as a signal because it is yet believed to be unknown background, [18]. There is still room for improvement, and the methodology

here proposed should include information about the recoil spectrum of CRESST, which is not equally distributed for each dark matter mass, see Appendix C for a discussion about this in the context of Poissonian statistics and the Yellin methods. Furthermore, information from further experiments should be included in the posterior. Nevertheless, in the case of a claim of dark matter by some experimental collaboration, this technique could be used to cross-check the feasibility of this signal with further experiments by looking precisely at the reconstructed dark matter velocity distribution which allows a signal at a certain experiment and a null results at others.

7 Alternative scenarios: Extragalactic dark matter and Inelastic dark matter

To conclude this thesis, we explore two scenarios that could also strongly affect the conclusions drawn from dark matter experiments. First, we will present the extragalactic dark matter contribution, which has been widely discussed in the context of indirect dark matter searches, [151][152], but not extensively in direct detection, [23], quantifying its impact in the upper limits of the CRESST III experiment. Later, we will consider the possibility that dark matter interacts inelastically with nuclei, deriving precise upper limits from CRESST II data, and comparing them with predictions and estimates from previous works, [24][143]. Finally, we will look at the 4 unidentified high recoil events observed at the CRESST II run, and sketch the impact that astrophysical uncertainties might have if interpreting such events as dark matter recoils.

7.1 Extragalactic dark matter at CRESST

A fraction of the dark matter particles detectable at Earth might not be bounded to the Milky Way, [153]. This fraction is small compared to the total local density of dark matter $\rho \sim 0.3 \text{ GeV}/\text{cm}^3$, but the large velocities of these particles $v \geq 500 \text{ km/s}$ could make their contribution significant to probe the low mass dark matter region of the parameter space in which most direct detection experiments lose sensitivity due to their energy threshold and minimum velocity required to produce such recoils. In this section we discuss the different extragalactic dark matter components that could yield a signal on Earth and calculate their impact in the CRESST experiment, whose sensitivity in the sub-GeV spectrum could be particularly affected by these contributions. There are two independent extragalactic dark matter contributions:

- **The Local Group**, consisting of two very massive galaxies (Milky Way and Andromeda galaxy M31), less massive Triangulum galaxy M33, and a host of dwarf galaxies, could contain a fraction of dark matter particles that is not bound in the galaxies, forming a large envelope that can penetrate the central region of our Galaxy and reach the solar system, [154]. Estimations in [23] show that this component is the of the order $\sim 10^{-2} \text{ GeV}/\text{cm}^3$.
- Extragalactic dark matter not belonging to the Local Group, in particular, **the diffuse component of the Virgo Supercluster**, in addition to galaxies and their groups, [153]. Measurements estimate the average of the diffuse component to be $\approx 10^{-5} \text{ GeV}/\text{cm}^3$

The dark matter envelope of the Local Group is modelled in [23] by an isotropic velocity distribution with small velocity dispersion $\sigma_v \approx 20 \text{ km/s}$, which would lead to a sharpened peak in the velocity distribution of dark matter particles near the Earth at velocities slightly higher than the escape velocity of the Galaxy, see Figure 30, that could dominate over the SHM-like component for the regions of the dark matter parameter space where experiment are only sensitive to the high velocity tail of the distribution. Regarding the supercluster dark matter particles, there is little knowledge about its velocity and space distributions. We assume that the dark matter particles have coherent velocities, comparable to the observed

velocity dispersions of the members of the supercluster, such that the velocity of dark matter particles at large distances from the earth is $v_\infty \sim 500$ km/s. The measurements estimate the average density of the diffuse component to be $\rho \approx 10^{-6}$ GeV/cm³, [153]. However, the gravitational field of the local group increases this quantity near the Earth. We can roughly estimate the enhancement as $1 + \frac{v_{esc}^2}{v_\infty^2}$. Taking the escape velocity of the solar system to be 544 km/s, the density of the supercluster dark matter particles is $\sim 10^{-5}$ GeV/cm³.

At a distance r from the center of the Milky Way, a dark matter particle has velocity $w(r) = \sqrt{v_\infty^2 + v_{esc}(r)^2}$. This yields velocities for the Virgo Supercluster dark matter particles at Earth to be ~ 740 km/s, which may produce high energetic recoils at direct detection experiments. Nevertheless, due to the low density of these extragalactic dark matter particles $\rho \approx 10^{-5}$ GeV/cm³, the expected scattering rate is very low.

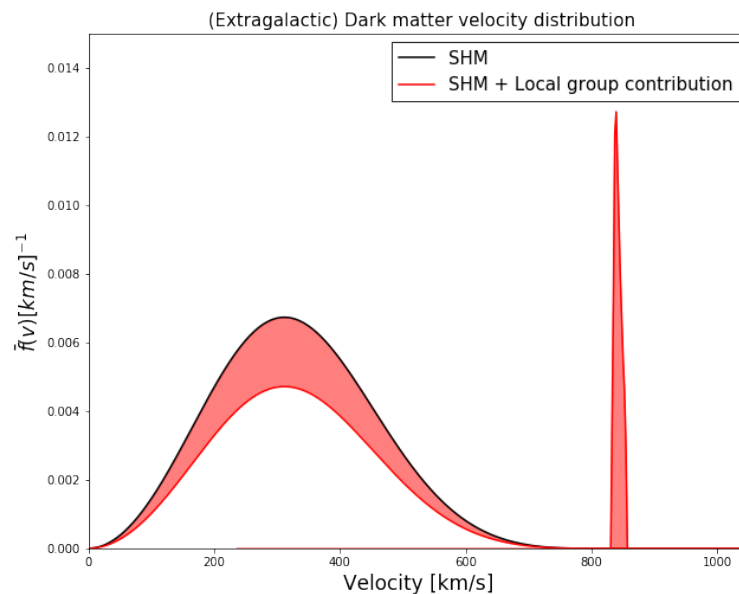


Figure 30: Normalized velocity distribution of dark matter particles at earth, according to [23], contrasted with the Maxwell-Boltzmann velocity distribution.

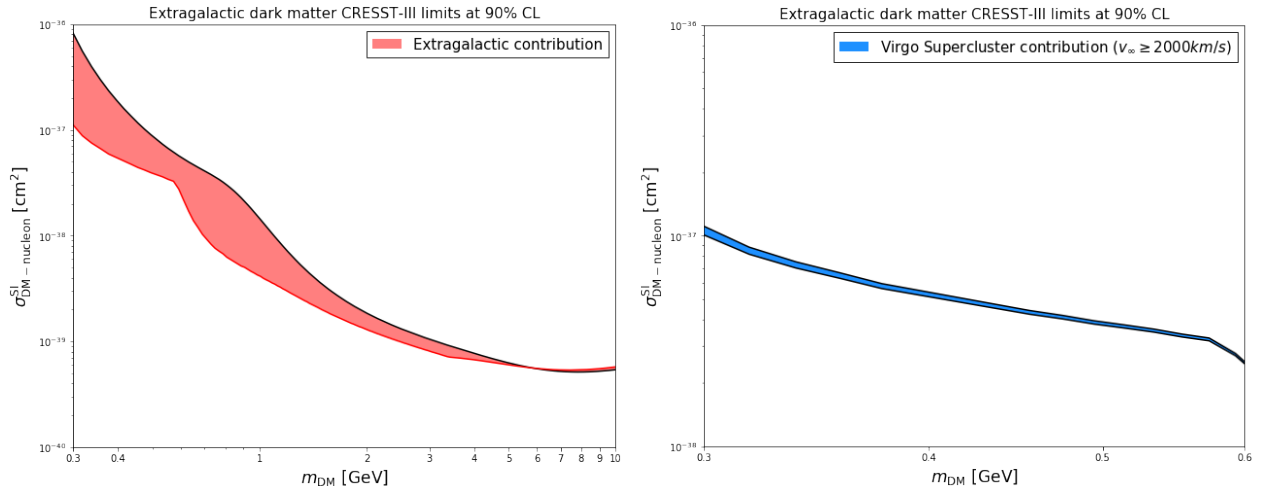


Figure 31: Impact of extragalactic component in CRESST III upper limits, from the Local Group contribution (left), and the diffuse component of the Virgo Supercluster (right), assuming for this case very large velocities of $v_\infty \sim 2000$ km/s

Our results are shown in Figure 31. The dark matter envelope of the Local Group would dominate the signal at CRESST III for masses below 5 GeV, causing uncertainties in the limits w.r.t the SHM limit of $\mathcal{O}(1)$. In the case of the diffuse component of the Virgo Supercluster, such high-speed dark matter particles do not affect the limits significantly, $\mathcal{O}(0.001)$ uncertainties. We conclude that the impact of the Local group component in the sensitivity of direct detection experiments in the elastic scattering scenario is small but sizable. If dark matter were made of light or sub-GeV particles, the extragalactic contribution may cause a signal on Earth that the Milky Way component wouldn't, therefore the study and determination of the precise shape and contribution of the extragalactic dark matter component from the Local Group is very important. In next section we will see indeed that in the case of inelastic dark matter this contribution could also dominate over the Standard Halo Model for sufficiently large mass splittings.

7.2 Inelastic dark matter at CRESST

We discussed in section 4.1 the possibility that dark matter scatters off inelastically with nuclei, accessing an excited state with mass splitting $\delta = m_{\chi_2} - m_{\chi_1}$. Inelastic dark matter has been suggested as a possible explanation for the DAMA dark matter signal, [155][156], and arises as a natural scenario in many dark matter particle models, [24][143][157]. Indeed, the inelastic kinematics provide scenarios in which dark matter particles would scatter in the DAMA Iodine detector ($A=127$) but not in other experiments with target nuclei of lower atomic number, such as CDMS, [106]. However, there is dedicated work to probe the incompatibility of the DAMA signal with other direct detection experiments, [55][158].

Regardless of its validity to explain the DAMA signal, inelastic scattering is a viable possibility that worths to be studied. If the state χ_2 is slightly heavier (\sim keV) than χ_1 , such that χ_1 can only scatter inelastically by making a transition to χ_2 , we have the following

kinematical constraint:

$$\delta c^2 < \frac{m_\chi m_N}{2(m_\chi + m_N)} v_\chi^2, \quad (124)$$

where δ is the mass splitting between χ_1 and χ_2 . It is straightforward to notice from equation 124 that heavier nuclei are able to test larger mass splitting values and thus we could encounter the situation in which some direct detection experiments are invisible to dark matter while others are not. As an example, if we take the largest possible velocity of a dark matter particle to be the Milky Way escape velocity (at the Galactic frame), $v_\chi = 544$ km/s, we see that the CRESST experiment (^{184}W) would satisfy the bound of 124 for mass splittings $\delta \leq 343$ keV. The PICO-60 and DAMA experiments containing Iodine, (^{127}I), require splittings of $\delta \leq 249$ keV. The CDMS experiment, ^{74}Ge , is blind to splittings larger than 151.2 keV. We could encounter an scenario in which a dark matter particle interacting inelastically with a sufficiently large mass splitting $\delta \sim 300$ keV would only be kinematically accesible to CRESST. In [143], it was suggested that 4 high energetic unidentified events at the CRESST II experiment, lying below the 5σ lower boundary of the electron/gamma band [17], could be produced by the inelastic scattering of heavy dark matter particles ~ 1 TeV, see Figure 34. Although these events are statistically incompatible with leakage, they are believed to be originated from unvetted α -decays, since the Lise detector module where these events were registered uses non-scintillating clamps and recoils happening on the surface are more difficult to distinguish. Additional data from further modules support this origin. Nevertheless, in the following we will consider these events as dark matter events, only with the purpose to show that a proper knowledge of the dark matter velocity distribution is crucial if one wants to make precise predictions, specially if dark matter scatters inelastically with nuclei.

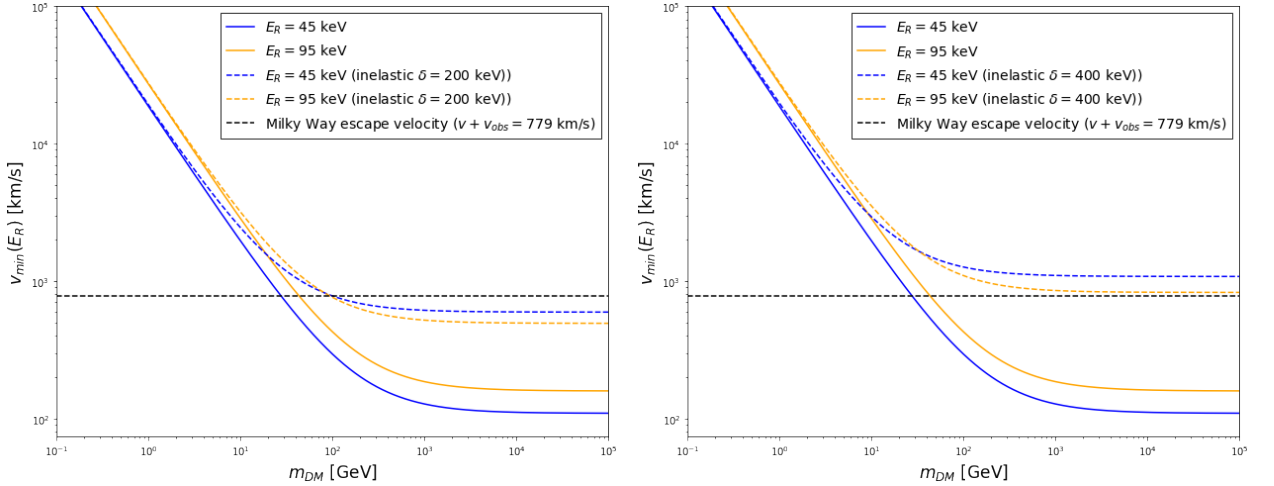


Figure 32: Minimum velocity necessary to produce recoils of 45 keV and 95 at tungsten, for different values of the dark matter mass, see equations 57 and 56. In dotted coloured lines we show the inelastic lower bound, and in solid lines the elastic case. In dotted black lines we show the Milky Way escape velocity at the Earth frame. On the left we consider a mass splitting of $\delta = 200$ keV, and on the right a value of $\delta = 400$ keV.

In Figure 32, we show the lower bound on the velocity that dark matter particles need to have in order to produce the lowest (45 keV) and the highest (95 keV) energy recoils from

the 4 unidentified events registered at CRESST II. We can appreciate that a mass splitting of 200 keV could only explain the CRESST results for dark matter particles having velocities close to the escape velocity of the Milky Way. For a dark matter mass splitting of 400 keV, this is not even possible. We can use the CRESST II data to constrain the parameter space of inelastic dark matter. Equation 46 for DM-induced elastic scattering rate in an element i is modified in the inelastic, spin-independent case as

$$\frac{dR_i}{dE_R} = \frac{\xi_i m_N \rho_{loc} \sigma_{p,n}}{2 m_{DM} \mu_{p,n}^2} \left(\frac{f^p Z + f^n (A - Z)}{f^n} \right)^2 F^2(E_R) \bar{\eta}(v_{min}) \quad (125)$$

$$\bar{\eta}(v_{min}) = \int_{v \geq v_{min}(E_R)} dv \frac{f(v)}{v} = \frac{\text{erf}(x_{min} + v_e/v_0) - \text{erf}(x_{min} - v_e/v_0)}{v_e} \quad (126)$$

where $v_0 = 220$ km/s, $x_{min} = v_{min}/v_0$, $\bar{\eta}(v_{min})$ is the mean inverse speed of the Maxwell-Boltzmann velocity distribution, [24], and $v_{min}(E_R)$ in the inelastic case is given by equation 56. By using this scattering rate formula in our analysis, we can derive upper limits on the spin-independent dark matter mass splitting cross section, for a fixed dark matter mass, that we will choose to be $m_{DM} = 1$ TeV, see Figure 33.

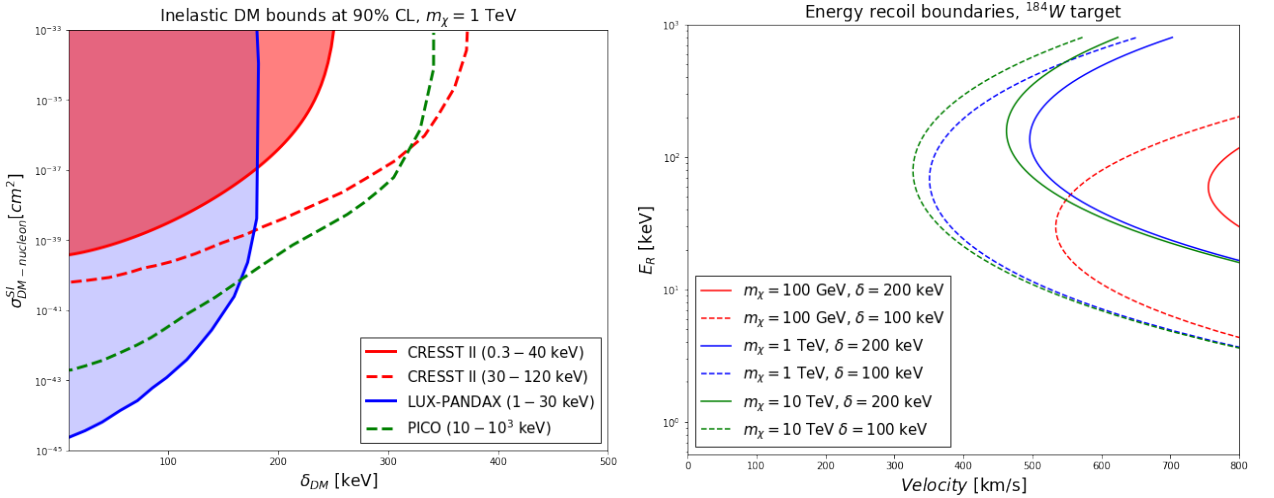


Figure 33: On the left, upper limits on the dark matter mass splitting δ -spin independent cross section on shaded colours for CRESST II, derived in this work, and the combination LUX-PandaX, taken from [143]. The dotted lines correspond to projections, or rough estimates, that consider energy ranges larger than actually analysed and published ones by CRESST II and PICO, probably not including the effect of target elements efficiencies, taken from [143]. On the right, the recoil energy boundaries according to equation 57, derived in section 4.1, for different values of the dark matter mass m_χ and mass splitting δ .

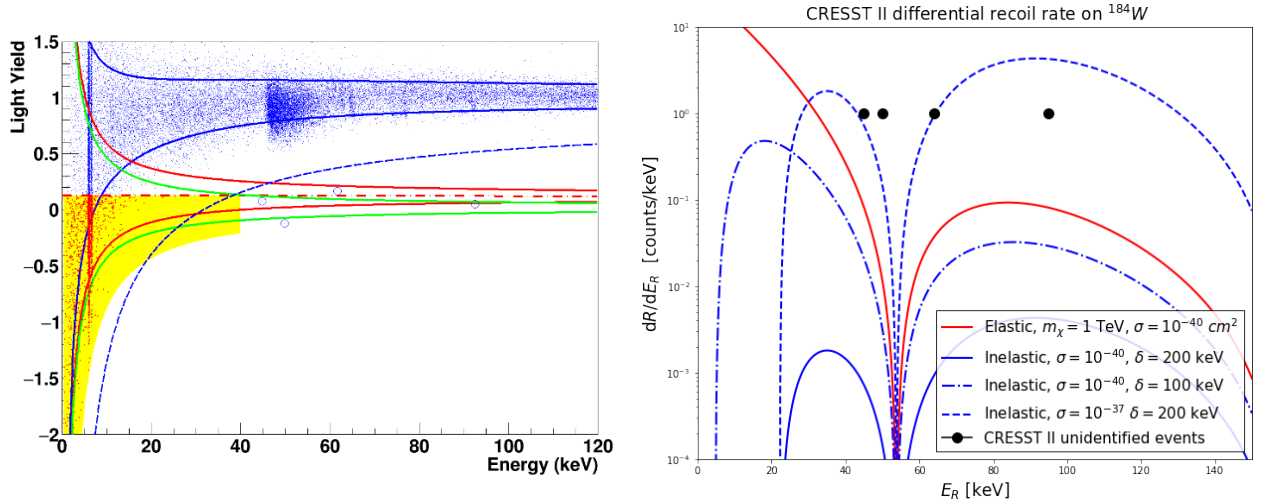


Figure 34: On the right, the light yield vs energy plane data taken at CRESST II, [17]. The solid lines mark the 90% upper and lower boundaries of the electron-gamma band (blue), the band for recoils off oxygen (red) and off tungsten (green). 4 events marked in blue circles are below the 5σ band. On the right, the expected differential recoil rate at CRESST for a dark matter particle of 1 TeV and different combinations of scattering type, dark matter cross section and mass splitting. The 4 unidentified events observed by CRESST are marked in black dots.

We notice that CRESST is able to rule out mass splittings $\delta \leq 200\text{-}270$ keV for dark matter cross sections greater than $10^{-37}\text{-}10^{-35}\text{cm}^2$. Projected limits for a larger energy range consideration from [143] will allow CRESST to test mass splittings as large as 400 keV. LUX-PandaX constraints are stronger than CRESST at low mass splittings, being able to rule out inelastic dark matter up to 180 keV for cross sections larger than 10^{-41}cm^2 . There is a large region of the parameter space which is yet untested. In Figure 34, some differential rates are calculated for different dark matter mass-cross section configurations. We notice that the 4 unidentified events from CRESST II lie close to a form factor suppressed region $E_R = 55$ keV, therefore being the event at 50 keV very problematic to explain with both elastic and inelastic scattering predictions. Furthermore, it is argued in [143] that a inelastic 1 TeV dark matter particle of mass splitting $\delta = 200$ keV and cross section $\delta = 10^{-39}\text{cm}^2$ could be in tension with PICO results, [109], although the energy range considered in this article is larger by one order of magnitude than published PICO data. We therefore treat this bound with precaution.

How would this discussion change if the dark matter velocity distribution were different from the SHM? In Figure 35 we calculate the differential scattering rates at CRESST II when considering the extragalactic dark matter contribution to the velocity distribution of dark matter particles near the Earth discussed in previous section 7.1.

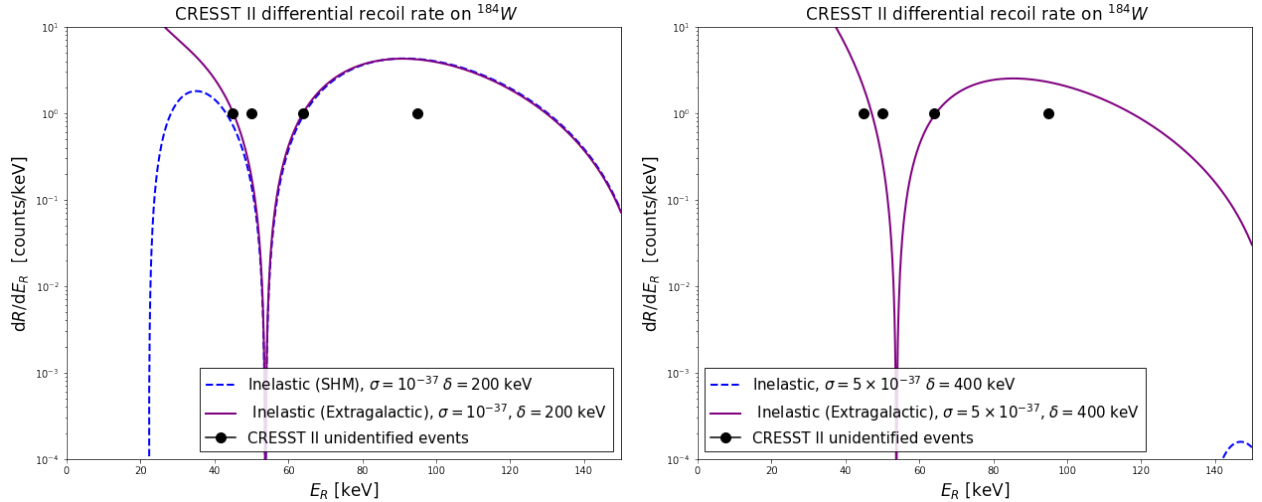


Figure 35: Expected differential recoil rates at CRESST II for a dark matter velocity distribution consisting in a mixture of the SHM and the extragalactic high velocity narrow peak coming from the Local Group dark matter envelope. On the left we show the rates for a dark matter mass splitting of 200 keV and on the right for a mass splitting of 400 keV.

We appreciate that due to the high velocity of the extragalactic dark matter particles, mass splittings of $\delta = 400$ keV are now accessible to CRESST, while for the SHM velocity distributions the rates were completely suppressed. For a mass splitting of 200 keV we notice a slightly better matching of the event occurred at 45 keV. This is only a qualitative study, and a proper analysis must include astrophysical and nuclear (from the Helm form factor) uncertainties in the differential rates, further calculating the significance of these events according to predictions of the differential dark matter inelastic recoil spectrum. We do not propose here that a dark matter particle with a mass of 1 TeV and a cross section in the range 10^{-37} - 10^{-40} with mass splittings $\delta \geq 200$ keV interacting inelastically, with a dark matter velocity distribution including the extragalactic components, is an explanation for these 4 events. Nevertheless, what is clear from the previous discussion is that the extragalactic dark matter component could lead to measurable differences in dark matter signatures w.r.t the SHM, and that a proper knowledge of the dark matter velocity distribution is crucial to make high precision predictions. Such a dark matter particle should furthermore be accessible kinematically to Xenon and Iodine based experiments. Nevertheless, current inelastic bounds shown in Figure 33 do not rule out this possibility. It would be in tension with PICO-60 null results, but we remark again that the bound shown in [143] corresponds to an energy range larger than the one described in the collaboration paper [109], and thus we cannot conclude that such a bound is sufficiently solid statistically as it was not performed by the collaboration, and the recoil efficiencies in the range 100-1000 keV are not available.

8 Conclusions

The dark matter velocity distribution in the solar neighbourhood is unknown. In this thesis, we have proposed a novel method to calculate the dark matter velocity distribution based in the principle of maximum entropy, from a set of initial prior assumptions. We have shown that our method and the rest of techniques available in the literature to obtain the dark matter velocity distribution present incompatibilities. We conclude that the Standard Halo Model (SHM) used at experiments might not be a correct description of our dark matter halo, and that deviations from this model need to be considered in order to make precise predictions at direct detection and indirect dark matter searches. We have described the formalism of direct detection and neutrino experiments searching for annihilation of dark matter particles in the Sun, emphasizing the relevance of the dark matter scattering kinematics. Based in this discussion and the work [121], we have developed a method to quantify the impact of astrophysical uncertainties in a direct detection experiment, based on tools from information theory. By using this technique, we have derived upper limits on the dark matter scattering cross-section using CRESST III data, including uncertainties from the velocity distribution. Being conservative, we find $\mathcal{O}(1)$ uncertainties in CRESST upper limits for both spin-independent and spin-dependent cases. Furthermore, we use our methodology to study the impact of astrophysical uncertainties when interpreting direct detection bounds on specific dark matter models. In addition, we perform a halo-independent analysis of CRESST and Super-Kamiokande, finding upper limits up to 1 order of magnitude more conservative than Super-Kamiokande bounds. Our spin-independent halo-independent limit is competitive with respect to previous studies in the range 4-10 GeV.

We also propose a different approach, motivated by [124], and based in the quantified maximum entropy method, that allows to interpolate between the maximally entropic and the Maxwell-Boltzmann velocity distributions under restrictions on upper limits coming from direct detection searches. We apply this methodology to the CRESST III experiment, discussing that this method could be used to cross-check a positive signal of a certain direct detection experiment, with the null results obtained at other experiments, by studying the velocity distributions that could satisfy all results simultaneously. Finally, we discuss the impact that the extragalactic dark matter contribution could cause on direct detection experiments, and the importance of having a proper knowledge of the dark matter phase space distribution to interpret a signal, if dark matter scatters inelastically with nuclei.

A Appendix A

A.1 Convex Optimization

This appendix is dedicated to discuss basic theoretical aspects of convex optimization and the main algorithms used along this thesis, following the notation of [131][159]. We have mostly used the programming language Python, and the public available code **CVXPY**, [119], which allows for a simple formulation of the optimization problems of interest, making use of disciplined convex programming, [160], and which includes several optimization packages with different functionalities such as **ECOS**, **CVXOPT** and **OSQL**, [130]. Most of the work here has been performed under the **ECOS** software, which is based in primal-dual path following algorithms. These are briefly discussed in A.6.

A convex optimization problem has the form

$$\text{Minimize: } f_0(x) \tag{127}$$

subject to:

$$f_i(x) \leq 0, \quad i = 1, \dots, m$$

$$a_j^T x = b_j, \quad j = 1, \dots, p$$

where f_0, \dots, f_m are convex functions, i.e, they are defined in a convex set $C \subset \mathbb{R}^n$, such that $f_0(x), f_i(x) : C \rightarrow \mathbb{R}$, and and if for all $x, y \in C$, and θ with $0 \leq \theta \leq 1$, the following condition is fulfilled:

$$f(\theta x + (1 - \theta)y) \leq \theta f(x) + (1 - \theta)f(y) \tag{128}$$

The problem 143 is said to be in the **standard form**. Alternative representations in terms of **generalized inequalities** are also possible, see [131].The function to optimize f_0 is called the *objective function* and the conditions to which is subject f_i, a_i are the *inequality constraints* and *equality constraints*, respectively. These define the *feasible set*, which is the set $x \in C$ that fulfills all constraints. If there is any local (global) optima for the problem, it belongs to this set. A fundamental property of convex optimization problems is that any locally optimal point is also (globally) optimal. A short and nice proof can be found in [131]. We do not extend further here for simplicity.

A.2 The Karush-Kuhn-Tucker optimality conditions

The Karush-Kuhn-Tucker (KKT) conditions are first-order necessary conditions for a solution of a non linear problem to be optimal, provided that some *regularity* conditions are satisfied. They are applicable to both convex and non-convex problems, though here we will assume only convex problems in the form of 143. The KKT conditions generalize the Lagrange multipliers method, which is only valid for problems with equality constraints, to problems including inequality constraints.

Given a non-linear convex problem in the standard form 143, being the objective function $f_0 : \mathbb{R}^n \rightarrow \mathbb{R}$ and constraints $f_i : \mathbb{R}^n \rightarrow \mathbb{R}, a_j : \mathbb{R}^n \rightarrow \mathbb{R}$ continuously differentiable at a point x^* . If x^* is a local optimum and the optimization problem satisfies some regularity conditions (they are not exposed in this appendix, we refer to [131] for a detailed description of them), then there exist constants μ_i ($i = 1, \dots, m$), λ_j ($j = 1, \dots, \ell$), called KKT multipliers, such that the following four groups of conditions hold:

- **Stationarity**

$$\nabla f_0(x^*) \pm \sum_{i=1}^m \mu_i \nabla g_i(x^*) \pm \sum_{j=1}^{\ell} \lambda_j \nabla a_j(x^*) = 0 \quad (129)$$

where the plus or minus is chosen whether we want to minimize or maximize the objective function, respectively.

- **Primal feasibility**

$$g_i(x^*) \leq 0, \quad i = 1, \dots, m \quad (130)$$

$$h_j(x^*) = 0, \quad i = 1, \dots, \ell \quad (131)$$

- **Dual feasibility**

$$\mu_i \geq 0, \quad i = 1, \dots, m \quad (132)$$

- **Complementary slackness**

$$\mu_i g_i(x^*) = 0, \quad i = 1, \dots, m \quad (133)$$

A local/global (the sufficient conditions are more subtle and not discussed here, we refer to [131] for a complete description) optimal value for a certain problem can be therefore obtained by finding the optimal values of the lagrangian $\mathcal{L}(x, \mu, \lambda)$. For the special case of $m = 0$, i.e, no inequality constraints, the KKT multipliers reduce to the usual Lagrange multipliers.

In section 2.2.4 we have used the KKT conditions analytically to find the maximally entropic VDF that respects some certain well motivated physical constraints. The KKT conditions have also been indirectly used in the computation of all halo-independent limits shown in this work, since they belong to the skeleton of all the optimization algorithms and packages that we have made used of.

A.3 Linear programming

Linear programs (LPs) are the simplest convex optimization problems, characterised by being affine both objective function and constraints. It reads

$$\text{Minimize: } c^T x \tag{134}$$

subject to:

$$Gx \leq h$$

$$Ax = b$$

where the vectors $c \in \mathbb{R}^n$, $h \in \mathbb{R}^m$, $b \in \mathbb{R}^p$ and the matrices $G \in \mathbb{R}^{m \times n}$, $A \in \mathbb{R}^{p \times n}$. Linear programs are usually written in their **standard form**. Transforming some problem to the standard form is necessary, for example, in order to use an algorithm for standard form LPs. Any problem which is not in the standard form can be transformed to this, in the case of unrestricted primal variables, by writing a general primal variable z_i as the difference of two non-negative primal variables, i.e. $z_i = x_i - y_i$, so that the primal variables x_i are non-negative in the standard form. Inequality constraints must be written as equality constraints as well, and this is achieved by introducing m slack variables s_i . Combining primal and slack variables into one vector $y = (x_1, \dots, x_n, s_1, \dots, s_m)$, the LP A.3 can be transformed into the standard form:

$$\text{Minimize: } c^T x \tag{135}$$

subject to:

$$Ay = b$$

$$x \geq 0$$

where A is now a $(m+p) \times (n+m)$ matrix. It is important to note that the non-negativeness of the primal variables is not considered as an inequality constraint. It is possible to show, [131], that the rows a_i of the matrix A must be linearly independent for the optimal solutions of the problem $p^* \in \mathbb{R}^{n+m}$ that belong to the set $a_i | Ap^* = b, b_i^* \neq 0$. As a $i \times j$ matrix can have at most $\min(i, j)$ linearly independent rows, we conclude that there are exactly $\min(n+m, m+p)$ entries of p^* that are larger than zero. As there are m slack variables that could be larger than zero, the number of positive primal variables is given by

$$\min\{m+n, p+n\} - k \leq \text{Number of } x_i \neq 0 \leq \min\{m+n, p+n\} \tag{136}$$

In common problems, the number of primal variables n is much larger than the number of constraints, which implies

$$p \leq \text{Number of } x_i \neq 0 \leq p+m \tag{137}$$

Therefore, the number of positive primal variables is at least equal to the number of equality constraints and can be as large as the total number of constraints. This observation is especially useful to get analytic insight into the solutions that have been obtained during this work, and for some objective functions, this can be used to determine the solution. This is particularly useful in reference to the number of dark matter streams that we are able to compute for the completely halo-independent analysis, as it has been discussed in section 5.1.

A.4 Second Order Cone Problems (SOCP)

Along this thesis, most problems discussed were solved in the form of Second order cone problems (SOCP). Before discussing this specific class of optimization problems, it is necessary to introduce the concept of *cone* and *generalized inequalities*.

A convex set K is called a convex *cone*, if for every $x_1, x_2 \in K$ and $\theta_1, \theta_2 \geq 0$, we have

$$\theta_1 x_1 + \theta_2 x_2 \in K \quad (138)$$

A *proper cone* $K \subset \mathbb{R}^n$ is a convex cone that satisfies the additional following conditions:

- K is closed (i.e its complementary set is open, it contains all its limit points..)
- K is *solid* (i.e its interior set is non-empty)
- K is *pointed*, which means that it contains no line (i.e $x \in K, x \in K \Rightarrow x = 0$)

Proper cones K are used to define *generalized inequalities*, which is a partial ordering on \mathbb{R}^n , and can be interpreted as a generalization to the standard ordering in \mathbb{R} . This partial ordering in proper cones is defined as

$$x \preceq_K y \Leftrightarrow y - x \in K \quad (139)$$

A strict partial ordering is defined as

$$x \prec_K y \Leftrightarrow y - x \in \text{int}K \quad (140)$$

Where $\text{int}K$ is the interior set of K . When $K = \mathbb{R}_+$, the partial ordering \preceq_K is the usual ordering \geq on \mathbb{R} , and the strict partial ordering \prec_K is the same as the usual strict ordering $<$ on \mathbb{R} . So generalized inequalities include as a special case ordinary (nonstrict and strict) inequality in \mathbb{R} .

The simplest example of a proper cone is the non-negative orthant \mathbb{R}_+^n , as it can be seen from conditions A.4. It can be straightforwardly seen, that the partial ordering $x \preceq_{\mathbb{R}_+^n} y$ are just component-wise inequalities of the vectors x and y , i.e. $x_i \leq y_i$ which can be written as matrix-vector inequality $Gx \leq h$.

We have now the necessary ingredients to introduce the example of *second order cones* \mathcal{Q}^n , [55],

$$\mathcal{Q}^n := \{(x, t) \in \mathcal{R}_+^n | t \gg \|x\|_2\}, \quad (141)$$

where $\|x\|_2$ denotes the Euclidean norm. Let's prove that \mathcal{Q}^n is a proper cone. First, we notice that it is convex. Being $\theta \in [0, 1]$ and $(t_1, x), (t_2, y) \in \mathcal{Q}^n$, we have

$$\|\theta x + (1 - \theta)y\|_2 \leq \theta\|x\|_2 + (1 - \theta)\|y\|_2 \leq \theta t_1 + (1 - \theta)t_2 \quad (142)$$

where we have used that the Euclidean norm is subadditive and absolutely homogeneous. We notice also that \mathcal{Q}^n is a closed and solid set, [55]. Furthermore, the second order cone is pointed as the only vector for which both x and x are in \mathcal{Q}^n is the vector consisting of only zeros.

Now we can define the standard form of second order cone optimization problems (SOCP). They are defined as

$$\text{Minimize: } c^T x \quad (143)$$

subject to:

$$\|G_i x + d_i\|_2 \leq e_i^T x + h_i, \quad i = 1, \dots, m$$

$$Ax = b$$

where we see that the variables $(G_i x + d_i, e_i^T x + h_i)$ should belong to a second-order cone \mathcal{Q}^m .

A.5 Exponential Cone Problems

Many optimization problems can contain exponentials and logarithms. These can sometimes be modelled with the exponential cone, which is a convex subset of \mathbb{R}^3 defined as

$$K_{\text{exp}} = \{(x_1, x_2, x_3) : x_1 \geq x_2 e^{x_3/x_2}, x_2 > 0\} \cup \{(x_1, 0, x_3) : x_1 \geq 0, x_3 \leq 0\} \quad (144)$$

Thus the exponential cone is the closure in \mathbb{R}^3 of the set of points which satisfy

$$x_1 \geq x_2 e^{x_3/x_2}, x_1, x_2 > 0 \quad (145)$$

When working with logarithms, as in the case of the KL-divergence, equation 145 can be rewritten as

$$x_3 \leq x_2 \log(x_1/x_2), x_1, x_2 > 0 \quad (146)$$

Alternatively, it can be written as

$$x_1/x_2 \geq e^{x_3/x_2}, x_1, x_2 > 0 \quad (147)$$

This shows that K_{exp} is a cone, i.e. $\alpha x \in K_{\text{exp}}$ for $x \in K_{\text{exp}}$ and $\alpha \geq 0$. The convexity of K_{exp} follows from the fact that the Hessian of $f(x, y) = y \exp(x/y)$ is positive,

$$D^2(f) = e^{x/y} \begin{bmatrix} y^{-1} & -xy^{-2} \\ -xy^{-2} & x^2 y^{-3} \end{bmatrix}$$

is positive semidefinite for $y > 0$, [161]

A.6 Interior-point methods

The main algorithms used for solving convex optimization problems that include inequality constraints are the so-called *interior-point methods*. Along this work, we have made use of them within the **CVXPY** package, in particular when using the *embedded conic solver ECOS* for second order cone problems (SOCP). Formally,

$$\text{Minimize: } f_0(x) \tag{148}$$

subject to:

$$f_i(x) \leq 0, \quad i = 1, \dots, m$$

$$Ax = b$$

where $f_0, \dots, f_m : \mathbf{R}^n \rightarrow \mathbf{R}$ are convex and twice continuously differentiable, and $A \in \mathbf{R}^{p \times n}$ with rank $A = p < n$. We assume that the problem is solvable and strictly feasible, [131]. Interior-point methods solve the problem using a *barrier function* to reduce the problem 148 to a series of linear equality constrained problems, each approximately solved by Newton's method. The idea of the barrier function is to make the inequality constraints implicit in the objective:

$$\text{Minimize: } f_0(x) + \sum_{i=1}^m -(1/t)\log(-f_i(x)) \tag{149}$$

subject to:

$$Ax = b$$

where $t > 0$ is a parameter that sets the accuracy of the approximation. The larger the value of t , the more accurate is the approximation. The objective here is convex, since $-(1/t)\log(-u)$ is convex and increasing in u , and differentiable. The barrier function

$$\phi(x) = - \sum_{i=1}^m \log(-f_i(x)) \tag{150}$$

has domain $\text{dom}\phi = \{x \in \mathbf{R}^{p \times n} | f_i(x) \leq 0, i = 1, \dots, m\}$, which is the set of points that satisfy the inequality constraints of 148 strictly. The problem 149 is just an approximation of the original problem, and the quality of the approximation improves as the parameter t grows. On the other hand, when t is too large, the objective function is difficult to minimize by Newton's method, since its Hessian varies rapidly near the boundary of the feasible set. This problem is circumvented by solving a sequence of problems of the form 151, increasing t at each step, and starting each Newton minimization at the solution of the problem for the previous value of t , thereby by a sequence,

$$\chi^{k+1} = \chi^k - \chi^k \Delta \chi^k, \quad k = 0, 1, 2, \dots \tag{151}$$

with $\chi^k = (x^k, y^k, s^k, z^k)$, being x and y the optimized variables of the primal and dual problems, respectively, and s and z the slack variables associated to its inequality constraints. Δ^k yields a particular search direction found by solving one or more linear systems, and $\alpha^k > 0$ is a step length found by line search, [130].

In path-following algorithms, iterates 151 loosely track the *central path*. Assuming that the problem 149 is solvable by Newton's method, and that for each $t > 0$ there is a unique solution $x^*(t)$, [131], the central path points are characterized by the following necessary and sufficient conditions:

- $x^*(t)$ is strictly feasible, i.e, satisfies $Ax^*(t) = b, f_i(x^*(t)) \leq 0, i = 1, \dots, m$
- There exists a $\bar{\nu} \in \mathbf{R}$ s.t

$$0 = t\nabla f_0(x^*(t)) + \nabla\phi(x^*(t)) + A^T\bar{\nu} = t\nabla f_0(x^*(t)) + \sum_{i=1}^m \frac{1}{-f_i(x^*(t))} \nabla f_i(x^*(t)) + A^T\bar{\nu} \quad (152)$$

holds

We can give a simple geometric interpretation of the centrality condition for the case of a *inequality form linear programming*, i.e an optimization problem with only linear inequality constraints, but not equality ones. At a point $x^*(t)$ on the central path the gradient $\nabla\phi(x^*(t))$, which is normal to the level set of ϕ through $x^*(t)$, must be parallel to c . In other words, the hyperplane $c^T x = c^T x^*(t)$ is tangent to the level set of ϕ through $x^*(t)$. An example is presented in figure 36.

From the second condition listed, every central point yields a dual feasible point, and hence a lower bound on the optimal value p^* . Concretely, define

$$\lambda_i^*(t) = -\frac{1}{tf_i(x^*(t))}, i = 1, \dots, m, \nu^*(t) = \bar{\nu}/t \quad (153)$$

and claim that the pair $\lambda^*(t), \nu^*(t)$ is dual feasible.

Only the basic aspects common to all interior point methods have been presented here. In particular, most of the calculations performed during this thesis have primarily used *primal dual methods*, [130]. These are characterized by updating both primal and dual variables at each iteration, and the search direction $\Delta\chi^k$ is obtained from Newton's method, applied to the the modified KKT equations. For a detailed mathematical description of this and other interior point methods see [131][130] and references therein.

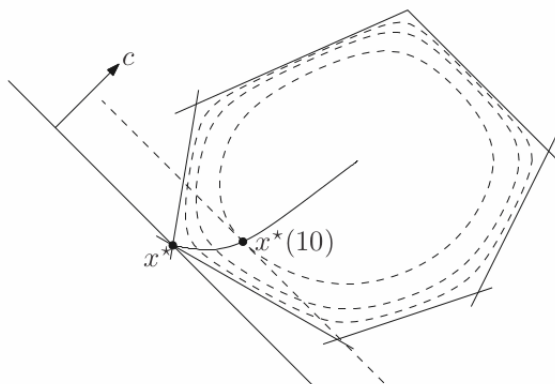


Figure 36: Central path for a linear problem with $n = 2$ and $m = 6$. The dashed curve show three contour lines of the logarithmic point x^* as $t \rightarrow \infty$. Also shown is the point on the central path with $t = 10$. The centrality condition 152 at this point can be verified geometrically: The line $c^T x = c^T x^*(10)$ is tangent to the contour line of ϕ through $x^*(10)$

A.7 Disciplined Convex Programming (DCP)

Disciplined convex programming (DCP) is a system for constructing mathematical expressions with known curvature from a given library of base functions and sets (*atoms*). The convex optimization package used in this thesis, CVXPY, [119], uses DCP to ensure that the specified optimization problems are convex. For this reason, we consider necessary to dedicate an specific appendix to discuss this methodology. Instead of constructing constraints and objective functions without an advance regard for convexity, DCP consists of an *atom library* of functions and sets, whose properties of shape (convex/concave/affine), monotonicity and range are explicately declared, and a *ruleset*, based on basic principles of convex analysis, that governs how atoms, variables, parameters and numeric values can be combined to produce convex results. The rules provide a set of sufficient conditions to guarantee that any problem constructed in accordance with the the ruleset is convex. Nevertheless, it could happen that a mathematical convex problem is not a valid DCP, so that they have to be rewritten to comply with the ruleset, or this itself and the atoms need to be enlarged. A concrete example of this is shown in Figure 37.

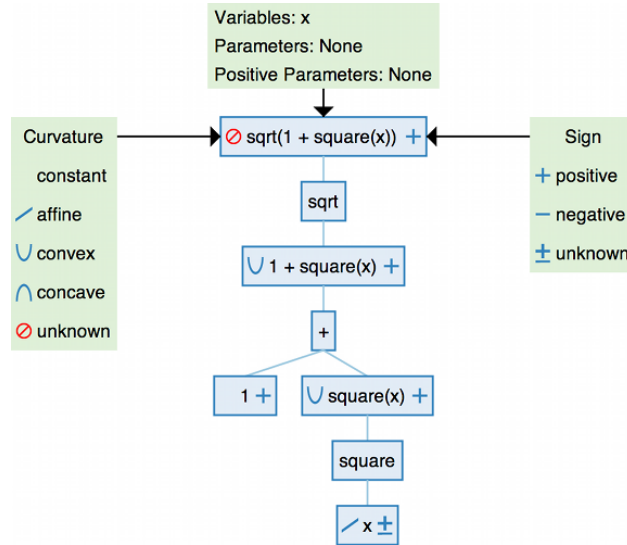


Figure 37: The variable x has affine curvature and unknown sign. The square function is convex and non-monotone for arguments of unknown sign. It can take the affine expression x as an argument; the result $square(x)$ is convex. The arithmetic operator $+$ is affine and increasing, so the composition $1 + square(x)$ is convex by the curvature rule for convex functions. The $sqrt$ function is concave and increasing, which means it can only take a concave argument. Since $1 + square(x)$ is convex, $sqrt(1 + square(x))$ violates the DCP rules and cannot be verified as convex. In fact, $sqrt(1 + square(x))$ is a convex function of x , but the DCP rules are not able to verify convexity. If the expression is written as $norm2(1, x)$, the L2 norm of the vector $[1, x]$, which has the same value as $sqrt(1 + square(x))$, then it will be certified as convex using the DCP rules, [160]

We will present a list of *top-level* rules, which will form the skeleton of any DCP. From these, further convex analysis knowledge can be applied to restrict the composition of functions. The extension and elements of the *atom library* also need to be discussed but we will omit this as it is out of the purpose of this work. For a more detailed treatment of the subject we remit the reader to [160].

Problem types:

- **T1** Minimization: convex objective and convex constraints
- **T2** Maximization: concave objective and convex constraints;
- **T3** Feasibility problem : no objective and one or more convex constraints.

Constraints:

- **T4** Equality constraint with affine-left and right-handed expressions
- **T5** Inequality of type $(<, \leq)$, with a convex left-hand expression and concave right-hand expression;

- **T6** Inequality of type ($>$, \geq), with concave left-hand expression and a convex right-hand expression;
- **T7** Set membership constraint $(lexp_1, \dots, lexp_m) \in cset$, where $m \geq 1$, $lexp_1, \dots, lexp_m$ are affine expressions, and $cset$ is a convex set.

$$\begin{array}{ll}
\text{affine} = \text{affine} & \text{(T4)} \\
\text{convex} \leq \text{concave} \text{ or } \text{convex} < \text{concave} & \text{(T5)} \\
\text{concave} \geq \text{convex} \text{ or } \text{concave} > \text{convex} & \text{(T6)} \\
(\text{affine}, \text{affine}, \dots, \text{affine}) \text{ in convex set} & \text{(T7)}
\end{array}$$

Figure 38: Valid constraints

Further top-level expressions refer to *constant expressions* and *assertions*. *Constant expressions* involve numeric values and/or problem parameters (**T8**), while *non-constant expressions* depend on the value of at least one problem variable, and *assertions* refer to constraints involving only constant expressions (like Boolean expressions, **T9**). Finally, if a function or set is parameterized, then those parameters must be valid constant expressions, **T10**.

B Appendix B

B.1 Introduction to Information theory

Information theory was originally formulated by Shannon (1948) as a theory of *communication*: specifically, the transmission of a signal of some given complexity over an unreliable channel, such as a telephone line corrupted by a certain amount of noise [19]. Nowadays, Information theory is understood within Probability theory. In particular, it emphasizes over some properties of probability distributions (more generally, of probability measures) that are independent of how those distributions are represented. The most fundamental of this properties is the *entropy*, formulated by Shannon based on the already known physical thermodynamical entropy. In Information theory, the *entropy* quantifies the amount of uncertainty involved in the value of a random variable or the outcome of a random process. Precisely, for a discrete probability distribution $P(X)$, it is defined as,

$$H(P) = - \sum_{x \in \mathcal{X}} P(x) \log_b P(x) \quad (154)$$

The logarithm of the probability distribution is useful as a measure of entropy because it is additive for independent events or sources. b is the base of the logarithm used, and it represents the units in which the information over the random variable is encoded. Some common values are:

- $b = 2 \rightarrow$ bits
- $b = e \rightarrow$ nats

- $b = 10 \rightarrow$ bans

In this thesis we have used natural logarithms ($b = e$). The fact that we are using natural logarithms is justified because we have dealt with physical processes and probability distributions based on thermodynamical assumptions, whose formulation is done using natural logarithms (to define the physical measurable quantities).

B.2 Proofs of theorems 1 and 2

Proof of theorem 1:

This proof is due to Pollard's [162].

We'll use this relation

$$(1+t)\log(1+t) - t \geq \frac{1}{2} \cdot \frac{t^2}{1+t/3}, \quad t \geq -1 \quad (155)$$

There is no loss of generality in assuming that

$$\sup_{x \in \mathcal{X}} \frac{p(x)}{q(x)} < \infty$$

since otherwise $D_{KL}(P, Q) = \infty$ and the claim is vacuously true. Assuming this, we can take $p(x) = (1+r(x))q(x)$ where $r(x) = p(x)/q(x) - 1 \geq -1$. Now, using the following relations

$$\mathbb{E}_{X \sim Q}[r(X)] = \sum_{x \in \mathcal{X}} q(x)r(x) = 0 \quad (156)$$

$$\mathbb{E}_{X \sim Q}[|r(X)|] = \sum_{x \in \mathcal{X}} q(x)|r(x)| = \|P - Q\|_1 \quad (157)$$

$$D_{KL}(P, Q) = \mathbb{E}_{X \sim Q}[(1+r(X))\log(1+r(X)) - r(X)] \quad (158)$$

Combining equations 155 and 158 we get

$$D_{KL}(P, Q) \geq \frac{1}{2} \mathbb{E}_{X \sim Q} \left[\frac{r(X)^2}{1+r(X)/3} \right] \quad (159)$$

Now 157 implies $\mathbb{E}_Q[1+r(X)/3] = 1$, and hence

$$D_{KL}(P, Q) \geq \frac{1}{2} \mathbb{E}_Q \left[\frac{r(X)^2}{1+r(X)/3} \right] \mathbb{E}_Q[1+r(X)/3] \quad (160)$$

Now, using the Cauchy-Schwarz inequality:

$$(\mathbb{E}_Q[f(X)g(X)])^2 \leq \mathbb{E}_Q[f(X)^2] \mathbb{E}_Q[g(X)^2] \quad (161)$$

Taking $f(x) = \sqrt{r(x)^2/(1+r(x)/3)}$ and $g(x) = \sqrt{1+r(x)/3}$, we have

$$\begin{aligned}
D_{KL}(P, Q) &\geq \frac{1}{2} \mathbb{E}_Q [f(X)^2] \mathbb{E}_Q [g(X)^2] \\
&\geq \frac{1}{2} (\mathbb{E}_Q [f(X)g(X)])^2 \\
&= \frac{1}{2} \left(\mathbb{E}_Q \left[\frac{|r(X)|}{\sqrt{1+r(X)^2}} \cdot \sqrt{1+r(X)^2} \right] \right)^2 \\
&= \frac{1}{2} (\mathbb{E}_Q [|r(X)|])^2 \\
&= \frac{1}{2} \|P - Q\|_1^2
\end{aligned}$$

where the last equality follows from [157](#).

Proof of theorem 2:

The χ^2 divergence can be written as

$$D_{\chi^2}(P, Q) = \int_{\mathcal{X}} dQ \left(\frac{dP}{dQ} \right)^2 - 1,$$

and by the concavity of the logarithm, reminding that

$$\log x \leq x - 1, \quad \forall x > 0,$$

the RHS inequality can be directly proven,

$$D_{\chi^2}(P, Q) \leq \log(D_{\chi^2}(P, Q) + 1)$$

For the LHS inequality, using that $E[f(x)] \leq f(E[x])$ for f concave,

$$\int_{\mathcal{X}} dP \log \left(\frac{dP}{dQ} \right) \leq \log \left(\int_{\mathcal{X}} dQ \left(\frac{dP}{dQ} \right)^2 \right)$$

so that

$$D_{KL}(P, Q) \leq \log(D_{\chi^2}(P, Q) + 1)$$

and the theorem is proven.

C Appendix C

C.1 Statistics of DM discovery and upper limits

C.1.1 Poisson statistics

Dark matter searches consist in detectors counting events and measuring their recoiling energies. The probability to observe n events for an expected value of μ is given by the Probability Mass Function (PMF) of the Poisson distribution,

$$P(n|\mu) = \frac{\mu^n}{n!} e^{-\mu} \tag{162}$$

If a set of parameters predicts that a experiment should have observed more events than it actually did with a certain Confidence Level (CL), then this point is excluded at that CL.

$$\text{CL} = P(n > N|\mu) = \sum_{n=N+1}^{\infty} \frac{\mu^n}{n!} e^{-\mu} = 1 - \text{CDF}(N|\mu) \quad (163)$$

For a given dark matter mass, we find the cross section σ_{DM} corresponding to the value of μ_a determined by equation 163. The simplest way is to choose a reference cross section σ_{ref} , compute the number of events N_{ref} and find the upper bound at confidence level CL by

$$\sigma_{DM} < \frac{\mu_{CL}}{N_{ref}} \sigma_{ref} \quad (164)$$

So that we need to solve $\text{CDF}(N|\mu_{CL}) = (1 - CL)$ for μ_{CL} at a given CL and number of observed events N . With the exception of $N = 0$, the Poisson Cumulative Distribution Function (CDF) can not simply be inverted, but it can be expressed in terms of incomplete gamma functions, [164]

$$\text{CDF}(N|\mu) = e^{-\mu} \sum_{n=0}^N \frac{\mu^n}{n!} = \frac{\Gamma(N+1, \mu)}{N!} \equiv Q(N+1, \mu) \quad (165)$$

where the incomplete gamma function is given by,

$$\Gamma(s, x) \equiv \int_x^{\infty} dt t^{s-1} e^{-t} \quad (166)$$

and can be solved numerically for μ_{CL} by usual optimization packages in most programming languages. Poissonian statistics assumes no knowledge about the expected spectrum or the background of the experiment and interprets all observed events as a dark matter signal of equal significance. Therefore, the results are the most conservative ones, see Figure 40. The main caveat is that poissonian statistics assigns the same relevance to all recoil events, independently of their energy, while the expected spectrum of experiments is not constant but rather changing and suppressed at some specific energies due to the presence of the form factors $F(E_R)$, as we discussed in the section of inelastic dark matter 7.2.

C.1.2 Yellin Methods

If one knows the background of the experiment, methods based on likelihood, such as the Feldman-Cousins, [163], or Bayesian analysis, take into account the information encoded in the expected energy spectrum. S. Yellin proposed an alternative for experiments with no knowledge about the backgrounds *a priori*, since the likelihood associated with an unknown background is unknown, [133].

The **Maximum Gap method**, see Figure 39, excludes a cross section σ as being too high if most random experiments would give smaller maximum gaps, where the maximum gaps correspond to the largest differential recoil rate integration between any two events. The function C_0 equals the desired level of confidence,

$$C_0(x, \mu) = \sum_{k=0}^m \frac{(kx - \mu)^k e^{-kx}}{k!} \left(1 + \frac{k}{\mu - kx}\right) \quad (167)$$

where x is the size of the maximum gap of a random experiment and μ is the total expected number of events. C_0 is defined as the probability of the maximum gap size being smaller than a particular value of x .

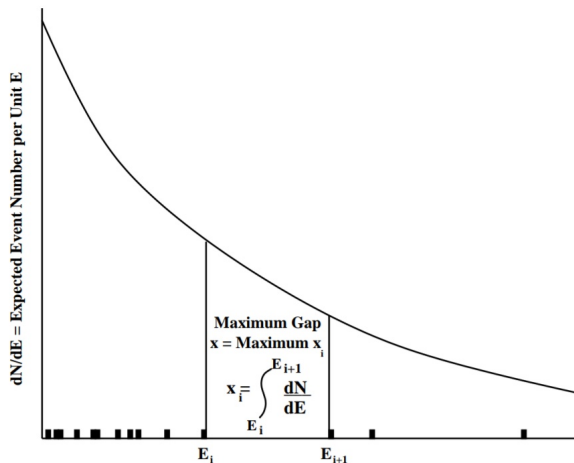


Figure 39: Illustration of the Maximum gap method

Yellin points out in his original paper, [133], that this method is particularly suited for situations of having a few events in the part of the energy range that seems relatively free of backgrounds, (small μ). Nevertheless, it can be used for an arbitrary number of events and we have noticed in our own implementation for the CRESST experiment that it yields a significant difference with respect to poissonian statistics, see Figure 40.

If there is a high density of events in the data, it would be useful to consider not only the spectral information given by maximum interval over which there is 1 event observed, but 2, 3...up to μ . By this means generalizes Yellin the Maximum Gap method to the **Optimum interval** method, where know the condifence level is given by the function $C_n(x, \mu)$, being the probability, for a given cross section without background, that all intervals with less than n events have their expected number of events less than x , and can be computed via Monte Carlo methods. This is the technique from which CRESST II and CRESST III official limits are published, and differ little from our implementation of the Maximum Gap method, see Figure 40.

C.2 DDCalc-2.2.0 software : Implementing CRESST III

The DDCalc software package, [134][135] is a set of routines and a frontend for doing various dark matter direct detection calculations for several experimental results, including Poisson likelihoods (binned and unbinned). Most of the calculations appearing in this Thesis have been performed within DDCalc or using DDCalc as the reference software for results

comparisons. For this purpose, it was necessary to implement the CRESST-III experiment in the software package for its proper use. This was done this with the help of Andreas Rappelt and Felix Kahlhoefer and appears as a new feature in the latest release of the software **DDCalc-2.2.0**. We strictly use the published CRESST-III data, and account for a finite energy resolution, energy threshold, and cut-survival probability in the expected WIMP spectrum according to the CRESST collaboration in [136]. The prediction of different models $p_{model}(E)$ is corrected to be comparable to the energy distribution measured by the detector in reconstructed energy $\bar{p}(E_{reco})$,

$$\bar{p}(E_{reco}) = \theta(E_{reco} - E_{thr,reco}) \cdot \bar{\epsilon} \cdot \epsilon_{x,Acc}(E_{reco}) \cdot \int_0^\infty p_{model}(E) \cdot \mathcal{N}(E_{reco} - E, \sigma_p^2) dE \quad (168)$$

where $\mathcal{N}(E_{reco} - E, \sigma_p^2)$ is a normal distribution with width σ_p being the resolution of the phonon detector for the convolution accounting for finite energy resolution. $\bar{\epsilon}$ is the cut-survival probability that accounts for the loss of the signal events from applied data selection criteria, and $\epsilon_{x,Acc}$ is needed if an acceptance region is defined. $\theta(E_{reco} - E_{thr,reco})$ imposes a lower cut off due to the energy threshold. Unlike CRESST-III experimental collaboration analysis, we did not perform an Analysis based on the Yellin's optimum interval method, but a binned likelihood analysis. The Poisson likelihood for the model is

$$\mathcal{L}_i(N_{p,i}|N_{o,i}) = \frac{(b_i + N_{p,i})^{N_{o,i}} e^{-(b_i + N_{p,i})}}{N_{o,i}!} \quad (169)$$

where $N_{p,i}$ is the number of predicted signal events in the analysis region, $N_{o,i}$ is the number of observed events, and b_i is the expected number of background events in that region. We assume no background model for the CRESST experiment, so that all events in the acceptance region are considered signal events. This yields a conservative limit and is consequent with the CRESST collaboration Yellin's Maximum gap/optimum interval method. In this case, b_i should be set to the value that maximizes the likelihood:

$$b_i = \begin{cases} N_{o,i} - N_{p,i}, & N_{o,i} > N_{p,i} \\ 0, & N_{o,i} \leq N_{p,i} \end{cases} \quad (170)$$

This leads to a one-sided likelihood, i.e. a non-zero WIMP signal can only be disfavoured but not preferred relative to the background-only hypothesis. Lastly, the likelihood function can be used to obtain an exclusion limit in the $\sigma - m_\chi$ plane. A point in the parameter space is excluded at 90% confidence level if

$$2\log\mathcal{L}(\sigma = 0) - 2\log\mathcal{L}(\sigma, m_\chi) > 1.64. \quad (171)$$

We notice that DDCalc spin independent CRESST III limits present a small disagreement agreement at masses $m_\chi \geq 5$ GeV w.r.t to the optimum interval method, see Figure 40. The disagreement at large masses is probably a result of stopping the analysis window at 1 keV along with the stronger constraining power of the optimum interval method for accounting small gaps. Still, this disagreement is not very relevant since above 3 GeV other direct detection experiments are currently much more constraining than CRESST III. Surprisingly, the likelihood background-free analysis of DDCalc yields slightly more aggressive results than CRESST III official ones obtained with the Optimum interval method. We notice that the CRESST collaboration numerous cases of contacts from people unable to reproduce their limits exactly, so we are just one among those, [136].

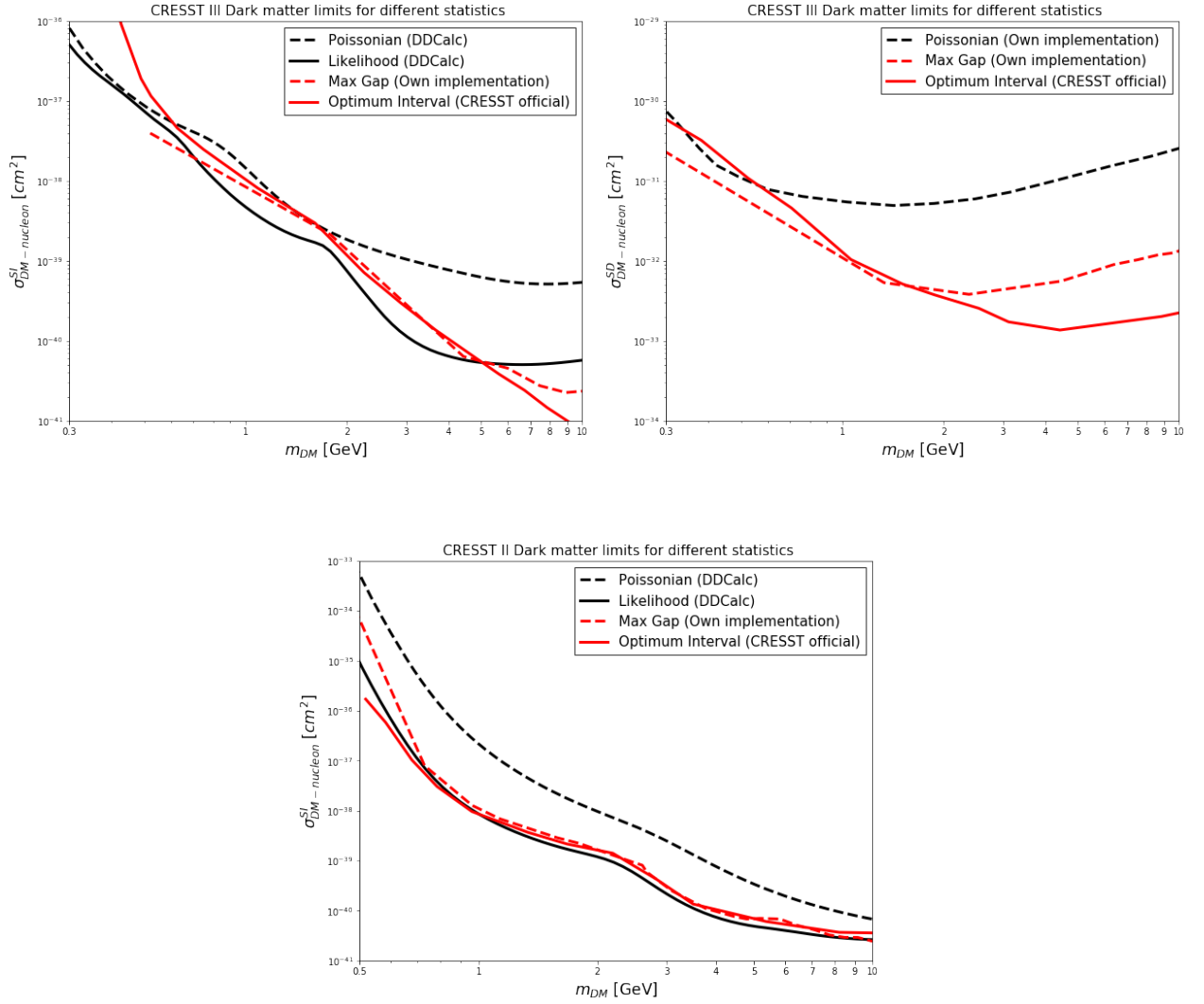


Figure 40: CRESST-III $\sigma - m_\chi$ exclusion limits for the spin independent (upper left) and spin dependent (upper right) cases. The dotted line represents the collaboration limit while the continuous one shows the DDCalc binned-likelihood analysis result. The results for spin independent at CRESST-II are shown in the lower panel.

References

- [1] G. Bertone and D. Hooper, *History of dark matter*, Rev. Mod. Phys. 90 (2018), no. 4 045002, <https://arxiv.org/abs/1605.04909>.
- [2] Kelvin, *Baltimore lectures on molecular dynamics and the wave theory of light*, (1904) <https://archive.org/details/baltimorelecture00kelviala>.
- [3] Jaan Einasto. *Dark Matter*, Brazilian Journal of Physics 43.5-6 (June 2013),pp. 369–374. ISSN: 0103-9733, 1678-4448. <https://link.springer.com/article/10.1007/s13538-013-0147-9>.
- [4] F.Zwicky, *Die Rotverschiebung von extragalaktischen Nebeln*, Helvetica Physica Acta 6, 110, (1933) pp. 110–127. ISSN: 0018-0238.
- [5] F.Zwicky, *Astrophys. J.* 86, 217, (1937).
- [6] M. Schwarzschild, *Mass distribution and mass-luminosity ratio in galaxies*, Astronomical Journal, Vol. 59, p. 273 (1954), <https://ui.adsabs.harvard.edu/abs/1954AJ.....59..273S/abstract>.
- [7] S. Van den Bergh, *Collapsed Objects in Clusters of Galaxies*, Nature, Volume 224, Issue 5222, pp. 891 (1969). <https://ui.adsabs.harvard.edu/abs/1969Natur.224..891V/abstract>.
- [8] Vera C. Rubin and W. Kent Ford Jr. *Rotation of the Andromeda Nebula from a Spectroscopic Survey of Emission Regions*, The Astrophysical Journal 159, p. 379 (1970), <https://ui.adsabs.harvard.edu/abs/1970ApJ...159..379R/abstract>.
- [9] D. Clowe et al., *A Direct Empirical Proof of the Existence of Dark Matter*, The Astrophysical Journal Letters 648.2 (2006), p. L109. ISSN: 1538-4357., <https://iopscience.iop.org/article/10.1086/508162>.
- [10] A.A Penzias, R. W. Wilson, *A Measurement Of Excess Antenna Temperature At 4080 Mc/s*. Astrophysical Journal Letters. 142: 419–421, (1965), <https://ui.adsabs.harvard.edu/abs/1965ApJ...142..419P/abstract>.
- [11] Planck Collaboration, *Planck 2018 results. VI. Cosmological parameters*, (2018), <https://arxiv.org/abs/1807.06209>.
- [12] Jungman, Gerard; Kamionkowski, Marc; Griest, Kim. *Supersymmetric dark matter*. Physics Reports. 267 (5–6): 195–373., (1996), <https://arxiv.org/abs/hep-ph/9506380>.
- [13] J.A. Peacock, *Large-scale surveys and cosmic structure*, Lectures delivered at the 2002 Tenerife Winter School, "Dark matter and dark energy in the universe", (2003), <https://arxiv.org/abs/astro-ph/0309240>.
- [14] Mariangela Lisanti, *Lectures on Dark Matter Physics*, <https://arxiv.org/abs/1603.03797>.

- [15] P. Salati, *Indirect and direct dark matter detection*, Cargese Summer School on Cosmology and Particle Physics Beyond the Standard Models, (2007), <https://inspirehep.net/literature/776274>.
- [16] E. T. Jaynes., *Information Theory and Statistical Mechanics*, Physical Review. Series II 106, 620, (1957), <https://journals.aps.org/pr/abstract/10.1103/PhysRev.106.620>.
- [17] The CRESST collaboration, *Direct Dark Matter Search with the CRESST II Experiment*, Contribution to ICHEP 2016, 217 (2016), <https://arxiv.org/abs/1611.02113>.
- [18] The CRESST collaboration, *Searches for Light Dark Matter with the CRESST-III Experiment*, Journal of Low Temperature Physics volume 199, pages 547–555, (2020), <https://link.springer.com/article/10.1007/s10909-020-02343-3>.
- [19] C. Shannon, *A Mathematical Theory of Communication*, The Bell System Technical Journal 27 (3): 379–423 (1948), <http://people.math.harvard.edu/~ctm/home/text/others/shannon/entropy/entropy.pdf>.
- [20] The CRESST collaboration, *Description of CRESST-III Data*, (2019), <https://arxiv.org/abs/1905.07335>.
- [21] The Super-Kamiokande collaboration, *Search for neutrinos from annihilation of captured low-mass dark matter particles in the Sun by Super-Kamiokande*, Phys.Rev.Lett. 114 (2015) 14, 14130, <https://arxiv.org/abs/1503.04858>.
- [22] J. Skilling, *The Axioms of Maximum Entropy*, pp. 173–187. Springer Netherlands, Dordrecht, (1988), https://link.springer.com/chapter/10.1007/978-94-009-3049-0_8.
- [23] A. N. Baushev, *Extragalactic dark matter and direct detection experiments*, Astrophys.J. 771 (2013) 117, <https://arxiv.org/abs/1208.0392>.
- [24] D. Tucker-Smith, N. Weiner, *Inelastic dark matter*, Phys.Rev.D 64 (2001) 043502, <https://arxiv.org/abs/hep-ph/0101138>.
- [25] Katherine Freese, *Review of Observational Evidence for Dark Matter in the Universe and in upcoming searches for Dark Stars*, EAS Publ.Ser. 36 (2009) 113-126, <https://arxiv.org/abs/0812.4005>.
- [26] P. Mroz, A. Udalski, D.M. Skowron, J. Skowron, I. Soszynski, P. Pietrukowicz, M.K. Szymanski, R. Poleski, S. Kozlowski, K. Ulaczyk, *Rotation curve of the Milky Way from Classical Cepheids*, ApJL 870, L10 (2019), <https://arxiv.org/abs/1810.02131>.
- [27] NASA, ESA, STScI, and CXC ; D. Harvey, R. Massey, T. Kitching, and A. Taylor and E. Tittley, NASA HUBBLESITE Resource Gallery. <https://hubblesite.org/contents/media/images/2015/10/3508-Image.html?news=true>.
- [28] M. Milgrom, *A modification of the Newtonian dynamics-Implications for galaxies*, The Astrophysical Journal 270 (1983), p. 371, <https://ui.adsabs.harvard.edu/abs/1983ApJ...270..371M/abstract>.

- [29] SDSS collaboration, *Detection of the Baryon Acoustic Peak in the Large-Scale Correlation Function of SDSS Luminous Red Galaxies*, *Astrophys.J.* 633 (2005) 560-574, <https://arxiv.org/abs/astro-ph/0501171>.
- [30] D. Baumann, *TASI Lectures on Inflation*, (2009), <https://arxiv.org/abs/0907.5424>.
- [31] R. K. Sachs and A. M. Wolfe, *Perturbations of a Cosmological Model and Angular Variations of the Microwave Background*, *The Astrophysical Journal* 147 (1967), <https://ui.adsabs.harvard.edu/abs/1967ApJ...147...73S/abstract>.
- [32] G. Steigman, *Primordial Nucleosynthesis in the Precision Cosmology Era*, *The Annual Review of Nuclear and Particle Science* 57 (2007), 463-491, <https://arxiv.org/abs/0712.1100>.
- [33] K. A. Olive and Particle Data Group. *Review of Particle Physics*, *Chinese Physics C* 38.9 (2014), p. 090001. <https://iopscience.iop.org/article/10.1088/1674-1137/38/9/090001>.
- [34] A. D. Popolo, M. Le Delliou, *Small scale problems of the CDM model: a short review*, *Galaxies* 5 (2017) 1, 17, <https://arxiv.org/abs/1606.07790>.
- [35] S. Weinberg, *Cosmology*, Oxford University Press, (2008)
- [36] P. J. E. Peebles, *Principles of Physical Cosmology*, Princeton University Press, (1993).
- [37] J.A. Peacock, *Cosmological Physics*, Cambridge U. Press, (1999).
- [38] P. Mészáros, *The behaviour of point masses in an expanding cosmological substratum*, *Astron. Astrophys.* 225-228, (1974), <https://inspirehep.net/literature/93541>.
- [39] P. Peter and J. P. Uzan, *Primordial Cosmology*, Oxford University Press, (2005).
- [40] E. Bertschinger, J. M. Gelb, *Cosmological N-Body Simulations*, *Computers in Physics* 5, 164 (1991), <https://aip.scitation.org/doi/pdf/10.1063/1.4822978>.
- [41] N. Yoshida, *Structure Formation in the Early Universe*, (2009), <https://arxiv.org/abs/0906.4372v1>.
- [42] J. R. Primack, A. K. Gross, *Hot Dark Matter in Cosmology*, <https://cds.cern.ch/record/447060/files/0007165.pdf>.
- [43] T. Lacroix, A. Núñez-Castiñeyra, M. Stref, J. Lavalle, E. Nezri, *Predicting the dark matter velocity distribution in galactic structures: tests against hydrodynamic cosmological simulations*, LUPM:20-024, IFT-UAM/CSIC-20-64, (2020), <https://arxiv.org/abs/2005.03955>.
- [44] L. Lindegren, U. Lammers, U. Bastian, J. Hernández, S. Klioner, D. Hobbs, A. Bombrun, D. Michalik, M. Ramos-Lerate, A. Butkevich, G. Comoretto, E. Joliet, B. Holl, A. Hutton, P. Parsons, H. Steidelmüller, U. Abbas, M. Altmann, A. Andrei, S. Anton, N. Bach, C. Barache, U. Becciani, J. Berthier, L. Bianchi, M. Biermann, S. Bouquillon, G. Bourda, T. Brüsemeister, B. Bucciarelli, D. Busonero, T. Carlucci, J. Castañeda, P.

- Charlot, M. Clotet, M. Crosta, M. Davidson, F. de Felice, R. Drimmel, C. Fabricius, A. Fienga, F. Figueras, E. Fraile, M. Gai, N. Garralda, R. Geyer, J.J. González-Vidal, R. Guerra, N.C. Hambly, M. Hauser, S. Jordan, M.G. Lattanzi, H. Lenhardt, S. Liao, W. Löffler, P.J. McMillan, F. Mignard, A. Mora, R. Morbidelli, J. Portell, A. Riva, M. Sarasso, I. Serraller, H. Siddiqui, R. Smart, A. Spagna, U. Stampa, I. Steele, F. Taris, J. Torra, W. van Reeve, A. Vecchiato, S. Zschocke, J. de Bruijne, G. Gracia, F. Raison, T. Lister, J. Marchant, R. Messineo, M. Soffel, J. Osorio, A. de Torres, W. O'Mullane, *Gaia Data Release 1: Astrometry - one billion positions, two million proper motions and parallaxes*, AA 595, A4 (2016), <https://arxiv.org/abs/1609.04303>.
- [45] A. Ibarra, B. J. Kavanagh, A. Rappelt, *Impact of substructure on local dark matter searches*, JCAP 12 (2019) 013, <https://arxiv.org/abs/1908.00747>.
- [46] V. Belokurov et. al., *The Field of Streams: Sagittarius and its Siblings*, Astrophys. J. 642 (2006) L137, <https://arxiv.org/abs/astro-ph/0605025>.
- [47] G.C. Myeong, N.W. Evans, V. Belokurov, S. Koposov, J.L. Sanders, *A Halo Substructure in Gaia Data Release 1*, Monthly Notices of the Royal Astronomical Society: Letters, Volume 469, Issue 1, (2017), Pages L78-L82, <https://arxiv.org/abs/1704.01363>.
- [48] C. W. Purcell, J. S. Bullock, M. Kaplinghat, *The Dark Disk of the Milky Way*, Astrophys.J.703:2275-2284, (2009), <https://arxiv.org/abs/0906.5348>.
- [49] K. Schutz, T. Lin, B. R. Safdi, C. L. Wu, *Constraining a Thin Dark Matter Disk with Gaia*, Phys. Rev. Lett. 121, 081101 (2018), <https://arxiv.org/abs/1711.03103>.
- [50] J. F. Navarro, C. S. Frenk, and S. D. M. White, *A Universal density profile from hierarchical clustering*, Astrophys. J. 490 (1997) 493–508, <https://arxiv.org/abs/astro-ph/9611107>.
- [51] A. W. Graham, D. Merritt, B. Moore, J. Diemand, and B. Terzic, *Empirical models for Dark Matter Halos. I. Nonparametric Construction of Density Profiles and Comparison with Parametric Models*, Astron. J. 132 (2006) 2685–2700, <https://arxiv.org/abs/astro-ph/0509417>.
- [52] A. Burkert, *The structure of dark matter halos in dwarf galaxies*, Astrophys. J.447,L25(1995), <https://iopscience.iop.org/article/10.1086/309560/meta>.
- [53] W. J. G. de Blok, *The Core-Cusp Problem*, Advances in Astronomy 2010 (Jan, 2010) 789293, <https://arxiv.org/abs/0910.3538>.
- [54] S. Sivertsson, H. Silverwood, J. I. Read, G. Bertone, and P. Steger, *The local dark matter density from SDSS-SEGUE G-dwarfs*, Mon. Not. Roy. Astron. Soc. 478 (2018), no. 2 1677–1693, <https://arxiv.org/abs/1708.07836>.
- [55] A. Rappelt, *Astrophysical uncertainties of direct dark matter searches*, PhD, Munich, Tech. U. (2020), <https://inspirehep.net/literature/1784298>.

- [56] M. Pato, F. Iocco, and G. Bertone, *Dynamical constraints on the dark matter distribution in the Milky Way*, JCAP 1512 (2015), no. 12 001, <https://arxiv.org/abs/1504.06324>.
- [57] J. I. Read, *The Local Dark Matter Density*, J.Phys.G 41 (2014) 063101, <https://arxiv.org/abs/1404.1938>.
- [58] N. W. Evans, C. A.J. O’Hare, C. McCabe, *SHM++: A Refinement of the Standard Halo Model for Dark Matter Searches in Light of the Gaia Sausage*, Phys.Rev.D 99 (2019) 2, 023012, <https://arxiv.org/abs/1810.11468>.
- [59] J. D. Vergados, Y. Semertzidis, *Axionic dark matter signatures in various halo models*, Nucl.Phys.B 915 (2017) 10-18, <https://arxiv.org/abs/1601.04765>.
- [60] P. Salati, *Indirect and direct dark matter detection*, PoS CARGESE2007 (2007), 009, <https://inspirehep.net/literature/776274>.
- [61] Z. Liu, Y. Su, Y. L. S. Tsai, B. Yu, Q. Yuan, *A combined analysis of PandaX, LUX, and XENON1T experiments within the framework of dark matter effective theory*, NCTS-PH/1717, (2017), <https://arxiv.org/abs/1708.04630>.
- [62] D. Bhattacharya, *IUCAA PH217: Fundamentals of Astrophysics*, <http://www.iucaa.in/~dipankar/ph217/>.
- [63] A. A. Vlasov, *On Vibration Properties of Electron Gas*. J. Exp. Theor. Phys. 8 (3): 291, (1938), <https://ufn.ru/ru/articles/1967/11/f/>.
- [64] A. S. Eddington, *The distribution of stars in globular clusters*, MNRAS 76 (1916) 572–585, <https://academic.oup.com/mnras/article/76/7/572/1122812>.
- [65] I. R. King, *The structure of star clusters. iii. some simple dynamical models*, Astron. J. 71, (1966) 64, <https://ui.adsabs.harvard.edu/abs/1966AJ.....71...64K/abstract>.
- [66] L. M. Widrow and J. Dubinski, *Equilibrium Disk-Bulge-Halo Models for the Milky Way and Andromeda Galaxies*, Astrophys. J. 631 (2005) 838–855, <https://arxiv.org/abs/astro-ph/0506177>.
- [67] A. M. Green, *Astrophysical uncertainties on direct detection experiments*, Mod. Phys. Lett. A27 (2012) 1230004, <https://arxiv.org/abs/1112.0524>.
- [68] T. Piffl et. al., *The RAVE survey: the Galactic escape speed and the mass of the Milky Way*, Astron. Astrophys. 562 (2014) A91, <https://arxiv.org/abs/1309.4293>.
- [69] M. Vogelsberger, A. Helmi, V. Springel, S. D. M. White, J. Wang, C. S. Frenk, A. Jenkins, A. D. Ludlow, and J. F. Navarro, *Phase-space structure in the local dark matter distribution and its signature in direct detection experiments*, Mon. Not. Roy. Astron. Soc. 395 (2009) 797–811, <https://arxiv.org/abs/0812.0362>.
- [70] L. Necib, M. Lisanti, V. Belokurov, *Inferred Evidence For Dark Matter Kinematic Substructure with SDSS-Gaia*, (2018), <https://arxiv.org/abs/1807.02519>.

- [71] M. Vogelsberger et al., *Phase-space structure in the local dark matter distribution and its signature in direct detection experiments*, Mon.Not.Roy.Astron.Soc. 395 (2009) 797-811, <https://arxiv.org/abs/0812.0362>.
- [72] F. Calore, N. Bozorgnia, M. Lovell, G. Bertone, M. Schaller, C. S. Frenk, R. A. Crain, J. Schaye, T. Theuns, J. W. Trayford, *Simulated Milky Way analogues: implications for dark matter indirect searches*, JCAP 12 (2015) 053, <https://arxiv.org/abs/1509.02164>.
- [73] E.T. Jaynes, *Information Theory and Statistical Mechanics*, Phys. Rev. 106, 620, (1957), <https://journals.aps.org/pr/abstract/10.1103/PhysRev.106.620>.
- [74] F. Mayet, A. M. Green, J. B. R. Battat, J. Billard, N. Bozorgnia, G. B. Gelmini, P. Gondolo, B. J. Kavanagh, S. K. Lee, D. Loomba, J. Monroe, B. Morgan, C. A. J. O'Hare, A. H. G. Peter, N. S. Phan, S. E. Vahsen, *A review of the discovery reach of directional Dark Matter detection*, Phys.Rept. 627 (2016) 1-49, <https://arxiv.org/abs/1602.03781>.
- [75] G. Busoni, A. De Simone, E. Morgante, A. Riotto, *On the validity of the effective field theory for dark matter searches at the LHC, part II: complete analysis for the s-channel*, Phys.Lett.B 728 (2014) 412-421, <https://arxiv.org/abs/1307.2253>.
- [76] J. Abdallah et al, *Simplified Models for Dark Matter Searches at the LHC*, Phys.Dark Univ. 9-10 (2015) 8-23, <https://arxiv.org/abs/1506.03116>.
- [77] S. P. Liew, M. Papucci, A. Vichi, K. M. Zurek, *Mono-X Versus Direct Searches: Simplified Models for Dark Matter at the LHC*, JHEP 06 (2017) 082, <https://arxiv.org/abs/1612.00219>.
- [78] ATLAS Collaboration, *Search for new high-mass phenomena in the dilepton final state using 36 fb¹ of proton-proton collision data at $\sqrt{s} = 13$ TeV with the ATLAS detector*, CERN-EP-2017-119, <https://arxiv.org/abs/1707.02424>.
- [79] S. A. Malik et al., *Interplay and Characterization of Dark Matter Searches at Colliders and in Direct Detection Experiments*, CERN-PH-TH/2014-180, <https://arxiv.org/abs/1409.4075>.
- [80] The ATLAS Collaboration, *Dark matter summary plots*, ATL-PHYS-PUB-2019-030, <https://cds.cern.ch/record/2684864/files/ATL-PHYS-PUB-2019-030.pdf>.
- [81] L. Rinchuso, E. Moulin (for the H.E.S.S. Collaboration), *Dark matter searches toward the Galactic Centre halo with H.E.S.S.*, Moriond VHEPU (2017), 255-262, <https://arxiv.org/abs/1711.08634>.
- [82] I. Cholis, D. P. Finkbeiner, L. Goodenough, N. Weiner, *The PAMELA Positron Excess from Annihilations into a Light Boson*, JCAP 0912:007,2009, <https://arxiv.org/abs/0810.5344>.
- [83] J. Herms, A. Ibarra, A. Vittino, S. Wild, *Antideuterons in cosmic rays: sources and discovery potential*, TUM-HEP 1063/16, <https://arxiv.org/abs/1610.00699>.

- [84] IceCube Collaboration, *Search for annihilating dark matter in the Sun with 3 years of IceCube data*, Eur. Phys. J. C (2017) 77: 146, <https://arxiv.org/abs/1612.05949>.
- [85] L. M. Krauss, K. Freese, D. N. Spergel, and W. H. Press, *Cold dark matter candidates and the solar neutrino problem*, The Astrophysical Journal, 299:1001-1006, (1985), <https://inspirehep.net/literature/223576>.
- [86] A. Gould, *Resonant Enhancements In WIMP Capture By The Earth*, SLAC - PUB - 4226, (1987), <https://inspirehep.net/literature/245322>.
- [87] K. Griest, D. Seckel, K. Griest(UC, Santa Cruz), D. Seckel, Nucl.Phys.B 283 (1987) 681-705, <https://inspirehep.net/literature/231215>.
- [88] A. Serenelli, S. Basu, J. W. Ferguson, M. Asplund, *New Solar Composition: The Problem With Solar Models Revisited*, Astrophys.J.705:L123-L127, (2009), <https://arxiv.org/abs/0909.2668>.
- [89] A. Gould, *WIMP Distribution in and Evaporation From the Sun*, Astrophys.J. 321 (1987) 560, <https://inspirehep.net/literature/244662>.
- [90] A. Gould, *Evaporation of WIMPs with Arbitrary Cross Sections*, Astrophysical Journal v.356, p.302, <https://ui.adsabs.harvard.edu/abs/1990ApJ...356..302G/abstract>.
- [91] M. W. Goodman, E. Witten, *Detectability of Certain Dark Matter Candidates*, Phys.Rev.D 31 (1985) 3059, <https://inspirehep.net/literature/207030>.
- [92] T. M. Undagoitia, L. Rauch, *Dark matter direct-detection experiments*, J. Phys. G43 (2016) no.1, 013001, <https://arxiv.org/abs/1509.08767>.
- [93] R. F. Lang, *Search for Dark Matter with the CRESST Experiment*, (2008), <https://www.semanticscholar.org/paper/Search-for-Dark-Matter-with-the-CRESST-Experiment-Lang/8fbc2d0455a63a35c0a4740b237c1968bfa6ed5d>.
- [94] E. Polisensky and M. Ricotti, *Constraints on the dark matter particle mass from the number of Milky Way satellites*, Phys. Rev. D 83, 043506, (2011), <https://journals.aps.org/prd/abstract/10.1103/PhysRevD.83.043506>.
- [95] A. Boyarsky, O. Ruchayskiy, D. Iakubovskiy, *A lower bound on the mass of Dark Matter particles*, JCAP 0903:005, (2009), <https://arxiv.org/abs/0808.3902>
- [96] E. O. Nadler, V. Gluscevic, K. K. Boddy, R. H. Wechsler, *Constraints on Dark Matter Microphysics from the Milky Way Satellite Population*, ApJL 878, 32 (2019), <https://arxiv.org/abs/1904.10000>.
- [97] W. L. Xu, C. Dvorkin, A. Chael, *Probing sub-GeV Dark Matter-Baryon Scattering with Cosmological Observables*, Phys. Rev. D 97, 103530 (2018), <https://arxiv.org/abs/1802.06788>.

- [98] B. W. Lee and S. Weinberg, *Cosmological Lower Bound on Heavy-Neutrino Masses*, Phys. Rev. Lett. 39, 165, (1977), <https://journals.aps.org/prl/abstract/10.1103/PhysRevLett.39.165>.
- [99] Edward W. Kolb and Keith A. Olive, *Lee-Weinberg bound reexamined*, Phys. Rev. D 33, 1202, (1986), <https://journals.aps.org/prd/abstract/10.1103/PhysRevD.33.1202>.
- [100] C. Boehm, P. Fayet, *Scalar Dark Matter candidates*, Nucl.Phys.B683:219-263, (2004), <https://arxiv.org/abs/hep-ph/0305261>.
- [101] H. Okada, Y. Orikasa, T. Toma, *Nonthermal dark matter models and signals*, Phys. Rev. D 93, 055007 (2016), <https://arxiv.org/abs/1511.01018>.
- [102] R. Garani, P. Tinyakov, *Constraints on Dark Matter from the Moon*, Phys.Lett. B804 (2020) 135403, <https://arxiv.org/abs/1912.00443>.
- [103] Kate Scholberg, *Coherent elastic neutrino-nucleus scattering*, (2015), <https://iopscience.iop.org/article/10.1088/1742-6596/606/1/012010>.
- [104] The CoGeNT collaboration, *CoGeNT: A Search for Low-Mass Dark Matter using p-type Point Contact Germanium Detectors*, Physical Review D 88, 012002 (2013), <https://arxiv.org/abs/1208.5737>.
- [105] DAMA/LIBRA collaboration, *First model independent results from DAMA/LIBRA-phase2*, Nucl. Phys. At. Energy 19 (2018) 307-325, <https://arxiv.org/abs/1805.10486>.
- [106] The SuperCDMS collaboration, *Results from the Super Cryogenic Dark Matter Search (SuperCDMS) experiment at Soudan*, Phys. Rev. Lett. 120, 061802 (2018), <https://arxiv.org/abs/1708.08869>.
- [107] The XENON collaboration, *Dark Matter Search Results from a One TonneYear Exposure of XENON1T*, Phys. Rev. Lett. 121, 111302 (2018), <https://arxiv.org/abs/1805.12562>.
- [108] PandaX-II Collaboration, *Dark Matter Results From 54-Ton-Day Exposure of PandaX-II Experiment*, Phys.Rev.Lett. 119 (2017) 18, 181302, <https://inspirehep.net/literature/1618319>.
- [109] The PICO collaboration, *Dark Matter Search Results from the Complete Exposure of the PICO-60 C3F8 Bubble Chamber*, Phys. Rev. D 100, 022001 (2019), <https://arxiv.org/abs/1902.04031>.
- [110] M. Schumann, *Direct Detection of WIMP Dark Matter: Concepts and Status*, J. Phys. G46 (2019) no.10, 103003, <https://arxiv.org/abs/1903.03026>.
- [111] The CRESST Collaboration, *Impact of Coherent Neutrino Nucleus Scattering on Direct Dark Matter Searches based on CaWO₄ Crystals*, Astropart.Phys. 69 (2015) 44-49, <https://arxiv.org/abs/1408.2357>.

- [112] C. McCabe, *The Earth's velocity for direct detection experiments*, IPPP/13/95, DCPT/13/190, <https://arxiv.org/abs/1312.1355>.
- [113] D. G. Cerdeno, A. M. Green, *Direct detection of WIMPs*, Chapter 17 of "Particle Dark Matter: Observations, Models and Searches" ed. G. Bertone, (2010), Cambridge University Press, <https://arxiv.org/abs/1002.1912v1>
- [114] F. Froberg, A. R. Duffy, *Annual Modulation in Direct Dark Matter Searches*, (2020), <https://arxiv.org/abs/2003.04545>.
- [115] J. Engel, *Nuclear form-factors for the scattering of weakly interacting massive particles*, Phys.Lett.B 264 (1991) 114-119, <https://inspirehep.net/literature/323343>.
- [116] European Muon, J. Ashman et. al., *A Measurement of the Spin Asymmetry and Determination of the Structure Function $g(1)$ in Deep Inelastic Muon-Proton Scattering*, Phys. Lett. B206 (1988) 364., <https://inspirehep.net/literature/252744>.
- [117] F. Iachello, L. M. Krauss, and G. Maino, *Spin Dependent Scattering of Weakly Interacting Massive Particles in Heavy Nuclei*, Phys. Lett. B254 (1991) 220-224., <https://inspirehep.net/literature/295857>.
- [118] The CRESST collaboration, *First results on sub-GeV spin-dependent dark matter interactions with ${}^7\text{Li}$* , Eur. Phys. J. C, 79 7 (2019) 630, <https://arxiv.org/abs/1902.07587>.
- [119] S. Diamond, S. Boyd, *CVXPY: A Python-Embedded Modeling Language for Convex Optimization*, Journal of Machine Learning Research 17 (2016) 1-5, https://web.stanford.edu/~boyd/papers/pdf/cvxpy_paper.pdf.
- [120] A. Ibarra, A. Rappelt, *Optimized velocity distributions for direct dark matter detection*, TUM-HEP 1079/17, (2017), <https://arxiv.org/abs/1703.09168>.
- [121] A. Ibarra, B. J. Kavanagh, A. Rappelt, *Bracketing the impact of astrophysical uncertainties on local dark matter searches*, JCAP 12 (2018) 018, <https://arxiv.org/abs/1806.08714>.
- [122] A. Shun-ichi; N. Hiroshi, *Methods of information geometry*, Oxford University Press. ISBN 0-8218-0531-2., (2000).
- [123] H. Padé, *Sur la représentation approchée d'une fonction par des fractions rationnelles*, Annales Scientifiques de l'École Normale Supérieure. Volume 9 supplement, (1892), S. 1-93.
- [124] A. Fowlie, *Halo-independence with quantified maximum entropy at DAMA/LIBRA*, JCAP 1710 (2017) no.10, 002, <https://arxiv.org/abs/1708.00181>.
- [125] B. Feldstein and F. Kahlhoefer, *Quantifying (dis)agreement between direct detection experiments in a halo-independent way*, JCAP 1412 (2014), no. 12 052, <https://www.arxiv.org/abs/1409.5446>.

- [126] N. Bozorgnia and T. Schwetz, What is the probability that direct detection experiments have observed Dark Matter?, JCAP 1412 (2014), no. 12 015, <https://arxiv.org/abs/1410.6160>.
- [127] J. A. Fernandez, *Topologia*, Universidad Nacional de Educacion a Distancia, (1998)
- [128] F.Liese, I. Vajda, *On divergences and informations in statistics and information theory* IEEE Transactions on Information Theory, (2006), <https://ieeexplore.ieee.org/document/1705001>.
- [129] S. Kullback, *Information Theory and Statistics*, John Wiley Sons., (1959), ISBN 0-8446-5625-9.
- [130] A. Domahidi, E. Chu, S. Boyd, *ECOS: An SOCP Solver for Embedded Systems*, European Control Conference (ECC) July 17-19, (2013), https://web.stanford.edu/~boyd/papers/pdf/ecos_ecc.pdf.
- [131] S. Boyd and L. Vandenberghe, *Convex Optimization*, Cambridge University Press, <https://web.stanford.edu/~boyd/cvxbook/>.
- [132] V. Chandrasekaran, P. Shah *Relative entropy optimization and its applications*, Mathematical Programming volume 161, pages1–32(2017), <https://link.springer.com/article/10.1007/s10107-016-0998-2>
- [133] S. Yellin, *Finding an Upper Limit in the Presence of Unknown Background*, Phys.Rev. D66 (2002) 032005, <https://arxiv.org/abs/physics/0203002>.
- [134] T Bringmann, J Conrad, JM Cornell, LA Dal, J Edsjö, B Farmer, F Kahlhoefer, A Kvellestad, A Putze, C Savage, P Scott, C Weniger, M White S Wild 2017, EPJC 77 (2017) 831, *DarkBit: A GAMBIT module for computing dark matter observables and likelihoods*, <https://arxiv.org/abs/1705.07920>.
- [135] P Athron , C Balazs, A Beniwal, S Bloor, JE Camargo-Molina, JM Cornell, B Farmer, A Fowlie, TE Gonzalo, F Kahlhoefer, A Kvellestad, GD Martinez, P Scott, AC Vincent, S Wild, M White AG Williams 2018, *Global analyses of Higgs portal singlet dark matter models using GAMBIT*, EPJC 79 (2019) 38, <https://arxiv.org/abs/1808.10465>.
- [136] CRESST Collaboration, *Description of CRESST-III Data*, (2019) <https://arxiv.org/abs/1905.07335>.
- [137] G. Arcadi, Y. Mambrini, F. Richard, *Z-portal dark matter*, JCAP 03 (2015) 018, <https://arxiv.org/abs/1411.2985>.
- [138] M. Escudero, A. Berlin, D. Hooper, M.X. Lin, *Toward (Finally!) Ruling Out Z and Higgs Mediated Dark Matter Models*, JCAP 12 (2016) 029, <https://arxiv.org/abs/1609.09079>.
- [139] O. Lebedev, Y. Mambrini, *Axial Dark Matter: the case for an invisible Z'*, Phys.Lett.B 734 (2014) 350-353, <https://arxiv.org/abs/1403.4837>.

- [140] T. Falk, K. A. Olive, M. Srednicki, *Heavy Sneutrinos as Dark Matter*, Phys.Lett.B339:248-251,(1994), <https://arxiv.org/abs/hep-ph/9409270>.
- [141] C. Arina, N. Fornengo, *Sneutrino cold dark matter, a new analysis: relic abundance and detection rates*, JHEP 11 (2007) 029, <https://arxiv.org/abs/0709.4477v1>.
- [142] C. Arina, *Sneutrino cold dark matter in extended MSSM models*, 43rd Rencontres de Moriond on Electroweak Interactions and Unified Theories, 575-578 <https://arxiv.org/abs/0805.1991>.
- [143] J. Bramante, P. J. Fox, G. D. Kribs, A. Martin, *The Inelastic Frontier: Discovering Dark Matter at High Recoil Energy*, Phys. Rev. D 94, 115026 (2016), <https://arxiv.org/abs/1608.02662>.
- [144] M. Drewes, J. Hajer, *Heavy neutrinos in displaced vertex searches at the LHC and HL-LHC*, J. High Energ. Phys. (2020) 2020: 70, <https://arxiv.org/abs/1903.06100>.
- [145] M. Fabbrichesi, E. Gabrielli, G. Lanfranchi, *The Dark Photon*, (2020), <https://arxiv.org/abs/2005.01515>.
- [146] M. Bertolini, *Lectures on Supersymmetry*, SISS, (2019), <https://people.sissa.it/~bertmat/susycourse.pdf>.
- [147] IceCube Collaboration, PICO collaboration, *Velocity independent constraints on spin-dependent DM-nucleon interactions from IceCube and PICO*, (2019) <https://arxiv.org/abs/1907.12509>.
- [148] A. Fowlie, *Non-parametric uncertainties in the dark matter velocity distribution*, JCAP 01 (2019) 006, <https://inspirehep.net/literature/1693208>
- [149] J. Skilling, *The Axioms of Maximum Entropy*, pp. 173–187. Springer Netherlands, Dordrecht, (1988).
- [150] A. A. Markov, *Theory of Algorithms*, (1954), Imprint Moscow, Academy of Sciences of the USSR.
- [151] M. Lisanti, S. Mishra-Sharma, N. L. Rodd, B. R. Safdi, R. H. Wechsler, *Mapping Extragalactic Dark Matter Annihilation with Galaxy Surveys: A Systematic Study of Stacked Group Searches*
- [152] S. Mishra-Sharma, *Extragalactic Searches for Dark Matter Annihilation*, Ph.D. thesis, Princeton, (2018), <https://arxiv.org/abs/1809.04665> .
- [153] D. Makarov I. Karachentsev, *Galaxy groups and clouds in the local ($z < 0.01$) Universe*, Monthly Notices of the Royal Astronomical Society, Volume 412, Issue 4, Pages 2498–2520, (2011), <https://academic.oup.com/mnras/article/412/4/2498/1020594>.
- [154] J. Binney; S. Tremaine, *Galactic Dynamics: Second Edition*, Princeton University Press, Princeton, NJ USA, (2008).

- [155] S. Chang, G. D. Kribs, D. Tucker-Smith, N. Weiner, *Inelastic Dark Matter in Light of DAMA/LIBRA*, Phys.Rev.D79:043513, (2009), <https://arxiv.org/abs/0807.2250>.
- [156] J. March-Russell, C. McCabe and M. McCullough, *Inelastic dark matter, non-standard halos and the DAMA/LIBRA results*, Journal of High Energy Physics, Volume 2009, JHEP05(2009), <https://arxiv.org/abs/0812.1931>.
- [157] Y. Cui, D. E. Morrissey, D. Poland, L. Randall, *Candidates for Inelastic Dark Matter*, JHEP 05 (2009) 076, <https://arxiv.org/abs/0901.0557>.
- [158] F. Kahlhoefer, F. Reindl, K. Schäffner, K. Schmidt-Hoberg, S. Wild, *Model-independent comparison of annual modulation and total rate with direct detection experiments*, JCAP 1805 (2018) no.05, 074, <https://arxiv.org/abs/1802.10175>.
- [159] E. Ramos Méndez, Programación lineal y entera, Ediciones Académicas S.A., UNED.
- [160] M. Grant, *Disciplined Convex Programming*, (2004) PhD thesis, Stanford.
- [161] MOSEK ApS, *The MOSEK optimization toolbox for MATLAB manual*. Version 9.0., (2019), <http://docs.mosek.com/9.0/toolbox/index.html>
- [162] Pollard's Pinsker inequality proof: <http://www.stat.yale.edu/~pollard/Books/Asymptopia/Metrics.pdf>, <https://www.cs.bgu.ac.il/~asml162/wiki.files/pollard-pinsker.pdf>.
- [163] Gary J. Feldman, Robert D. Cousins, *A Unified Approach to the Classical Statistical Analysis of Small Signals*
- [164] Abramowitz, Milton; Stegun, I. Ann, *Handbook of Mathematical Functions with Formulas, Graphs, and Mathematical Tables*, (1983), ISBN 978-0-486-61272-0.